HOT DIRAC FERMION DYNAMICS AND COHERENTLY CONTROLLED PHOTOCURRENT GENERATION IN EPITAXIAL GRAPHENE

by

Dong Sun

A dissertation submitted in partial fulfillment
of the requirements for the degree of
Doctor of Philosophy
(Physics)
in The University of Michigan
2009

Doctoral Committee:

Professor Theodore B. Norris, Co-chair
Professor Roberto D. Merlin, Co-chair
Professor Duncan G. Steel
Professor Jasprit Singh
Associate Professor Cagliyan Kurdak

© Dong Sun 2009
All Rights Reserved

To my parents,

Youping Shen and Xiaolan Sun

Acknowledgements

"So, professor, can I ask how many years it takes to graduate?" I don't know why I kept asking each professor this question since I actually understand how naive it is after almost two and half years of struggle in graduate school. I wasn't prepared for the estimate of two years when Professor Ted Norris gave me the answer about 2 years ago. Although to be honest, I never took it seriously and became quite careless about my graduating date after joining the group. However, I am very grateful for this answer from Ted, not because he kept his promise and graduated me on time, but because he encouraged me during helpless and hopeless moment and kept me on track. It's his optimistic attitude toward research and life that has kept me energized and focused throughout my graduate study. As an inspiring advisor, he always led me to in the right direction. At the same time he allowed me great freedom to initiate projects and encouraged me to work with my own imagination and creativity. Without his academic excellence and continuous encouragement, I could not imagine this thesis work ever becoming a reality.

I want to give special thanks to Professor Duncan Steel, who is my first advisor and the only person who served as a member of both my prelim and defense committees. I am so lucky to have joined Duncan's lab during the early stages of my program to have received systematic optics training in his lab. Although I switched group later, Duncan kept looking after me and generously offered me help and support during my entire

graduate life. I can still remember Duncan's patience when I told him I am not sure what I am really interested in and don't think "interest" is that important. He always had a big smile on his face and kept encouraging me during the tough times. I think what I will benefit most after graduate school from Duncan and Ted's education, is not just the knowledge, but the beautiful philosophy toward life and research they conveyed me to every day.

I would like to thank Professor P.C. Ku, who is my second advisor and who guided me through my prelim work on the slow light project. One year's work with P. C. broadened my knowledge of engineering and device fabrication, which is an excellent compliment to my physics background. He also invested a large effort in improving my weakness in scientific communication and numerical simulation, from which I benefited a lot in my later graduate studies. I still clearly remember the night I worked with him to meet the deadline of my first conference paper and his patience with two years of back and forward modification of my first first-authored journal paper. I was impressed by his rigorous attitude and his constant pursuit of perfection.

I am so lucky to have worked in the excellent laboratory and office environment in Randall provided by Professor Roberto Merlin. Also, as co-chair of my defense committee, Roberto is another important person to whom I'd like to express my gratitude. I should apologize to him for having taken up so much precious laser time in the last couple of years, time that should have belonged to his students so that they could have greatly accelerate their own research.

I also would like thank my other two committee members: Professor Jasprit Singh and Professor Cagliyan Kurdak for their interest in and contributions to my thesis work. I

enjoyed the nice trip with Cagliyan to this year’s APS March Meeting; it’s so impressive that he, as a professor, took care of every aspect, including driving during the trip. Jasprit is such a great lecturer. I learned a lot about semiconductors from his class. I also want to thank Professor Luming Duan for serving on my prelim committee and his generous and selfless help in my early graduate life.

For the work in this thesis, I give my thanks to our collaborators: Professor Walt de Heer, Professor Phillips First and Dr. Claire Berger’s group in Georgia Institute of Technology for their scientific support and enthusiasm. A large portion of the success of my thesis work is due to the world-best epiaxial graphene samples provided by them. I am also grateful to Professor John Sipe’s group at the University of Toronto for their theoretical support and useful comments on our experimental results. I should also thank their students: Dr. Xiaosong Wu, Mike Sprinkle, Ming Ruan, Julien Rioux for their technical assistance and valuable discussion. I will miss our numerous conference calls, meetings and lunches in San Jose, Atlanta and Pittsburge.

One of the wonderful things about working in those groups is that I always received excellent training from a group of talented mentors. Among these mentors, the first I want to thank is my colleague Chuck Divin who worked with me together to make the coherent control in this thesis. Actually, Chuck was also my mentor when I joined the lab. I could never have started my work in the lab so quickly and smoothly without his patient training and help. He has genius ability detected problems and made the experiment work every time when there seemed no solution, and I am so lucky to have had Chuck working with me on the coherent control experiment. Without him, I can hardly imagine any of the work being accomplished so fast.

I'd like to thank my mentors Jun Cheng and Qiong Huang for their training on the basic optics when I was in Duncan's lab. When I started with them, I had never been in a real lab; it's their excellence and patience that allowed me to build the basic skills that I am using everyday in my experiments. They also kindly provided me technical support and loaned me equipments whenever I needed it during the entire past 4 years.

I also want to thank John Wu who came back from Intel just to train me on pump probe spectroscopy on graphene and Hyunyong Choi for his training on OPA and DFG. I also can't forget Paul Jacobs in Professor Merlin's group, who patiently tought me how to use the complex Magnetic cryostat, for which he probably has never got any credit before.

Special thanks go to Steve Katnik, who trained me on the maintenances of the laser and shared his knowledge and experience using the laser. Also his hard work on the maintenances of the laser system guaranteed our high quality experimental work during the past years.

I have special mentions here: Dr. Guoqing Chang in Ted's group, who was always the first person I turned for help whenever I had an optics puzzle; Dr. Yongjian Han from Luming's group, who knows so much math and gave me so much help on theory and simulation; Dr. Xiaodong Xu from Duncan's group, who always came up with excellent technique solutions in the spectroscopy experiments. I am grateful for what I learned during discussions with them.

I feel extremely lucky to have worked with my past and current labmates. They are Dr. Jingyong Ye, Dr. Guoqing Chang, Dr. John Wu, Dr. Hyunyong Choi, Chuck Divin, Yuchung Chang, Moussa Ngom, Malakeh Musheinish, Jessica Ames, Jae-Hyun Kim, Yunbo Guo, Eric Tkaczyk and Pacha Mongkolwongrojn in Ted's group; Dr. Jun Cheng,

Dr. Qiong Huang, Dr. Yanwen Wu, Dr. Xiaodong Xu, Eric Kim and Hailing Cheng in Duncan's group; Dr. Hongbo Yu, Luke Lee, Taeil Jung and Min Kim in P.C.'s group; Dr. Paul Jacobs, Ilya Vugmeyster, Lei Jiang, Jingjing Li and Andrea Bianchini in Roberto's group. I greatly benefited from the inspiring academic discussions and pleasant personal communications that I had with them. I have special thanks go to Moussa Ngom, Jessica Ames and Pacha Mongkolwongrojn for good amount of time proof-reading my thesis.

I want to thank my friends and colleagues in physics: Jing Shao, Jiangang Hao, Guindar Lin, Chun Xu, Zhuang Wu, Rui Zhang, Hao Fu, Ming Liu, Meng Cui, Bing Wang, Daiming Wang, Song Ge, Zetian Mi, Jun Yang, Xiaochuang Bi and many others, for their help and friendship. They made the past five years one of the best times in my whole life.

The CUOS has provided a second-to-none environment for my research. I would like to extend my thanks to CUOS staff members, Linda Owens, Bett Weston, and Debra Dieterle.

I'd also like to take this opportunity to thank my undergraduate group and friends in China, especially my undergraduate advisor Professor Zhengwei Zhou, Professor Guangcan Guo also my friends Professor Lixin He, Professor Chuanfeng Li in USTC and many others for their training, support, help and also friendship.

Finally, I would like to thank my parents for their selfless love and support. Although they know nothing about physics, they gave me an optimistic attitude toward work and life, from which I have been benefiting and will continue to benefit from throughout my life; they are always the inspiration for me to face challenges and continue my academic pursuits.

Table of Contents

Dedication……………………………………………………………………………ii

Acknowledgements …………………………………………………………………...iii

List of Figures…………………………………………………………………………xii

Abstract………………………………………………………………………………..xv

Chapter

I. Introduction to Graphene and Its Electronic Properties…………………………......1

1.1 Graphene and Its Fabrication…………………………………………………2

1.1.1 Exfoliated Graphene……………………………………………...3

1.1.2 Chemical Derived Graphene……………………………………...4

1.1.3 Epitaxial Graphene………………………………………………..5

1.1.4 Chemical Vapor Deposition Grown Graphene……………………...5

1.2 Electronic Properties of Graphene……………………………………………6

1.2.1 Tight-binding Calculation…………………………………………...6

1.2.2 Dirac Fermions Properties……………………………………….…8

1.3 Epitaxial Graphene…………………………………………….…………..11

1.3.1 Fabrication of Epitaxial Graphene…………………….………...11

1.3.2 Atomic and Electronic Structure of Epitaxial Graphene…………..14

1.3.3 Epitaxial C-face Graphene Behaves as Multilayer Graphene……...16

1.4 Toward Graphene Electronics and Optoelectronics Devices………………...17

1.5 Dissertation Chapter Outlines………………………………………………..18

II. Dynamic Optical Conductivity of Graphene and Transfer Matrix Approach………...22

2.1 Dynamic Conductivity of a Single Graphene Layer…………………………23

2.1.1 Intraband Complex Dynamic Conductivity………………………..24

2.1.2 Interband Complex Dynamic Conductivity………………………..25

2.1.3 Low Frequency Limit of Dynamic Conductivity…………………..26
2.2 Transfer Matrix of Ultrathin Layer with Dynamic Conductivity σ…………27
2.2.1 Transfer Matrix of Normal Incidence……………………………...27
2.2.2 Transfer Matrix with Oblique Incidence Angle……………………28
2.3 Transfer Matrix Method……………………………………………………...29
III. Time-Resolved Differential Transmission Spectroscopy……………………………32
3.1 Differential Transmission Spectroscopy……………………………………..32
3.2 Laser System……………………………………………………………………33
3.2.1 Ti: Sapphire Oscillator……………………………………………..33
3.2.2 Ti: Sapphire Regenative Amplifier………………………………...34
3.2.3 White Light Super-Continuum Generation………………………...36
3.2.4 Optical Parametric Amplifier………………………………………37
3.2.4.1 Parametric Amplification………………………………...38
3.2.4.2 Infrared OPA system……………………………………..41
3.2.5 Differential Frequency Generator…………………………………42
3.3 Experiment Setup for Ultrafast Pump-Probe Spectroscopy…………………45
3.3.1 Ultrafast Non-degenerate Pump Probe Spectroscopy……………...45
3.3.2 Ultrafast Degenerate Pump Probe Spectroscopy…………………..47
IV. Ultrafast Spectroscopy on Epitaxial Graphene………….……………………...49
4.1 Ultrafast Relaxation of Hot Dirac Fermions…………………………………50
4.1.1 Experimental Setup………………………………………………...50
4.1.2 Experimental Results………………………………………………52
4.1.3 Interpretation of the Results………………………………………..54
4.2 Doping Profile and Screening Length………………………………………..62
4.2.1 Experimental Setup………………………………………………...64
4.2.2 Experimental Results………………………………………………66
4.2.3 Interpretation of the Results………………………………………..69
4.3 Interlayer Thermal Coupling of Hot Electrons………………………………71
4.3.1 Experimental Setup………………………………………………...72
4.3.2 Experimental Results………………………………………………74
4.3.3 Interlayer Thermal Coupling Mechanism…………………………76

4.4 Polarization Dependence……………………………………………………77
4.4.1 Experimental Setup……………………………………………...77
4.4.2 Experimental Results……………………………………………78
4.4.3 Experimental Discussion………………………………………..79
4.5 Electron Cooling in Epitaxial Graphene……..…………………………80
4.6 Pump Power Dependence—Hot Phonon Effect………………………..84
4.6.1 Experimental Setup……………………………………………...84
4.6.2 Experimental Results……………………………………………84
4.6.3 Experimental Fitting at Low pump Excitation….………………87
4.7 Probing the New Electromagnetic Mode in Graphene…………….…..89
V. Coherent Controlled Photocurrent in Epitaxial Graphene...........................………94
5.1 Introduction……………………………………………………………..94
5.2 Tight Binding Calculation………………………………………………96
5.2.1 Current Injection Rate…………………………………………..96
5.2.2 Tensor Element……………………………………………….....97
5.2.3 Polarization Effect………………………………………………98
5.2.4 Bad Electrons……………………………………………………98
5.3 Dynamics of Injected Coherent Controlled Current……………………..100
5.4 Experiment Setup and Detection Techniques……………………………101
5.4.1 Free Space Electro-optics Sampling of THz Field with ZnTe…....102
5.4.2 Experimental Setup………………………………………………104
5.5 Experimental Results and Discussion……………………………………107
5.5.1 Coherent Controlled Photocurrent in Epitaxial Graphene..............107
5.5.2 THz Signal Strength………………………………………………108
5.5.3 Polarization of the Emitted THz…………………………………109
5.5.4 Fundamental Beam Power Dependence…………………………112
5.5.5 Second Harmonic Beam Power Dependence……………………114
5.5.6 Sample Dependence……………………………………………....116
5.5.7 The Effect of Pre-injected Hot Carriers…………………………..118
5.6 Optical Effect……………………………………………………………..126
5.6.1 Spectrum Bandwidth in Second Harmonic Generation…………..126

5.6.2 Pulse Broadening and Temporal Walk-off……………………….127
5.6.3 Current Injection with Chirped and Delayed Pulses……………...128
5.7 Conclusions……………………………………………………………129
VI. Contributions, Conclusions, and Future Work…………………………………...133
6.1 Contributions and Conclusions……………………………………………..133
6.2 Future work……………………………………………………………134
6.2.1 Magneto Ultrafast Nonlinear Spectroscopy………………………134
6.2.2 Exfoliated and CVD Grown Graphene, Graphene Bilayer……….136
6.2.3 Nonlinear Frequency Multiplication……………………………...137
6.2.4 Generation and Probe the Pseudospin/Valley Polariztion………..138
6.2.5 Reflection of Coherent Controlled Ballistic Current……………..138
6.2.6 Ballistic Dirac Fermions in Magnetic Field………………………139
6.2.7 Toward Graphene Based Optoelectronics Device………………..139
Appendices…………………………………………………………………...141

List of Figures

Figure

1.1 Lattice Structure and Brillioun Zone of Graphene……………………………………7

1.2 Graphene Band Structure..…………………………………………………………...10

1.3 Terahedron Crystal Structure of SiC…………………………………………………12

1.4 Polytypes of SiC……………………………………………………………………...13

1.5 Interface Geometry…………………………………………………………………...14

1.6 Calculated Band Structure for Three Forms of Graphene…………………………16

2.1 Schematic Diagram of Oblique Incident Angle……………………………………29

3.1 Ti: Sapphire Oscillator……..34

3.2 Ti: Sapphire Regenerative Amplifier...35

3.3 OPA Schematic...37

3.4 OPA Phase Matching Angle…………………………………………………………40

3.5 Parametric Amplification……………………………………………………………..41

3.6 OPA Signal Wavelength Characteristics……………………………………………..42

3.7 DFG Schematics……………………………………………………………………...43

3.8 DFG Phase Matching Angle…………………………………………………………44

3.9 DFG Wavelength Characteristics……………………………………………………44

3.10 DFG Tuning Characteristics…………………………………………………………45

3.11 Non-degenerate Experiment Setup…………………………………………………...45

3.12 Degenerate Experimental Setup………………………………………………………47

4.1 Sample Structure and Energy Dispersion Curve……………………………………..51

4.2 DT Spectrum and Zero Crossings…………………………………………………….53

4.3 Temperature-dependent DT spectrum………………………………………………..54

4.4 DT Signal Simulation……………………………………………………………...58
4.5 Sample Inhomogeneity………………………………………………………………59
4.6 DT Crossing Points Shift with the Number of Undoped Layers…………………..61
4.7 Sample Structure and DT Crossings…………………………………………………68
4.8 DT Signal Simulation……………………………………………………………...69
4.9 Screening Length Fitting…………………………………………………………...71
4.10 Sample Structure, Energy Dispersion Curve and Experimental Scheme…………73
4.11 Degenerate Pump-probe DT Time Scan…………………………………………...75
4.12 Rising Time of the Interlayer Thermal Coupling…………………………………76
4.13 Polarization Dependence above the Fermi Level…………………………………79
4.14. Polarization Dependence below the Fermi Level……..…………………………79
4.15. The role of Graphene Layers in Contribution to DT Signal………………………83
4.16 Simulated DT/T Time Scan Curve Through Transfer-matrix Method……………85
4.17 Low Pump Power Dependence……………………………………………………86
4.18 High Pump Power Dependence ……………………………………………………87
4.19 Low Pump Power Dependence Analysis…………………………………………..88
4.20 Experimental Setup for Probing TE Mode………………………………………...91
5.1 Schematic Diagram of General Coherent Control…………………………………95
5.2 Schematic Diagram of Coherent Control in Epitaxial Graphene…………………99
5.3 Experimental Setup for Coherent Control Experiment with Pre-pulse Excitation of Background Hot Carriers……………………………………………………...106
5.4 Phase Controlled THz Emission from Injected Photocurrent……………………108
5.5 THz Field *vs* the Polarizer Orientation…………………………………………...110
5.6 THz Field *vs* Wave Plate Main Axis Orientation……………………………...111
5.7 Fundamental Beam Power Dependence…………………………………………113
5.8 Second Harmonic Beam Power Dependence……………………………………115
5.9 Sample Dependence………………………………………………………………117
5.10 Experimental Setup for Coherent Control Experiment with In-situ Differential Transmission Measurement……………………………………………………...119
5.11 Coherently Controlled THz Waveform…………………………………………...121
5.12 Differential THz Signal Waveform………………………...…………………..122

5.13 Differential THz Signal and In-situ Mid-IR Pump-probe Signal…………………123
5.14 Power Dependent THz Probe dt/t Data at Different Temperature………………..124
5.14 Normalized Differential THz Signal and dt/t Signal……………………………...125
6.1 Landau Level Energy *vs* Landau Level Number under Different Magnetic Fields.136

Abstract

Hot Dirac Fermion Dynamics and Coherently Controlled Photocurrent Generation in Epitaxial Graphene

By
Dong Sun

Co-Chairs: Theodore B. Norris and Roberto D. Merlin

We investigate the ultrafast relaxation dynamics of hot Dirac Fermionic quasiparticles in multilayer epitaxial graphene using ultrafast optical differential transmission (DT) spectroscopy. We observe DT spectra which are well described by interband transitions with no electron-hole interaction. Following the initial thermalization and emission of high-energy phonons, electron cooling is determined by electron-acoustic phonon scattering. The spectra also provide strong evidence for the multilayer structure and a measure of the doping profile, thus giving insight into the screening length in thermally grown epitaxial graphene on SiC. From the zero crossings of the differential transmission (DT) signal tails, we can resolve 4 heavily doped layers with Fermi levels of 361meV, 214meV, 140meV, 93meV above the Dirac point in the sample, respectively. The screening length is determined to be 2-3 layers in carbon face grown epitaxial graphene. The measured DT spectrum can be well explained by a dynamic conductivity simulation

incorporating the in plane disorder and an elevated lattice temperature. We observed evidence for thermal coupling of hot carriers between graphene layers by ultrafast degenerate pump-probe spectroscopy and determined the interlayer thermal coupling time to be below the time resolution of the experiment (100fs).

A second series of experiments focuses on the generation of ballistic electric currents in unbiased epitaxial graphene at 300 K via quantum interference between phase-controlled cross-polarized fundamental and second harmonic 220- fs pulses. The transient ballistic currents are detected via the emitted terahertz radiation. Due to graphene's special structural symmetry, the injected current direction can be well controlled by the polarization of the pump beam in epitaxial graphene. The results match theoretical calculations showing that the current direction can be controlled through changing the relative phase between two pump beams. By pre-injecting background hot carriers into the system, we study the enhancement of hot carriers in phase breaking scattering due to hot carriers and the results show that this scattering rate increased monotonically with the hot electron temperature. This all-optical current injection provides not only a non-contact way of injecting directional current into graphene, but also new insight into optical and transport processes in epitaxial graphene.

Chapter I

Introduction to Graphene and Its Electronic Properties

Graphene is an individual atomic plane of carbon atoms densely packed in a honeycomb lattice, or it can be viewed as a single layer of bulk graphite. It has attracted a great deal of interest since this ideal two-dimensional physical system was isolated successfully in 2004 by scotch tape [1].

As the first truly two dimensional system ever made by the human beings, graphene exhibits unique physical properties: the carriers in graphene follow the 2 dimensional Dirac equation instead of the usual Schrödinger equation, which makes it an excellent condensed matter analog of quantum electrodynamics. So graphene attracts considerable interest in the field of fundamental physics[2, 3]. On the other hand, due to its unique electronic properties and its compatibility with the existing CMOS fabrication technologies, graphene has great potential as a platform for carbon-based nanoelectronics and this has further amplified interest in this material in the electronics community [4].

For graphene based high-speed electronic devices such as field-effect transistors, p-n junction diodes and photonic devices, understanding the carrier dynamics of graphene will be critical to its device applications. In steady-state transport measurements, the transport of carriers is controlled by the electrons near the Fermi level; transport in high speed devices, however, is determined by the dynamics of hot carriers. The investigation of hot carrier effects thus plays

a central role in device physics, and provides a key link between fundamental physics and high-speed devices.

On the other hand, optical spectroscopy has unique strengths in providing fundamental information about nonequilibrium, nonlinear and transport properties of semicondcutors. If combined with femtosecond laser pulses it can provide new insights into different aspects of semiconductors including photoexcitated non-equilibrium carrier distribution functions and the dynamics of the relaxation of these excitations. It also provides the ability to investigate the nonlinear properties in semiconductors such as many-body effects, coherent effects and dephasing phenomena. Part of this dissertation is a discussion of some of these aspects in epitaxial graphene as measured through the use of ultrafast spectroscopy.

In this chapter, I'll start with an introduction to various techniques for the fabrication of graphene, followed by a discussion of the basic electronic properties of graphene that are related to this thesis. Since all the experiments in this dissertation have been performed on samples of epitaxial graphene, a structurally different material from exfoliated graphene, I have included a separate section to describe epitaxial graphene in more detail. At the end, we will specify the motivation and outline of this thesis.

1.1 Graphene and Its Fabrication

When one presses a pencil against a sheet of paper, among those graphene stacks, there should be individual graphene layers. Despite this no one actually expected graphene to exist in a free state because from the theoretical aspect, Mermin and Wagner concluded that, because of the periodic order of carbon, the atoms cannot be maintained in an infinite two-dimensional crystal about 40 years ago [5, 6]. In contrast to these predictions are recent observations of individual layers derived from layered materials [1]. Later experiments and

theoretic work explained this contradiction and revealed that a free-hanging graphene sheet is buckled rather than flat [7, 8]. The discovery of the first graphene flake is not easy, since it's either expected or there exists any experimental tools exist to search for graphene among the pencil debris covering macroscopic areas. Graphene was eventually discovered due to a subtle optical effect created on top of a chosen SiO_2 substrate with a certain thickness that allows its observation under an ordinary optical microscope [1].

1.1.1 Exfoliated Graphene

So far the samples most widely used by experimental groups are obtained by micromechanical cleavage of bulk graphite, the same technique that allowed isolation of graphene for the first time [1]. This relatively simple and low cost technique can provide individual samples for research purposes with high-quality graphene crystallites up to several hundred micrometers in size, which is sufficient for most research purposes. The critical ingredient for success with this method was the observation that graphene becomes visible in an optical microscope if placed on top of a Si wafer with a carefully chosen thickness of SiO_2. The visibility is due to an interference-like contrast with respect to an empty wafer. For this purpose, a Si substrate with t = 300 nm is used. Only a 5% difference in SiO_2 thickness (315 nm instead of the current standard of 300 nm) can make single-layer graphene become completely invisible. A color map of few layer graphene on this substrate is provided in the supplementary material of reference [1]. To make a larger graphene flake, careful selection of the initial graphite material (so that it has largest possible grains) and the use of freshly cleaved and cleaned surfaces of graphite and SiO_2 are necessary.

The micromechanical cleavage method is simple and produces high-quality graphene crystallites, which is excellent for research purposes. However, the production of single layer

graphene films this way is random and the maximum size of the flake is quite limited. With this method there is no possibility of quality control for mass production and industrial fabrication of graphene based chips. For large scale device application purposes, more efficient fabrication methods are expected.

1.1.2 Chemically Derived Graphene

Even before the success of the micromechanical cleavage method, there were significant efforts towards the chemical exfoliation of graphite. To this end, bulk graphite was intercalated so that graphene planes became separated by layers of intervening atoms or molecules [9]. In certain cases, large molecules could be inserted between atomic planes providing greater separation than a graphene layer so that the resulting compounds could be considered as isolated graphene layers embedded in a 3D matrix; however, this is essentially a new 3D material. In recent years, major progress has been made in the development of chemically derived graphene nanoribbons [10] and graphene-polymer composites [11]. The chemically derived graphene nanoribbons can be sub-10-nanometers thick and open enough bandgap to turn off a graphene based transistor at room temperature. However, the mobility of this device is only 200 cm^2/Vs [10]. Chemically derived graphene-oxide [12] also shows a bandgap opening and an epitaxial-graphene/graphene-oxide junction device has been demonstrated with 850 cm^2/Vs mobility [13]. Although chemical fabrication of graphene is cheap and provides mass production, the chemically derived graphene nanoribbons and graphene-polymer composites share the same problem with carbon nanotubes in terms of real device applications: the graphene suspended in the solvents is hard to locate and fabricate for device mass production.

1.1.3 Epitaxial Graphene

Graphene grown epitaxially on single crystal silicon carbide can be patterned using standard lithography methods and thus is compatible with current CMOS fabrication technologies. The method is very simply to heat SiC in ultrahigh vacuum. The Si atoms will then be desorbed from SiC and leave carbon to form graphene. Although epitaxial graphene grown this way has multiple layers, it is a different material from exfoliated graphene. It may seem that epitaxial graphene is simply ultrathin graphite, but the stacking order is very different from graphitic A-B stacking. The epitaxially grown material has a special rotational stacking order and exhibits the same linear dispersion curve as seen in single layer graphene. Thus these chemically synthesized samples look more like multiple graphene layers than graphite. This will be discussed further in the Section 1.3 of this Chapter. Experimentally, the charge carriers in epitaxial graphene are found to be chiral [14] and the band structure is clearly related to the Dirac cone [15, 16]. Epitaxial graphene possesses the unique electronic structure of ideal single layer graphene but due to its mass producibility and compatibility with current manufacturing technology, it is the most promising form of graphene for use in electronics and optoelectronic devices. Since this thesis focuses on epitaxial graphene, there will be a separate section covering the fabrication and electronic properties of epitaxial graphene later.

1.1.4 Chemical Vapor Deposition Grown Graphene

Although chemical vapor deposition (CVD) has been used to grow carbon nanotubes for a long time, progress in growing graphene by CVD has only started recently [17-19]. Using this method, few-layer graphene can be grown via ambient pressure methane-based CVD on polycrystalline Ni films deposited on Si/SiO_2. Large area (~cm^2) films of single to few-layer

graphene can be fabricated and the films transferred to nonspecific substrates. The films are continuous over the entire area and can be patterned lithographically or by pre-patterning the underlying Ni film. Chemical vapor deposition grown graphene opens another promising avenue beyond epitaxial graphene for device applications. However, the single- or bilayer regions are 20 μm in lateral size and the details of their properties have yet to be characterized.

1.2 Electronic Properties of Graphene

The electronic properties of graphene have been reviewed in detail by Castro Neto et al. [20]. Here I review two important concepts central to this dissertation. First, I review the tight-binding calculation for the electronic structure of a hexagonal carbon lattice. This is followed by a discussion of the unique properties of a Dirac Fermion in graphene.

1.2.1 Tight-binding Calculation

Graphene is made out of carbon atoms arranged in a hexagonal structure. The structure can be seen as a triangular lattice with a basis of two atoms per unit cell as shown in Fig. 1.1. The lattice vectors can be written as:

$$\mathbf{a}_1 = \frac{a}{2}(3, \sqrt{3}), \mathbf{a}_2 = \frac{a}{2}(3, -\sqrt{3}), \tag{1.1}$$

where $a \approx 1.42\,\mathring{A}$ is the carbon-carbon distance. The reciprocal lattice vectors are given by:

$$\mathbf{b}_1 = \frac{2\pi}{3a}(1, \sqrt{3}), \mathbf{b}_2 = \frac{2\pi}{3a}(1, -\sqrt{3}). \tag{1.2}$$

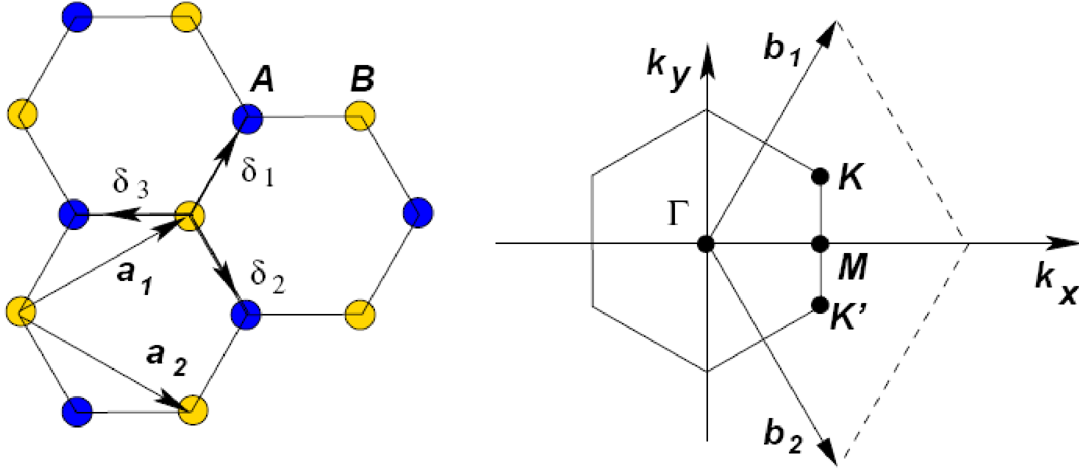

Figure 1.1: Lattice Structure and Brillioun Zone of Graphene. Left: Lattice structure of graphene, made out of two interpenetrating triangular lattices. $\mathbf{a}_1$ and $\mathbf{a}_2$ are the lattice unit vectors, and $\boldsymbol{\delta}_i$, i=1, 2, 3 are the nearest neighboring vectors; Right: corresponding Brillouin zone. The Dirac cones are located at the K and K′ points. Figure taken from ref. [21].

Two points K and K' at the corners of graphene's Brillouin zone (BZ) are the so called Dirac points which are of particular importance for the physics of graphene. Their positions in momentum space are given by:

$$\mathbf{K} = (\frac{2\pi}{3a}, \frac{2\pi}{3\sqrt{3}a}), \mathbf{K}' = (\frac{2\pi}{3a}, -\frac{2\pi}{3\sqrt{3}a}). \tag{1.3}$$

The three nearest neighbor vectors in real space are given by:

$$\boldsymbol{\delta}_1 = \frac{a}{2}(1, \sqrt{3}), \boldsymbol{\delta}_2 = \frac{a}{2}(1, -\sqrt{3}), \boldsymbol{\delta}_1 = -a(1,0). \tag{1.4}$$

While the six second-nearest neighbors are located at:

$$\boldsymbol{\delta}_1^{'} = \pm a_1, \boldsymbol{\delta}_2^{'} = \pm a_2, \boldsymbol{\delta}_3^{'} = \pm(a_2 - a_1). \tag{1.5}$$

The energy bands derived from the tight-binding Hamiltonian that considers electron hopping both to nearest and next nearest neighboring atoms have the following form [22]:

$$\begin{aligned} &E_{\pm}(\mathbf{k}) = \pm t\sqrt{3 + f(k)} - t' f(k), \\ &f(\mathbf{k}) = 2\cos(\sqrt{3}k_y a) + 4\cos(\frac{\sqrt{3}}{2}k_y a)\cos(\frac{3}{2}k_x a), \end{aligned} \tag{1.6}$$

where the plus and minus signs apply to the upper (π) and lower (π^*) band, respectively. $t\,(\approx 2.8eV)$ is the hopping energy of the nearest neighbor and t' is the hopping energy of the next nearest neighbor. Fig. 1.2 shows the full band structure of graphene. When t' is zero, the spectrum is symmetric around zero energy. For a finite value of t', Eq. 1.2 can be expanded close to the Dirac points as $\mathbf{k} = \mathbf{K} + \mathbf{q}$, with $|q| << |K|$ [22]:

$$E_{\pm}(\mathbf{q}) \approx \pm v_F\,|\mathbf{q}| + \varepsilon((q/K)^2), \tag{1.7}$$

where $\mathbf{q}$ is the momentum measured relative to the Dirac points and v_F represents the Fermi velocity, given by $v_F = 3ta/2$, with a value $v_F \approx 1\times10^6\,m/s$. The Fermi velocity at these Dirac points is a constant which doesn't depend on the energy or momentum as do typical semiconductors with parabolic energy dispersion curves. This result was first obtained by Wallace [22].

The expansion around Dirac points including t' up to second order in q/K is given by:

$$E_{\pm}(\mathbf{q}) \approx 3t' \pm v_F\,|\mathbf{q}| - \left(\frac{9t'a^2}{4} \pm \frac{3ta^2}{8}\sin(3\theta_{\mathbf{q}})\right)|\mathbf{q}|^2, \tag{1.8}$$

where

$$\theta_{\mathbf{q}} = \arctan\left(\frac{q_x}{q_y}\right), \tag{1.9}$$

is the angle in momentum space. Hence the presence of next nearest neighbor hopping shifts the energy of the Dirac points and breaks electron-hole symmetry. Up to the order of $(q/K)^2$ the dispersion depends on the direction in momentum space and has three-fold symmetry. This is called trigonal warping of the electron spectrum [9, 23].

1.2.2 Dirac Fermion Properties

The linear energy dispersion shown in Eq. (1.6) resembles the energy dispersion of ultra-

relativistic particles; these particles are quantum mechanically described by the massless Dirac equation. The effective mass is thus zero due to the linearity of the dispersion curve and at the first quantized language, the two-component electron wavefunction, closed to the $\mathbf{K}$ point, obeys the 2D Dirac equation:

$$-iv_F\boldsymbol{\sigma}\cdot\nabla\psi(\mathbf{r}) = E\psi(\mathbf{r}) \ , \tag{1.10}$$

The wavefunction, in momentum space, for the momentum around $\mathbf{K}$ has the form:

$$\psi_{\pm,\mathbf{K}}(\mathbf{k}) = \frac{1}{\sqrt{2}}\begin{pmatrix} e^{-i\theta_{\mathbf{k}}/2} \\ \pm e^{i\theta_{\mathbf{k}}/2} \end{pmatrix}, \tag{1.11}$$

for $H_{\mathbf{k}} = v_F\boldsymbol{\sigma}\cdot\mathbf{k}$, where the $\pm$ signs correspond to the eigenenergies $E = \pm v_F k$, that is, for the π and π^* band, respectively, and θ_k is given by Eq. (1.9). The wavefunction for the momentum around $\mathbf{K'}$ has the form:

$$\psi_{\pm,\mathbf{K'}}(\mathbf{k}) = \frac{1}{\sqrt{2}}\begin{pmatrix} e^{i\theta_{\mathbf{k}}/2} \\ \pm e^{-i\theta_{\mathbf{k}}/2} \end{pmatrix}, \tag{1.12}$$

for $H_{K'} = v_F\boldsymbol{\sigma}^*\cdot\mathbf{k}$. So the wavefunctions at $\mathbf{K}$ and $\mathbf{K'}$ are related by time-reversal symmetry. If the phase θ_{k} is rotated by 2π , the wavefunction changes sign indicating a phase of π , which is commonly called a Berry's phase. This change of phase by π radians under rotation is a characteristic of spinors and in fact the wavefunction is a two-component spinor.

A relevant quality used to characterize eigenfunctions is their helicity defined as the projection of the momentum operator along the spin direction. The quantum mechanical operator for helicity has the form:

$$\hat{h} = \frac{1}{2}\boldsymbol{\sigma}\cdot\frac{\mathbf{p}}{|\mathbf{p}|}. \tag{1.13}$$

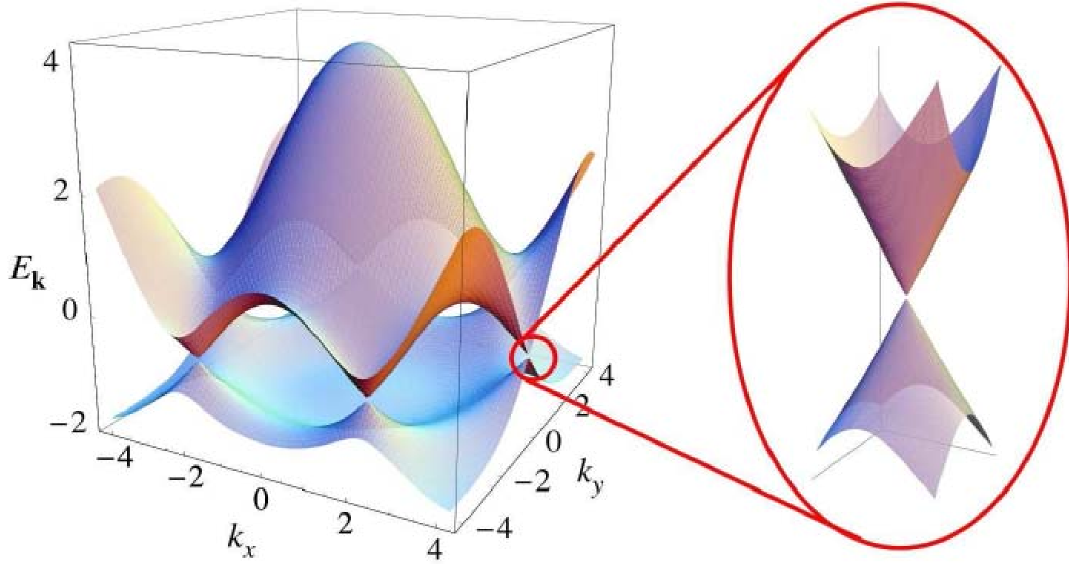

Figure 1.2 Graphene Band Structure. Left: Energy spectrum (in units of t) for finite values of t and t', with $t = 2.7eV$ and $t' = 0.2t$. Right: zoom-in of the energy bands close to one of the Dirac points. Figure taken from ref [21].

It's clear from the definition of $\hat{h}$ that the states $\psi_{\mathbf{K}}(\mathbf{r})$ and $\psi_{\mathbf{K}'}(\mathbf{r})$ are also eigenstates of $\hat{h}$:

$$\hat{h}\psi_{\mathbf{K}}(\mathbf{r}) = \pm\frac{1}{2}\psi_{\mathbf{K}}(\mathbf{r}), \tag{1.14}$$

and an equivalent equation for $\psi_{\mathbf{K}'}(\mathbf{r})$ with inverted signs. Therefore electrons (holes) have a positive (negative) helicity. Eq. (1.13) implies that $\boldsymbol{\sigma}$ has its two eigenvalues either in the direction of or against the momentum $\mathbf{p}$. This property says that the states of the system close to the Dirac point have well defined chirality or helicity. Since chirality is not defined in regards to the real spin of the electron, it's also called pseudo-spin. The helicity values are good quantum numbers as long as the Hamiltonian is valid. Therefore the existence of helicity quantum numbers holds only as an asymptotic property, which is well defined close to the Dirac points $\mathbf{K}$ and $\mathbf{K}'$. Either at larger energies or due to the presence of a finite t', the helicity stops being a good quantum number.

The tight-binding structures of bilayer graphene are addressed in reference [24] and are not

considered further in this dissertation. There are two major features of bilayer graphene that are different from single layer graphene: first, the dispersion relationship is no longer linear; second, there are two closed parabolic bands instead of one.

1.3 Epitaxial Graphene

Epitaxial graphene, grown by high temperature desorption of Si from SiC, has a very different structure from that of an exfoliated graphene sheet and thin graphite; they have similarities in some respects, but they are essentially different materials. In this section, I'll give detailed descriptions of epitaxial graphene covering various aspects including fabrication, atomic structures and electronic structures.

1.3.1 Fabrication of Epitaxial Graphene

Epitaxial graphene is grown on Silicon Carbide when it's heated to about 1300 °C in ultra-high vacuum (UHV) or moderate vacuum conditions using ovens with controlled background gas. The Silicon Carbide is hydrogen etched beforehand to remove polishing scratches to obtain large atomically flat terraces. The epitaxial growth is established by examining the low energy electron diffraction (LEED) pattern after various growth times [4, 15].

SiC is a wide-bandgap, compound semiconductor. It has high breakdown field, electron saturation and thermal stability which make it an ideal material for today's high temperature, high power and high frequency device applications. In the prime structure, SiC has a hexagonal frame with a carbon atom situated above the center of a triangle of Si atoms and underneath a Si atom belonging to the next layer as in Fig. 1.3. The distance between neighboring silicon or carbon atoms is approximately 3.08 Å. The carbon atom is positioned at the center of mass of the tetragonal structure surrounded by four neighboring Si atoms so that the distance between a C atom and each of the Si atoms is the same, approximately equal

to 1.89 Å. The distance between two silicon planes is approximately 2.52Å, which is the height of the unit cell [25].

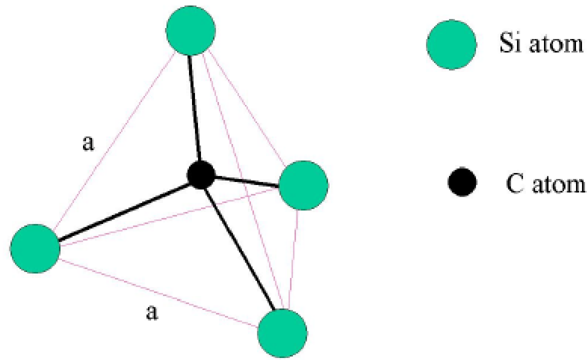

Figure 1.3: Tetrahedron Crystal Structure of SiC. Figure taken from Ref. [21].

SiC has more than 200 polytypes, all of which have the same chemical composition but different stacking orders of the double layers of carbon and silicon atoms (Fig 1.4 a). If the first double layer is called the A position, the next layer will be placed on the B position or the C position according to a closed packed structure (Fig 1.4 b). The different polytypes are constructed through permutations of these three positions. The three most common polytypes are 3C-SiC (cubic, Fig 1.4c), 4H-SiC (hexagonal, Fig 1.4d) and 6H-SiC (hexagonal, Fig 1.4e). 3C-SiC is the SiC polytype with 3 layers per period along the stacking direction with a cubic crystal system. Similarly, 4H-SiC and 6H-SiC are the SiC polytypes with 4 and 6 layers, respectively, per period along the stacking direction with hexagonal crystal systems. Graphene films have been grown on both 6H-SiC and 4H-SiC substrates. The samples grown on 6H-SiC and 4H-SiC can exhibit very different physical properties including substrate induced bandgap opening [26] and nonlinear optical signals [27, 28]. The origin of these differences is still largely unexplored. All the experiments in this dissertation were conducted on 4H-SiC samples.

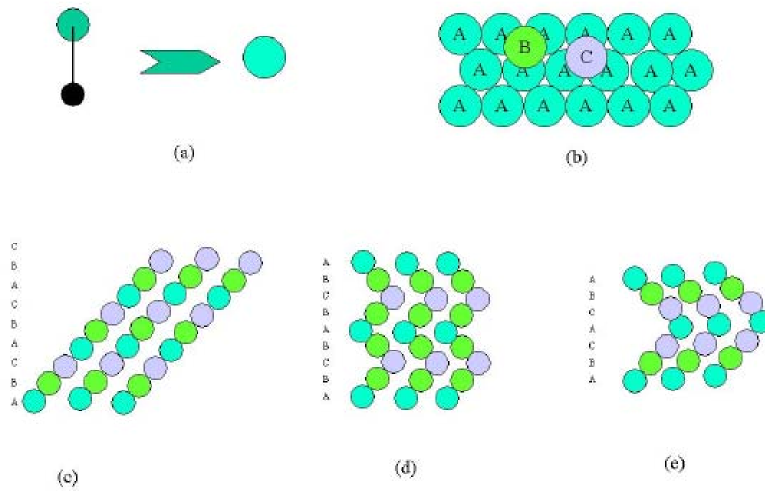

Figure 1.4: Polytypes of SiC. (a) A single carbon and silicon atom are connected together and denoted as a ball. (b) The first layer marked as “A”, there are two equivalent positions, “B” and “C” to form the second layer. (c) 3C-SiC stacking direction (d) 4H-SiC stacking direction (e) 6H-SiC stacking direction. Figure taken from Ref. [21].

It’s clear that the carbon atom is closer to the plane of the three bottom silicon atoms (0.63Å) than to the top silicon atom (1.89 Å), so that cutting SiC perpendicular to the (0001) direction will most likely break the bonds between carbon atoms and the top Si atoms, splitting the crystal into two different faces, one denoted as the C-face $(000\bar{1})$ and the other as the Si-face (0001). Growth on the Si face is slow and terminates after relatively short times at high temperatures. The growth on the carbon face apparently does not self-limit so that relatively thick layers (~4 up to 100 layers) can be achieved. The graphene thickness can be estimated for thin layers by modeling measured Auger-electron intensities or photoelectron intensities. For the relatively thicker multilayer graphene the thickness can be measured via conventional ellipsometry.

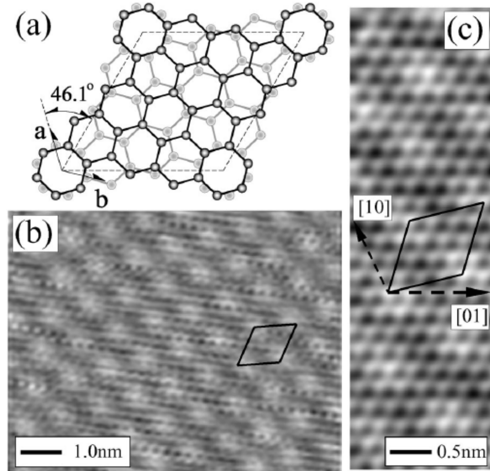

Figure 1.5: Interface Geometry: (a) Schematic $\sqrt{13}\times\sqrt{13}R46.1^{\circ}$ fault pair unit cell (dashed line). Dark circles are *R30* C atoms. Gray circles are C atoms in the $R2^{+}$ plane below, rotated *32.204°* from the top plane. (b) STM image of C-face graphene showing a periodic superlattice with a $\sqrt{13}\times\sqrt{13}$ cell. (c) High resolution STM image of the top view of the $\sqrt{13}\times\sqrt{13}R46.1^{\circ}$ unit cell and the principle graphene directions. Figure taken from ref [29].

1.3.2 Atomic and Electronic Structure of Epitaxial Graphene

The first C layer on top of a SiC surface acts as a buffer layer and allows the next graphene layer to behave electronically like an isolated graphene sheet. There exists strong covalent bonds between the substrate and the first layer; charge can be transferred from SiC to the graphene layers depending on the interface geometry and results in doping of these layers [30]. This charge transfer process doesn't rely on doping of the SiC substrate. It originates from the SiC and graphene interface only. Both first principle calculation and X-ray reflectivity data confirm that the first graphene layer is 1.65 ± 0.05 Å above the last bulk C layer, this bond length is nearly equal to the bond length of diamond (1.54 Å) and suggests that the substrate bond to the first graphene layer is much stronger than a Van der Waals interaction. The next graphene layer is separated from the first by 3.51 ± 0.1 Å (slightly larger than the bulk value of 3.354 Å), so the first layer is strongly bonded to the C face with a well isolated graphene layer above it [30, 31].

As claimed earlier in this chapter, epitaxial graphene is emphatically not simply ultrathin graphite even though it has multiple layers. Experimentally, the charge carriers in carbon face epitaxial graphene are found to be chiral and the band structure is clearly related to the Dirac cone[14-16, 32, 33]. These electronic properties can be explained by the epitaxial graphene structure. Instead of Bernal stacking, as in graphite, it's found that epitaxial graphene grown on the carbon-terminated surface contains rotational stacking faults related to the epitaxial condition at the graphene-SiC interface. A 13×13 graphene cell can be rotated by either 30° or ±2.2° to be commensurate (~0.14% smaller) with a SiC $6\sqrt{3}\times6\sqrt{3}R30^{\circ}$ cell. Two stacked graphene sheets can rotate relative to each other in a number of ways to make the two sheets commensurate. The lowest energy corresponds to rotational angles of $30\pm2.204^{\circ}$. *This bi-layer structure corresponds to a graphene* $\sqrt{13}\times\sqrt{13}(R\pm46.1^{\circ})$ *cell as shown in Fig. 1.5. First principle calculation shows that such faults produce an electronic structure indistinguishable from an isolated single graphene sheet in the vicinity of the Dirac point as shown in Fig 1.6.*

Graphene grown on Si face typically has low electron mobility compared to C face samples. The different interfacial structures and the stacking order can be responsible for the observed electronic property differences. The graphene layer is found to be Bernal stacking instead of rotational stacking on Si face sample. The interface of a Si face sample is not composed of a simple graphene-like layer above a relaxed SiC bilayer, it is comparable to a substantially relaxed SiC bilayer, above which lies a dense carbon layer containing a partial layer of Si atoms which separates it from the graphene film. The carbon density in this intermediate layer is approximately 2.1 times larger than in a SiC bilayer. The bond distance between the Si adatom layer and the first graphene layer is 2.32 ± 0.08 Å. While this distance is short

compared to the interplanar graphene spacing, it is still larger than the corresponding distance measured on C-face graphene, indicating that the graphene on Si-face is less tightly bound to the substrate than C-face graphene. This dense carbon layer with Si adatoms plays the role of the buffer layer and partly isolates subsequent graphene layers from interactions with the substrate [31].

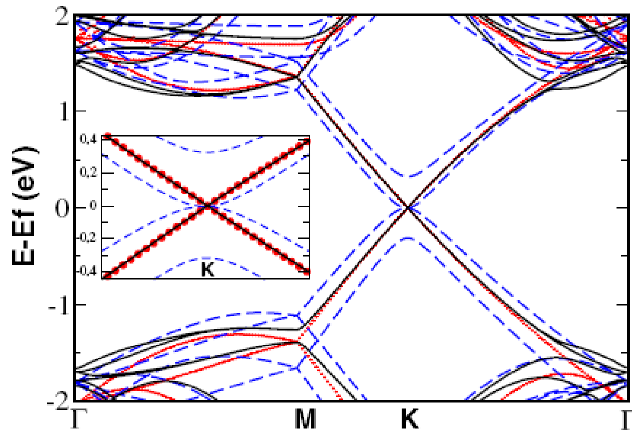

Figure 1.6: Calculated Band Structure for Three Forms of Graphene. (i) Isolated graphene sheet (dots), (ii) Bernal stacked graphene bi-layer (dashed line) and (iii) $R30/R2^{+}$ fault pair (solid line). Inset shows details of band structure at the K-point. Figure taken from ref [30].

1.3.3 Epitaxial C-face Graphene Behaves as Multilayer Graphene

The conclusion from all the facts above is that epitaxial graphene is a form of multilayered graphene that is structurally and electronically distinct from graphite. There is a buffer layer on the SiC substrate and the subsequent interfacial graphene layer starts to recover the electronic properties of graphene. The layer is also heavily doped due to the built-in electric field at the SiC-graphene interface. The number of these heavily doped layers and doping profile will be measured in this dissertation. The doped layers carry most of the current and cause Shubnikov–de Haas (SdH) oscillations C. Berger *et al.* [32]. The charge density of the top layers is more than 2 orders of magnitude smaller, and they are expected to be much more resistive. The magnetoresistant measurement shows the charge density of

3.8×10^{12} electons/cm^2. The undoped layers contribute signal mainly to the Landau level spectroscopy measurement [16, 33]. This measurement suggests $n \approx 1.5*10^{10}$ electrons/cm^2 for the lightly doped layers (or specified as "undoped" layers with respect to those heavily doped). The Landau level spectroscopy also demonstrates that epitaxial graphene consists of stacked graphene layers, whose electronic band structure is characterized by a Dirac cone with chiral charge carriers. It also shows that the low energy part of the spectrum of electrons in graphene is well described by a linear dispersion relation. Any deviation from ideal behavior of the Dirac particles is not observed until 500meV above the Dirac point. At an energy of 1.25eV, the deviation from linearity is around 40meV from magneto-optical transmission spectroscopy [34].

1.4 Toward Graphene Electronics and Optoelectronic Devices

Graphene's mobility μ can exceed 15,000 cm^{2}V^{-1}s^{-1} even under ambient conditions in those exfoliated samples[1-3], and the mobility of epitaxial graphene is refered to be as high as 250,000 cm^{2}V^{-1}s^{-1} from magneto far infrared spectroscopy measurement [35]. Moreover, the observed mobilities depend weakly on temperature and remain high at high doping concentrations (>10^{12} cm^{-2}). Add to this the excellent compatibility of graphene's epitaxial counterpart with current CMOS fabrication technologies and graphene's potential to substitute for silicon in the next generation electronic and far infrared and THz region optoelectronic device materials is unprecedented.

Before jumping to the fabrication of successful graphene based electronics and optoelectronic devices, it would be crucial to understand the related device physics since the fundamental operation of electronic devices is ultimately governed by the carrier dynamics. Specifically, scattering processes such as carrier-phonon interaction and carrier-carrier

scattering determine energy/momentum relaxation and transport properties of devices. For high speed devices, electrons will be accelerated to high energy, thus the dynamics of hot carriers will come into play.

Over the years a diverse community of researchers has used ultrafast spectroscopy to study mainly III-V semiconductors to address problems in making electronics and optoelectronic devices. Mechanisms we can study and measure include hot electron relaxation, various carrier-carrier and carrier-photon scattering, carrier recombination, ballistic acceleration and velocity overshoot. Ultrafast spectroscopy can also be used to probe quantum interference, interband and intersubband transitions and the role of decoherence in dephasing. We can also look into coherent coupling, Rabi oscillations between discrete levels, time-dependent tunneling processes, coherent plasmons and even ballistic electron wave packets.

In part of my research I have utilitzed ultrafast spectroscopy to address problems like hot electron cooling, thermal coupling between layers, carrier-carrier scattering, hot phonon effects and some material properties like the doping profile of multiple layer systems and screening length.

On the other hand, we try to generate directional current by a non-contact all optical method using quantum interference effect in epitaxial graphene. This method serves as a clean method to study the ballistic current scattering mechanism without any side effects due to the electrodes.

1.5 Dissertation Chapter Outline

There are two categories of work in this dissertation: first, I used ultrafast, time-resolved pump-probe techniques to investigate the various electron transport dynamics and material characteristics in epitaxial graphene. Various probe wavelength-, temperature-,

intensity-, and polarization-dependent studies enable a comprehensive understanding of the relaxation of hot Dirac Fermions, electron-electron scattering, electron-phonon coupling, interlayer thermal coupling, doping profile and screening length in carbon face epitaxial graphene. Second, I all-optically generated coherently controlled ballistic currents in epitaxial graphene using quantum interference between phase related fundamental and second harmonic pulses. By pre-injection of background hot carriers, I studied the enhancement of hot carriers in phase breaking scattering processes and correlated this scattering rate to the hot electron temperature.

After introducing the electronic properties of graphene and epitaxial graphene in this chapter, the dynamic conductivity and transfer matrix method is discussed in Chapter 2. This method widely used to explain most of the pump-probe data. The concept of ultrafast pump-probe spectroscopy and the experimental setup will be outlined in Chapter 3. Chapter 4 addresses all the experimental results from ultrafast pump-probe spectroscopy. Chapter 5 describes coherent control related work and results. Final conclusions and future work will be explained in Chapter 6.

References

[1] K. S. Novoselov *et al.*, Science **306**, 666 (2004).

[2] Y. Zhang *et al.*, Nature **438**, 201 (2005).

[3] K. S. Novoselov *et al.*, Nature **438**, 197 (2005).

[4] C. Berger *et al.*, J. Phys. Chem. B **108**, 19912 (2004).

[5] N. D. Mermin, and H. Wagner, Physical Review Letters **17**, 1133 (1966).

[6] N. D. Mermin, Physical Review **176**, 250 (1968).

[7] A. Fasolino, J. H. Los, and M. I. Katsnelson, Nat Mater **6**, 858 (2007).

[8] J. C. Meyer *et al.*, Nature **446**, 60 (2007).

[9] M. S. Dresselhaus, and G. Dresselhaus, Advances in Physics **30**, 139 (2002).

[10] X. Li *et al.*, Science **319**, 1229 (2008).

[11] S. Stankovich *et al.*, Nature **442**, 282 (2006).

[12] S. Gilje *et al.*, Nano Letters **7**, 3394 (2007).

[13] X. Wu *et al.*, Physical Review Letters **101**, 026801 (2008).

[14] X. Wu *et al.*, Physical Review Letters **98**, 136801 (2007).

[15] W. A. de Heer *et al.*, Solid State Communications **143**, 92 (2007).

[16] M. L. Sadowski *et al.*, Physical Review Letters **97**, 266405 (2006).

[17] A. Reina *et al.*, Nano Letters **9**, 30 (2009).

[18] L. Gomez De Arco *et al.*, Nanotechnology, IEEE Transactions on **8**, 135 (2009).

[19] J. Campos-Delgado *et al.*, Nano Letters **8**, 2773 (2008).

[20] A. H. C. Neto *et al.*, Reviews of Modern Physics **81**, 109 (2009).

[21] Z. Song, Ph.D Thesis (Geogia Institue of Technology) (2006).

[22] P. R. Wallace, Physical Review **71**, 622 (1947).

[23] T. Ando, T. Nakanishi, and R. Saito, Journal of the Physical Society of Japan **67**, 2857.

[24] E. McCann, and V. I. Fal'ko, Physical Review Letters **96**, 086805 (2006).

[25] U. Starke *et al.*, Silicon Carbide, Iii-Nitrides and Related Materials **Pts 1 and 2 264**, 321 (1998).

[26] S. Y. Zhou *et al.*, **6**, 770 (2007).

[27] J. M. Dawlaty *et al.*, Applied Physics Letters **92**, 042116 (2008).

[28] P. A. George *et al.*, Nano Letters **8**, 4248 (2008).

[29] J. Hass *et al.*, Physical Review Letters **100**, 125504 (2008).

[30] F. Varchon *et al.*, Physical Review Letters **99**, 126805 (2007).

[31] J. Hass *et al.*, Physical Review B **78**, 205424 (2008).

[32] C. Berger *et al.*, Science, 1125925 (2006).

[33] M. L. Sadowski *et al.*, Solid State Communications **143**, 123 (2007).

[34] P. Plochocka *et al.*, Physical Review Letters **100**, 087401 (2008).

[35] M. Orlita *et al.*, Physical Review Letters **101**, 267601 (2008).

Chapter II

Dynamic Optical Conductivity of Graphene and Transfer Matrix Approach

The optical, DC and Hall conductivities of graphene have been considered in several works [1-9]. Magneto-optical conductivity of graphene has been considered in Gusynin et al [4]. Work without a magnetic field was pioneered by Ando et al [10], who considered the effect of frequency-dependent conductivity of short and long range scatterers in a self-consistent Born approximation. Gusynin et al. [3] describe several anomalous properties of the microwave conductivity of graphene. These properties are directly related to the Dirac nature of quasiparticles. Several analytic formulae for the longitudinal as well as Hall AC conductivity are given in the paper [2]. They also present extensive results for DC properties. Peres et al. [7, 8] treat localized impurities in a self-consistent fashion as well as extended edge and grain boundaries. They also include the effects of electron-electron interactions and self-doping. Since optical conductivity is widely used in this dissertation to describe experimental data from pump-probe differential transmission experiments I have focused a section of this chapter on the deduction of the optical conductivity of a single graphene layer under various conditions. I have also included a section focused on the transfer matrix for ultrathin layers. This important tool is used widely in this dissertation to connect the optical conductivity and the response of graphene layers to probe photons of different wavelengths.

2.1 Dynamic Conductivity of a Single Graphene Layer

Here I concentrate on the optical (dynamic or AC) conductivity of graphene, which will be widely used in this dissertation to explain the experimental phenomena. I start from the expression deduced by Kubo [7]:

$$\sigma(\omega,\mu_c,\Gamma,T)=\frac{je^2(\omega-i2\Gamma)}{\pi\hbar^2}*\left[\frac{1}{(\omega-i2\Gamma)^2}\int_0^\infty \varepsilon\left(\frac{\partial f_d(\varepsilon)}{\partial\varepsilon}-\frac{\partial f_d(-\varepsilon)}{\partial\varepsilon}\right)d\varepsilon-\int_0^\infty \frac{f_d(-\varepsilon)-f_d(\varepsilon)}{(\omega-i2\Gamma)^2-4(\varepsilon/\hbar)^2}d\varepsilon\right], \quad (2.1)$$

where e is the charge of an electron, $\hbar=h/2\pi$ is the reduced Planck's constant, $f_d(\varepsilon)=(e^{(\varepsilon-\mu)/k_BT}+1)^{-1}$ is the Fermi-Dirac distribution, and k_B is the Boltzmann constant. The first term in Eq. (2.1) is due to intraband contributions and the second term is due to interband contributions.

For an isolated graphene sheet, the chemical potential, μ, is determined by the carrier density n_s,

$$n_s=\frac{2}{\pi\hbar^2 v_F^2}\int_0^\infty \varepsilon[f_d(\varepsilon)-f_d(\varepsilon+2\mu)]d\varepsilon\,, \quad (2.2)$$

where v_F is the Fermi velocity. Typical doping intensity of the heavy doped layer in epitaxial graphene is about 10^{13} cm^{-2} and the undoped layer (lightly doped layer) is about 10^{10} cm^{-2} which corresponds to the Fermi level at about 350 meV and 12 meV above the Dirac point, respectively. The carrier density can be controlled by an application of a gated voltage and/or chemical doping.

In the limit of the high carrier concentration, $kv_0 \ll (T, E_F)$, the dynamic conductivity of graphene is given in summation form in ref.[6]. It consists of interband and intraband contributions, respectively:

$$\sigma_{\alpha\beta}^{\text{intra}}(\omega) = \frac{-ie^2}{\hbar^2(\omega+i0)S}\sum_{\vec{k}l}\frac{\partial E_{\vec{k}l}}{\partial k_\alpha}\frac{\partial f(E_{\vec{k}l})}{\partial E_{\vec{k}l}}\frac{\partial E_{\vec{k}l}}{\partial k_\beta}$$
$$\sigma_{\alpha\beta}^{\text{inter}}(\omega) = \frac{ie^2\hbar}{S}\sum_{\vec{k},l\neq l'}\frac{f(E_{\vec{k}l'})-f(E_{\vec{k}l})}{E_{\vec{k}l'}-E_{\vec{k}l}-\hbar(\omega+i0)}\times\frac{1}{E_{\vec{k}l'}-E_{\vec{k}l}} < \vec{k}l\,|\,\hat{v}_\alpha\,|\,\vec{k}l' >< \vec{k}l'\,|\,\hat{v}_\beta\,|\,\vec{k}l > , \quad (2.3)$$

Next, the summation notations of the inter- and intra-band conductivity are simplified to to analytic formulae or integral forms that can be easily simulated.

2.1.1 Intraband Complex Dynamic Conductivity

The intraband part of the complex dynamic conductivity is:

$$\sigma_{\alpha\beta}^{\text{intra}}(\omega) = \frac{-ie^2}{\hbar^2(\omega+i0)S}\sum_{\vec{k}l}\frac{\partial E_{\vec{k}l}}{\partial k_\alpha}\frac{\partial f(E_{\vec{k}l})}{\partial E_{\vec{k}l}}\frac{\partial E_{\vec{k}l}}{\partial k_\beta}, \quad (2.4)$$

where,

$$E_{\vec{k}l} = (-1)^l \hbar V k , \quad (2.5)$$

$\vec{k} = (k_x, k_y), k = \sqrt{k_x^2 + k_y^2}$, $\alpha, \beta = x, y$, V is the Fermi velocity, l = 1 for a hole and l = 2 for an electron, $f(E_{\vec{k}l})$ is the Fermi distribution function. Plugging these into equations (2.4) and (2.5), and approximating the summation $\sum_k$ by integration: $\sum_k = \frac{S}{(2\pi)^2}\int_0^{\pi/2} d\theta \int_0^{\infty} dk$, when μ≠0:

$$\sigma_{\alpha\beta}^{intra}(\omega) = \frac{e^2 g_s g_v}{16\hbar}\frac{4i\mu}{\pi\hbar^2(\omega+i0)}\{2\frac{k_B T_e}{\mu}\log[1+\exp\frac{\mu}{k_B T_e}]-1\} . \quad (2.6)$$

Here μ is the Fermi level. The factors g_s and g_v are due to spin and valley degeneracy, respectively, and are both 2. While μ->0,

$$\sigma_{\alpha\beta}^{\text{intra}}(\omega) = \frac{ie^2 g_s g_v}{16\hbar}\frac{8k_B T_e}{\hbar(\omega+i0)\pi}\ln 2 , \quad (2.7)$$

This coincides with the formula given in reference [6],

Another simple case is when T_e->0,

$$\sigma_{\alpha\beta}^{intra}(\omega)=\frac{e^2 g_s g_v}{16\hbar}\frac{4i\mu}{\pi\hbar(\omega+i0)}, \tag{2.8}$$

2.1.2 Interband Complex Dynamic Conductivity

The summation form of the interband contribution is also given in [6]:

$$\sigma_{\alpha\beta}^{inter}(\omega)=\frac{ie^2\hbar}{S}\sum_{\vec{k},l\neq l'}\frac{f(E_{\vec{k}l'})-f(E_{\vec{k}l})}{E_{\vec{k}l'}-E_{\vec{k}l}-\hbar(\omega+i0)}\times\frac{1}{E_{\vec{k}l'}-E_{\vec{k}l}}<\vec{k}l\,|\,\hat{v}_\alpha\,|\,\vec{k}l'><\vec{k}l'\,|\,\hat{v}_\beta\,|\,\vec{k}l>, \tag{2.9}$$

$\hat{v}_\alpha = V\sigma_\alpha$ is the velocity operator, where σ_α is the Pauli matrix. The wavefunctions follow the following forms as described in the previous chapter and in reference [11]:

$$\begin{aligned}\left|\vec{k}1\right\rangle&=\frac{1}{\sqrt{2}}\begin{pmatrix}e^{-i\theta_k/2}\\-e^{i\theta_k/2}\end{pmatrix}\\\left|\vec{k}2\right\rangle&=\frac{1}{\sqrt{2}}\begin{pmatrix}e^{-i\theta_k/2}\\e^{i\theta_k/2}\end{pmatrix}\end{aligned}, \tag{2.10}$$

$$\theta_k=\arctan(k_x/k_y), \tag{2.11}$$

Plugging this into (2.9) and approximating the summation by an integration, when the Fermi level is not 0, we get:

$$Real(\sigma_{inter})=\frac{e^2 g_s g_v}{16\hbar}\left[\frac{1}{1+\exp-\frac{\hbar\omega/2+\mu}{k_B T_e}}-\frac{1}{1+\exp\frac{\hbar\omega/2-\mu}{k_B T_e}}\right], \tag{2.12}$$

$$\begin{aligned}Im(\sigma_{inter})&=\frac{e^2 g_s g_v}{16\hbar}(-\frac{1}{\pi})*\\&[PI\int_0^\infty(\frac{\exp\frac{E-\mu}{k_BT_e}}{(1+\exp\frac{E-\mu}{k_BT_e})^2}+\frac{\exp-\frac{E+\mu}{k_BT_e}}{(1+\exp-\frac{E+\mu}{k_BT_e})^2})\frac{1}{k_BT_e}\log\frac{2E+\hbar(\omega+i0)}{2E-\hbar(\omega+i0)}dE\}]\end{aligned}, \tag{2.13}$$

When μ->0, the real part can be expressed in an analytic form:

$$Real(\sigma_{inter}) = \frac{e^2 g_s g_v}{16\hbar}\left[\frac{1}{1+\exp-\frac{\hbar\omega/2}{k_B T_e}} - \frac{1}{1+\exp\frac{\hbar\omega/2}{k_B T_e}}\right], \tag{2.14}$$

$$\mathrm{Im}(\sigma_{inter}) = \frac{e^2 g_s g_v}{16\hbar}\left(-\frac{1}{\pi}\right) * \left[P.I.\int_0^{\infty}\left(\frac{\exp-\frac{E}{k_B T_e}}{(1+\exp-\frac{E}{k_B T_e})^2} + \frac{\exp\frac{E}{k_B T_e}}{(1+\exp\frac{E}{k_B T_e})^2}\right)\frac{1}{k_B T_e}\log\frac{2E+\hbar(\omega+i0)}{2E-\hbar(\omega+i0)}dE\right], \tag{2.15}$$

When T_e->0, equation (2.13) can be simplified to be:

$$\sigma_{inter} = \frac{e^2 g_s g_v}{16\hbar}\theta(|\Omega|-2) + i\frac{e^2 g_s g_v}{16\hbar}\left(-\frac{1}{\pi}\right)\log\left|\frac{\Omega+2}{\Omega-2}\right|), \tag{2.16}$$

where $\Omega = \frac{\hbar\omega}{\mu}$. Equation (2.16) coincides with the result given in reference [6] for this special case.

2.1.3 Low Frequency Limit of Dynamic Conductivity

The results in the previous section apply in the high frequency limit which only includes the infrared experiments in this dissertation. The dynamic conductivity of graphene in the low frequency limit is needed to understand the low energy photon probe experiment, specifically the THz probe experiment. In this situation, the intraband part of the dynamic conductivity starts to contribute significantly to the signal compared to the high frequency limit since phonons, defects and other scattering mechanisms can provide enough momentum to assist this transition at low transition energy. The specific form of the dynamic conductivity in this limit is beyond the scope of this dissertation and will not be discussed [3].

2.2 Transfer Matrix of Ultrathin Layer with Dynamic Conductivity σ

A transfer matrix defines the relationship between the dynamic conductivity and the optical absorption and reflection properties of the material in question. It builds upon the fact that, according to Maxwell's equations, there are simple continuity conditions for the electric field across boundaries from one medium to the next. If the field is known at the beginning of a layer, the field at the end of the layer can be derived from a simple matrix operation. In this section, we start from the Maxwell's equations and boundary conditions and derive the transfer matrix of an ultrathin layer with dynamic conductivity σ. Since graphene is a fundamentally two-dimensional material with only one atomic layer, an ultrathin conducting layer is a perfect model for a graphene sheet in all the cases considered in this dissertation.

2.2.1 Transfer Matrix of Normal Incidence

I consider the simple case with normal incidence first, assuming E_i^+, E_i^- are the incident and reflected fields, respectively, and E_j^+, E_j^- are the transmitted and reflected fields in the forward and backward directions. H_i^+, H_i^-, H_j^+, H_j^- are the corresponding magnetic fields defined similarly. Consider the following boundary conditions:

Transverse E continuity:

$$E_i^+ + E_i^- = E_j^+ + E_j^- \quad , \tag{2.17}$$

Transverse H field boundary condition:

$$H_i + H_j = \sigma(E_i^+ + E_i^-) \, , \tag{2.18}$$

Now, given the dependence of H on E it follows that

$$\begin{aligned} H_i &= (E_i^+ - E_i^-)/\eta_i \\ H_j &= (E_j^+ - E_j^-)/\eta_j \end{aligned} \, , \tag{2.19}$$

where $\eta_i = \sqrt{\dfrac{\mu_i}{\varepsilon_i}}$ is the dielectric impedance. These results can be written succinctly in the form of a transfer matrix as

$$\begin{bmatrix} E_i^+ \\ E_i^- \end{bmatrix} = \begin{bmatrix} \frac{1}{2}+\frac{\eta_i}{2\eta_j}+\frac{\eta_i\sigma}{2} & \frac{1}{2}-\frac{\eta_i}{2\eta_j}+\frac{\eta_i\sigma}{2} \\ \frac{1}{2}-\frac{\eta_i}{2\eta_j}-\frac{\eta_i\sigma}{2} & \frac{1}{2}+\frac{\eta_i}{2\eta_j}-\frac{\eta_i\sigma}{2} \end{bmatrix} \begin{bmatrix} E_j^+ \\ E_j^- \end{bmatrix}, \tag{2.20}$$

This result, derived from simple boundary conditions, coincides with that derived from the Dyadic Green function method in Ref [5].

2.2.2 Transfer Matrix with Oblique Incidence Angle

Now let's consider the case where the incident field has angle θ with respect to normal incidence. Just as before, we assume E_i^+, E_i^- are the incident and reflected fields, respectively, and E_j^+, E_j^- are the transmitted and reflected fields in the forward and backward directions. H_i^+, H_i^-, H_j^+, H_j^- are the magnetic fields defined in the same manner as the electric fields. From the boundary condition requiring continuity of the transverse E field we get

$$E_i^+ + E_i^- = E_j^+ + E_j^- \quad , \tag{2.21}$$

Similarly, the transverse H field boundary condition gives:

$$(H_i^+ + H_i^-)\sin\theta_i - (H_j^+ + H_j^-)\sin\theta_j = 0, \tag{2.22}$$

and the normal H field boundary condition gives:

$$(H_i^+ - H_i^-)\cos\theta_i - (H_j^+ - H_j^-)\cos\theta_j = \sigma(E_i^+ + E_i^- + E_j^+ + E_j^-), \tag{2.23}$$

As before the relationship between the H fields and E fields is needed:

$$H_{i,j}^{\pm} = E_{i,j}^{\pm} / \eta_{i,j}, \tag{2.24}$$

where, again, $\eta_{i,j} = \sqrt{\dfrac{\mu_i}{\varepsilon_i}}$ is the dielectric impedance.

Solving equations (2.21-2.24), I find the transfer matrix to be:

$$\begin{bmatrix} E_i^+ \\ E_i^- \end{bmatrix} = \begin{bmatrix} \frac{1}{2} - \frac{1}{2}\frac{\sigma\eta_i}{\cos\theta_i} - \frac{1}{2}\frac{\eta_i\cos\theta_j}{\eta_j\cos\theta_i} & \frac{1}{2} - \frac{1}{2}\frac{\sigma\eta_i}{\cos\theta_i} + \frac{1}{2}\frac{\eta_i\cos\theta_j}{\eta_j\cos\theta_i} \\ \frac{1}{2} + \frac{1}{2}\frac{\sigma\eta_i}{\cos\theta_i} + \frac{1}{2}\frac{\eta_i\cos\theta_j}{\eta_j\cos\theta_i} & \frac{1}{2} + \frac{1}{2}\frac{\sigma\eta_i}{\cos\theta_i} - \frac{1}{2}\frac{\eta_i\cos\theta_j}{\eta_j\cos\theta_i} \end{bmatrix} \begin{bmatrix} E_j^+ \\ E_j^- \end{bmatrix}, \tag{2.25}$$

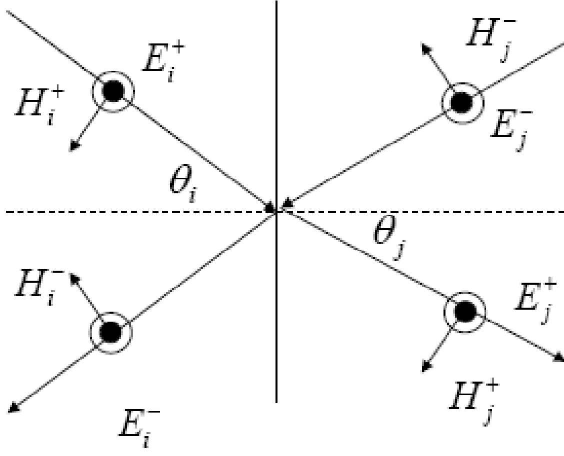

Figure 2.1: Schematic Diagram for an Oblique Angle of Incidence.

The relationship between θ_i and θ_j is determined from Equations (2.22) and (2.21) to be:

$$\eta_i \sin\theta_i = \eta_j \sin\theta_j , \tag{2.26}$$

which is simply Snell's law. It's fairly straightforward to verify that equation (2.25) is compatible with equation (2.20) when $\theta_i = 0$.

2.3 Transfer Matrix Method

The beauty of the transfer matrix method is that a stack of layers can be represented as a system matrix and this matrix is simply the product of the individual layer matrices. To see this assume N stacked graphene layers on a SiC substrate with one doped layer on the bottom and N-1 undoped layers on top. Denote the transfer matrix of the *i*th layer as M_i. Also note that since the distance between two layers is ~3 Å, which is << λ, the identity matrix is a

good approximation for each propagation matrix. After all this the transfer matrix of the whole epitaxial graphene sample M is simply:

$$M = \prod_i^N M_i = \begin{bmatrix} A & B \\ C & D \end{bmatrix}, \tag{2.27}$$

$$\begin{bmatrix} E_i^+ \\ E_i^- \end{bmatrix} = \begin{bmatrix} A & B \\ C & D \end{bmatrix} \begin{bmatrix} E_j^+ \\ E_j^- \end{bmatrix}, \tag{2.28}$$

The system matrix simplifies further since there is no backwards propagating transmitted electric field, so $E_j^- = 0$.

We can derive the transmission coefficient T and reflection coefficient R from the system transfer matrix to be:

$$T = |t|^2 = \left| \frac{E_j^+}{E_i^+} \right|^2 = \left| \frac{1}{A} \right|^2, \tag{2.29}$$

$$R = |r|^2 = \left| \frac{E_i^-}{E_i^+} \right|^2 = \left| \frac{C}{A} \right|^2, \tag{2.30}$$

The absorption coefficient is simply A=1-R-T if scattering from the surface can be neglected. Thus we can get the transmission, reflection and absorption coefficients directly from the transfer matrix calculation.

References

[1] L. A. Falkovsky, and S. S. Pershoguba, Physical Review B **76**, 153410 (2007).

[2] V. P. Gusynin, and S. G. Sharapov, Physical Review B **73**, 245411 (2006).

[3] V. P. Gusynin, S. G. Sharapov, and J. P. Carbotte, Physical Review Letters **96**, 256802 (2006).

[4] V. P. Gusynin, S. G. Sharapov, and J. P. Carbotte, Journal of Physics: Condensed Matter, 026222 (2007).

[5] G. W. Hanson, Journal of Applied Physics **103**, 064302 (2008).

[6] S. A. Mikhailov, and K. Ziegler, Physical Review Letters **99**, 016803 (2007).

[7] N. M. R. Peres, F. Guinea, and A. H. C. Neto, Physical Review B **73**, 125411 (2006).

[8] N. M. R. Peres, A. H. C. Neto, and F. Guinea, Physical Review B **73**, 195411 (2006).

[9] K. Ziegler, Physical Review B **75**, 233407 (2007).

[10] T. Ando, Y. Zheng, and H. Suzuura, Journal of the Physical Society of Japan **71**, 1318 (2002).

[11] A. H. C. Neto *et al.*, Reviews of Modern Physics **81**, 109 (2009).

Chapter III

Time-Resolved Differential Transmission Spectroscopy

3.1 Differential Transmission Spectroscopy

Ultrafast optical spectroscopy provides insights into carrier dynamics with femtosecond temporal resolution. In order to understand the ultrafast dynamics in epitaxial graphene, time-resolved differential transmission (DT) spectroscopy is used in this dissertation. The DT measurement is a pump-probe technique. Pump pulse comes in to excite the carriers from their equilibrium distribution; the excitation is probed by a relatively weaker pulse with a variable time delay. The time delay is typically achieved by mechanically changing the optical path. The resolution is limited by the duration of the pulses instead of the time delay stage which is tens of femtosecond in this dissertation. The delay time measurement window ranges from picosecond to nanosecond depending on the travel range of the mechanical stage.

DT spectroscopy measures the induced transmission change by the pump pulse. The DT signal normalized by the transmission T can be expressed as:

$$\begin{aligned}\frac{DT}{T} &= \frac{T_p - T_0}{T_0} \\ &= \exp\{\alpha_0 l \cdot [1-(f_{e,p}+f_{h,p})-1+(f_{e,0}+f_{h,0})]\}-1 \\ &\approx \alpha_0 l \cdot [(f_{e,p}+f_{h,p})-(f_{e,0}+f_{h,0})]\end{aligned} \tag{3.1}$$

where α_0 is the absorption coefficient and proportional to the product of the interband transition probability and the joint density of states of the conduction and valence bands. The subscripts p and 0 denote quantities with and without pump pulse respectively. Since typical DT/T results are on the order of 10^{-4}, the approximation in the last step of equation (3.1) is valid. DT/T is a direct measurement of the population change in the conduction and valence bands.

3.2 Laser Systems

The central tools for a time-resolved pump-probe experiment are the sources of ultrafast laser pulses. Pulse durations on the order of 100fs contribute temporal resolution in time-resolved experiments. Moreover, the corresponding high peak power allows for the great tunability from visible to the mid-infrared spectrum through nonlinear processes. In our measurement of carrier dynamics in graphene, near IR to mid-IR pulses are needed to probe the carriers around the Fermi levels of different doped layers of epitaxial graphene. Ultrafast laser pulses of such varied wavelengths can be obtained through one master source: a Ti: Sapphire regenerative amplified system. Supercontinuum generation is used to produce a broadband source and optical parametric processes are implemented to achieve wavelength conversion.

3.2.1 Ti: Sapphire Oscillator

The schematic diagram of our oscillator is shown in Fig. 3.1. There is an independent pumping mechanism of a 5W continuous-wave, frequency-doubled Nd: YVO_4 laser at 532nm. The oscillator produces 60fs, 5nJ pulses at a repetition rate of 76 MHz and average power of 400mW at 800nm center wavelength. The cavity is a standard astigmatically-compensated Z-cavity. Although the center wavelength of the output laser

beam can be tuned by tilting the birefringent filter at the end of the cavity, it is usually set at 800 nm with a typical spectral bandwidth larger than 25 nm. The gain spectrum of the Ti: Sapphire crystal ranges from 770 nm to 875 nm, however the tuning range of our oscillator is limited by the bandwidth of the mirrors rather than the gain spectrum of the Ti: Sapphire crystal. Anti-parallel equilateral DF-10 prisms are used to compensate the accumulating intra-cavity dispersion. The laser is mode-locked due to the Kerr-lens mode-locking which is induced by a combination of the third-order process of self-focusing and spatial beam-loss modulation by the hard aperture of the end slit.

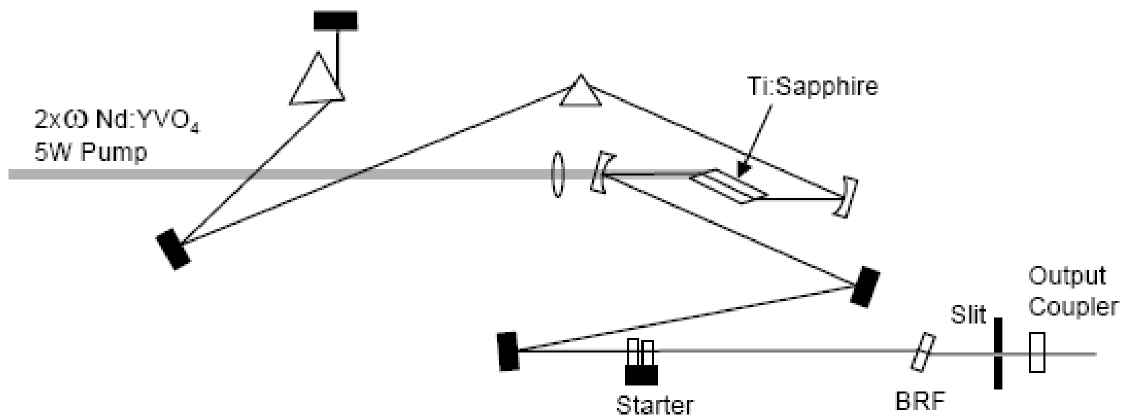

Figure 3.1: Ti: Sapphire Oscillator. Figure taken from ref. [1].

3.2.2 Ti: Sapphire Regenative Amplifier

The nJ pulse from the oscillator is amplified in the regenerative amplifier system using chirped pulse amplification (CPA) to get enough power to pump the IR-OPA after it [2]. The ultrashort pulse from the oscillator is first stretched, using a multi-pass holographic grating pair, by a factor of 500 to 10,000 in the time domain before the amplification so that the peak intensities is low enough to be safely amplified to high energy levels without any nonlinearities and material breakdown. The stretched nanosecond pulse is injected into the amplifier cavity; it is then amplified and ejected out of the cavity. It is

compressed to its original pulse width using another grating pair with dispersion opposite to that of the stretcher. The schematic diagram of a regenerative amplifier system is shown in Fig. 3.2 [3]. The amplifier has the same standard Z-cavity design as the oscillator. Q-switching in the system sets the target repetition rate at 250 kHz, which is limited by the Ti: Sapphire ~3 μs lifetime. While the Q-switch is closed the system cannot achieve lasing because of the low Q of the cavity and a population inversion develops in the Ti:Sapphire crystal. When the Q-switch is open, a stretched pulse from the oscillator is injected by a short RF-driven pulse through the acousto-optic Bragg cell cavity dumper. While the pulses are circulating in the cavity they are amplified by a factor of a few hundred until they saturate the available Ti: Sapphire gain. The repetition rate can be lowered to 100 kHz to achieve higher energy per pulse. Injected pulses typically make twenty five to twenty-eight round trips. After saturating the gain, the stretched pulse is ejected out of the cavity by the same Bragg cell in the cavity dumper. After passing through the Faraday isolator which isolates the back-reflection light from the oscillator, the ejected pulse is recompressed to 80 fs 5 μJ pulses at 250 kHz.

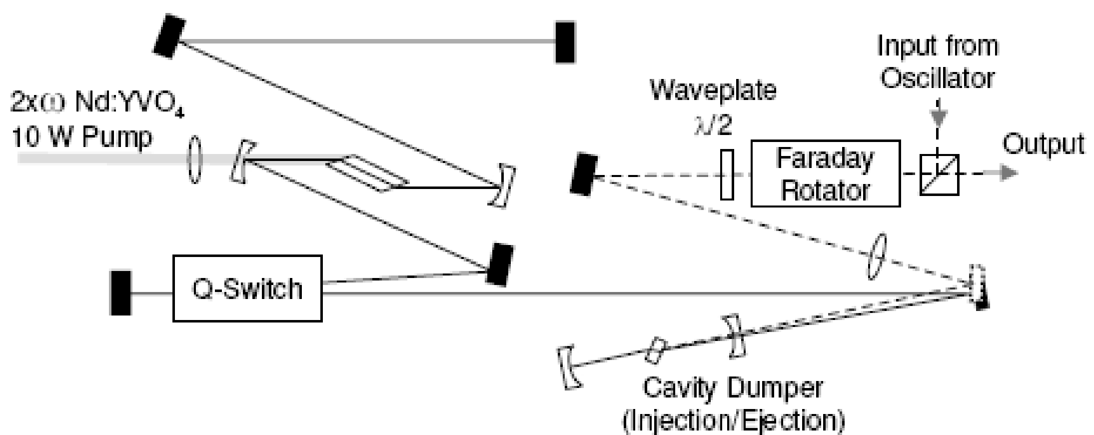

Figure 3.2: Ti: Sapphire Regenerative Amplifier. Figure taken from ref. [1].

3.2.3 White Light Super-Continuum Generation

Ultrashort optical pulses can be used to generate a white light super-continuum to extend the spectral tunability. White light super-continuum is used in our OPA system as a seed pulse for the nonlinear parametric amplification of infrared pulses. White light generation has previously been observed with a 530 nm picosecond pulse in glass [4]. In general, it is possible to generate optical pulses with a very broad spectral range by the interaction of materials with intense ultrashort light pulses. So far it has been observed in many different material systems: glass [4], solids [5], liquid [6], and gases [7].

Self-phase modulation with self-steepening is considered as the main physical mechanism behind the white light generation process [8-10]. The generated spectrum has an asymmetric profile with a cut-off on the short-wavelength side and a decaying tail towards the longer wavelengths. A Ti:Sapphire laser can generate a supercontinuum ranging from 400 nm to 1500 nm. We generated white light super-continuum in a 2 mm thick sapphire disk with a 5 cm plano-convex lens. It is crucial to obtain a stable white light continuum with minimal intensity fluctuations. The generated white light usually shows a round-shape filament with center-positioned bright white light and can be seen by projecting the supercontinuum onto a white card. The generated continuum is collimated with an achromatic doublet lens at a point where the nonlinear effects and the diffracted beam are balanced. A stable white light continuum is obtained when the input pulse power is increased until a red ring pattern appears around the uniform white light disk. If the input power is over this threshold, an iris before the lens is needed to control the beam size otherwise the nonlinear process generates multiple white light filaments and it reduces the stability of the generated supercontinuum.

3.2.4 Optical Parametric Amplifier

The 80 fs, 5μJ pulse produced by the Ti: Sapphire regenerative amplified system is used to pump an infrared optical parametric amplifier (OPA) to generate wavelengths between 1.1 μm -2.5 μm. The schematic of the OPA is shown in Fig. 3.3; 80 fs 800 nm pulse from the RegA are splitted into two arms: one arm (25%) is used to generate the white light supercontinuum as described above and is reflected with protected silver mirrors before focusing onto a Beta-Barium Borate (BBO) crystal, while the other arm (75%) the polarization is rotated by 90° to provide the pump for the amplification process. The pump is put on a translation stage to compensate the group velocity mismatch and the walk-off between the white light seed and 800 nm pulse. The two pulses are recombined through a dichroic mirror and focused onto the type-II BBO crystal cut at μ =32° [11]. The nonlinear parametric amplification process is achieved through the 2nd order nonlinearity of the BBO crystal. In this double pass configuration, the first pass weakly saturates the amplifier's gain while the second pass extracts ~10% of the pump energy. In order to match the peak gain between the first and second pass, each pass is kept in the same horizontal plane.

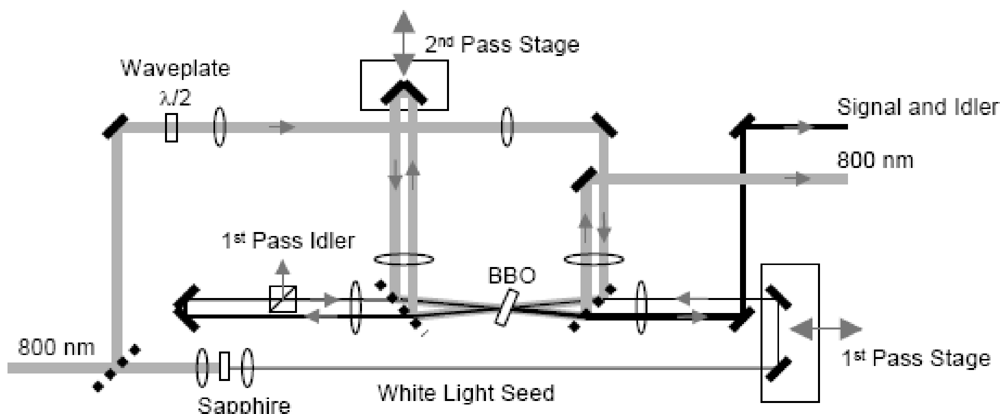

Figure 3.3: OPA Schematic: 800 nm denoted by thick gray line; the seed and amplified beam by black line. Figure taken from ref. [1].

3.2.4.1 Parametric Amplification

Here we briefly describe the principle of parametric amplification following the description by Wu [1]. We assume that the material's response is instantaneous. The nonlinear response is often described by the induced polarization P(t) as a power series of the oscillating electric field E(t):

$$\vec{P} = \varepsilon_0[\overleftrightarrow{\chi}^{(1)}\vec{E}(t) + \overleftrightarrow{\chi}^{(2)}\vec{E}(t)\vec{E}(t) + \overleftrightarrow{\chi}^{(3)}\vec{E}(t)\vec{E}(t)\vec{E}(t) + ...] \tag{3.4}$$

where $\chi^{(i)}$'s are the ith order susceptibilities in tensor form. Consider two monochromatic plane waves in the material:

$$\vec{P}^{(2),(\omega_i+\omega_j)}(z,t) = D \cdot \varepsilon_0 \overleftrightarrow{\chi}^{(2)} E_i E_j e^{-i[(k_i+k_j)z-(\omega_i+\omega_j)t]} + c.c. \tag{3.5}$$

where ω extends over all positive and negative frequencies and D is the degeneracy factor, D=1/4 if $\omega_i=\omega_j$ or 1/2 if $\omega_i \neq \omega_j$. The time-varying polarization field can act as the source term for new components of the electromagnetic field. For a new frequency component $\vec{E}_3$ at $\omega_3=\omega_1+\omega_2$, the wave equation can be written as

$$\nabla^2 \overline{E}_3 - \frac{1}{c^2}(1+\chi^{(1)})\frac{\partial^2}{\partial t^2}\vec{E}_3 = -\mu_0 \frac{\partial^2}{\partial t^2} P^{(2),(\omega_3=\omega_1+\omega_2)} \tag{3.6}$$

With

$$\vec{E}_3 = E_3 e^{-i(k_3 z - \omega_3 t)},$$

$$k_i^2 = \frac{\omega_i^2}{c^2}(1+\chi_i^{(1)}) = \frac{\omega_i^2}{c^2} n_i^2 \tag{3.7}$$

By carrying out the differentiation with the slowly varying envelope approximation and defining the new field variable A_i by

$$A_i = \sqrt{\frac{n_i}{\omega_i}} E_i \tag{3.8}$$

we get:

$$\frac{dA_3}{dz} = -i\kappa \cdot A_1 A_2 \cdot e^{-i\Delta kz} \tag{3.9}$$

$$\frac{dA_1}{dz} = -i\kappa \cdot A_3 A_2^* \cdot e^{i\Delta kz} \tag{3.10}$$

$$\frac{dA_2}{dz} = -i\kappa \cdot A_3 A_1^* \cdot e^{i\Delta kz} \tag{3.11}$$

where

$$\kappa = \frac{1}{c}\sqrt{\frac{\omega_1\omega_2\omega_3}{n_1 n_2 n_3}} \cdot \chi^{(2)} \tag{3.12}$$

$$\Delta k = k_1 + k_2 - k_3 \tag{3.13}$$

The field amplitudes of the three frequencies are coupled via the 2nd order nonlinear process. Optical parametric amplification in our system can be described with the 800nm pump pulse as A_3, the white light seed pulse as A_1 and no input field at ω_2 initially. Fig. 3.6 shows a schematic drawing of the parametric process. The coupled equations can be solved in a simple way in the non-depleted-pump approximation where the energy loss in the pump wave is negligible ($dA_3/dz=0$). With $A_2(0)=0$, we can obtain

$$A_1(z)e^{i\frac{1}{2}\Delta kz} = A_1(0)[\cosh\frac{1}{2}bz + i\frac{\Delta k}{2b}\sinh bz] \tag{3.14}$$

$$A_2(z)e^{-i\frac{1}{2}\Delta kz} = i\frac{g}{2b}A_1(0)\sinh bz \tag{3.15}$$

where

$$g = 2\kappa A_3(0) \tag{3.16}$$

$$b = \sqrt{g^2 - (\Delta k)^2} \tag{3.17}$$

Under phase matching conditions ($\Delta k=0$), the oscillatory behavior disappears and both

waves experience monotonic growth which increases asymptotically as exp(gz) (until the non-depletion assumption breaks down). The "signal" wave at ω_1 is amplified by the nonlinear mixing process and an idler wave at $\omega_2=\omega_3-\omega_1$ is generated by the process. In other words, the 800nm photon is "split" into the signal and idler photons when both energy and momentum (phase matching) conservation are met.

The phase matching is achieved by changing the BBO orientation, i.e. the angle between the propagation direction and the crystal axis. BBO is a negative uniaxial crystal where the light polarized along the optical axis experiences a smaller refractive index n_e than light polarized along some other axis. The type-II phase matching requires

$$k_3 = k_1 + k_2 \tag{3.18}$$

$$n_{e,3}\omega_3 = n_{0,1}\omega_1 + n_{e,2}\omega_2 \tag{3.19}$$

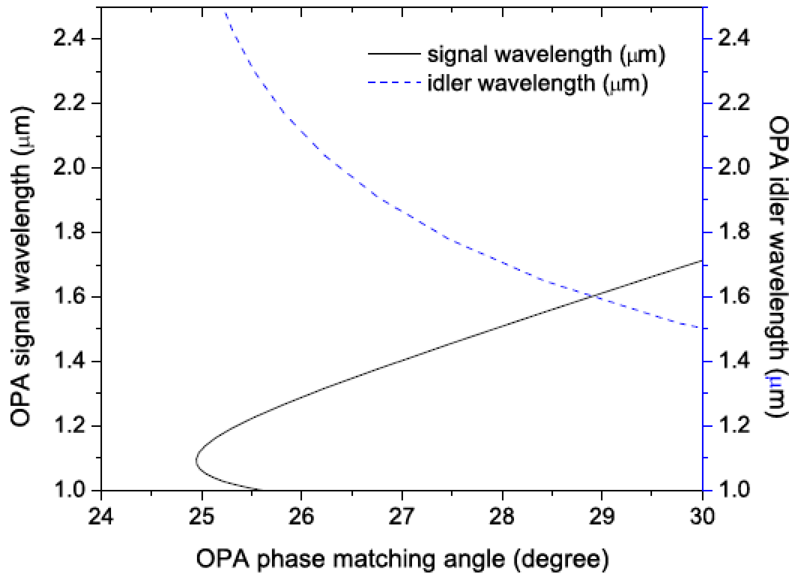

Figure 3.4: OPA Phase Matching Angle. Figure taken from ref.[12].

And the n_e's depend on the angle θ between the optical axis and k

$$\frac{1}{n_{e,i}^2(\theta)} = \frac{\sin^2\theta}{\overset{-2}{n_{e,i}}} + \frac{\cos^2\theta}{\overset{-2}{n_{0,i}}} \tag{3.20}$$

where $\bar{n}_{e,i}$ is the principle value of the extraordinary refractive index. In the OPA setup, the 800nm and the idler wave are polarized in the vertical plane containing the optical axis while the signal is polarized in the horizontal plane. For amplification of different frequency bands in the white light seed, angle θ is adjusted to satisfy the above constraints. Fig 3.5 shows the phase match angle for the type-II BBO crystal calculated from the Sellmeier equation given by Kato [11]:

$$n_0^2 = 2.7359 + \frac{0.01878}{\lambda^2 - 0.01822} - 0.01354\lambda^2 \qquad (3.21)$$

$$n_e^2 = 2.3753 + \frac{0.01244}{\lambda^2 - 0.01667} - 0.01516\lambda^2 \qquad (3.22)$$

where λ is the wavelength in μm.

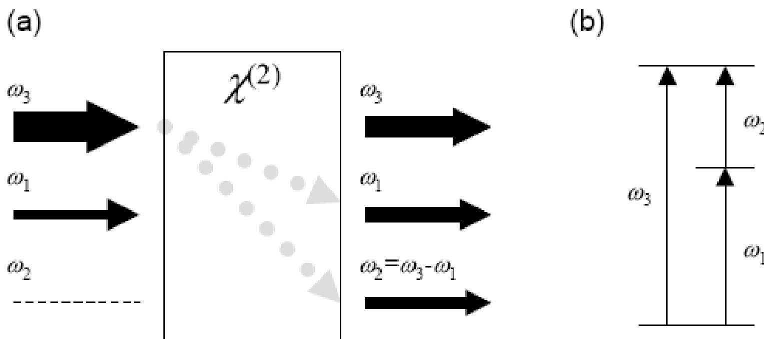

Figure 3.5: Parametric Amplification: (a) typically no input field applied at ω2. Net energy flows from the pump field into the two lower frequency fields. (b) Photon energy. Figure taken from ref.[1].

3.2. Infrared OPA system

The OPA incorporates a double-pass configuration with the layout shown in Fig. 3.3. Two mechanical translation stages are used to compensate for the group delay mismatch and walk-off between the 800nm pump and signal pulse for each pass. After the first amplification the idler pulse is removed using a polarizing beam splitter so that only the signal and OPA pump pulse participate in the second pass. Removing the idler from the

second pass prevents the interferometric nonlinear mixing between the phase-sensitive idler and OPA pump [13]. This significantly reduces the output noise and time-delay/alignment sensitivity, especially for long wavelength operation when the signal and idler pulses have similar wavelength close to the degeneracy at 1.6 μm. The total power generated is around 150mW over most of the tuning range. In daily operation, we see a reduction in power below 1.2μm due to the strong group velocity mismatch while above 1.6μm the power is limited by the decaying energy tail of the white light generation at long wavelength.

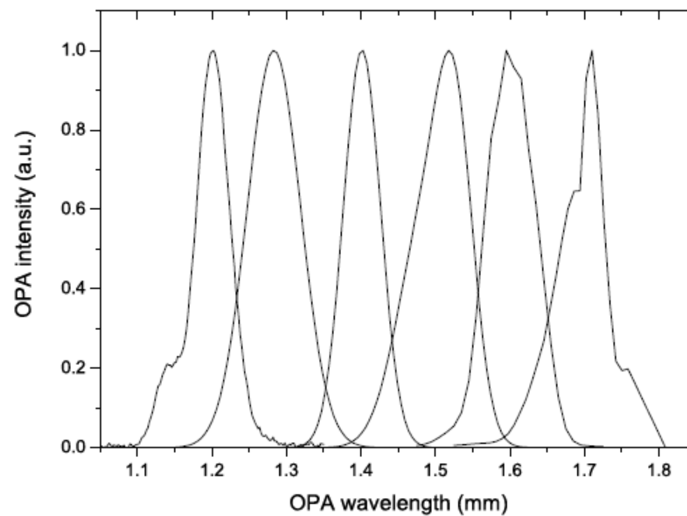

Figure 3.6: OPA Signal Wavelength Characteristics. Figure taken from ref.[12].

3.2.5 Differential Frequency Generator

In the second stage of wavelength conversion, the signal and idler of the OPA are used to pump the difference frequency generator (DFG) shown in Fig. 3.7. The pulses are separated with a dichroic mirror, which reflects the signal and transmits the idler. A delay stage is placed in the idler arm to compensate group delay mismatch and walk-off between the two pulses. The OPA signal and idler pulses are focused onto a type-I $AgGaS_2$ crystal for difference frequency generation [14, 15]. The principle behind the

difference frequency generation is the same as the parametric amplification described in the previous section. The difference is that, for the DFG, the OPA signal pulse is now the higher frequency and is represented as A_3 in Eq. (3.9) to (3.11). A_1 now represents the OPA idler pulse and the generated pulse is at the difference frequency $\omega_2=\omega_3-\omega_1$. The type-I phase matching is given by

$$n_{e,3}\omega_3 = n_{0,1}\omega_1 + n_{0,2}\omega_2 \tag{3.23}$$

The Sellmeier equations are provided by Fan [16]:

$$n_0^2 = 3.3970 + \frac{2.3982}{1-0.09311/\lambda^2} + \frac{2.1640}{1-950.0/\lambda^2} \tag{3.24}$$

$$n_0^2 = 3.5873 + \frac{1.9533}{1-0.11066/\lambda^2} + \frac{2.3391}{1-1030.7/\lambda^2} \tag{3.25}$$

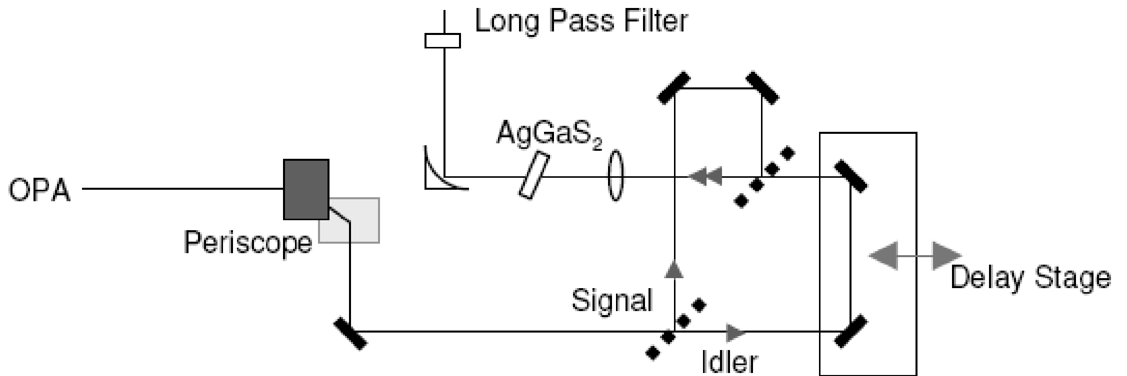

Figure 3.7: DFG Schematics. Figure taken from ref. [12].

where λ is the wavelength in μm. Fig. 3.8 shows the calculated phase matching angle for for the DFG with respect to the OPA signal wavelength. For the measurements reported in this thesis, the DFG is tuned from 2.7 to 7 μm for different excitation. Fig. 3.9 shows a tuning record of the OPA and DFG with respect to the $AgGaS_2$ crystal orientation (inferred by the stage position reading). The mid-IR pulse was re-collimated with a gold-coated 90°-turning off-axis parabola. The pulse width of the mid-IR pulse is measured by

cross correlating with a 100 fs 800 nm gating pulse in a KTA ($KTiOAsO_4$) crystal. As shown in Fig. 3.10, when tuned to 5 μm, the cross correlation has a width of 220 fs. The average DFG power typically falls within 3 to 6mW, decreasing exponentially over 7 μm. A different $AgGaS_2$ crystal is used for wavelengths beyond 5 μm to get power over 2 mW.

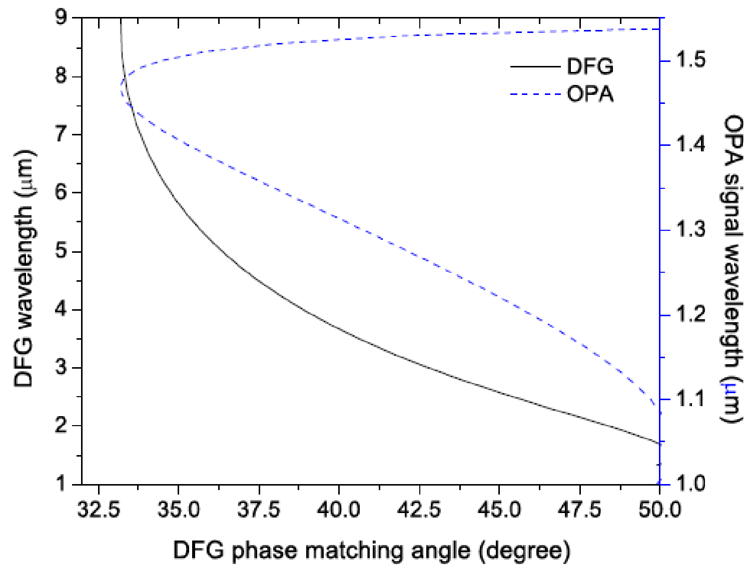

Figure 3.8: DFG Phase Matching Angle. Figure taken from ref. [12].

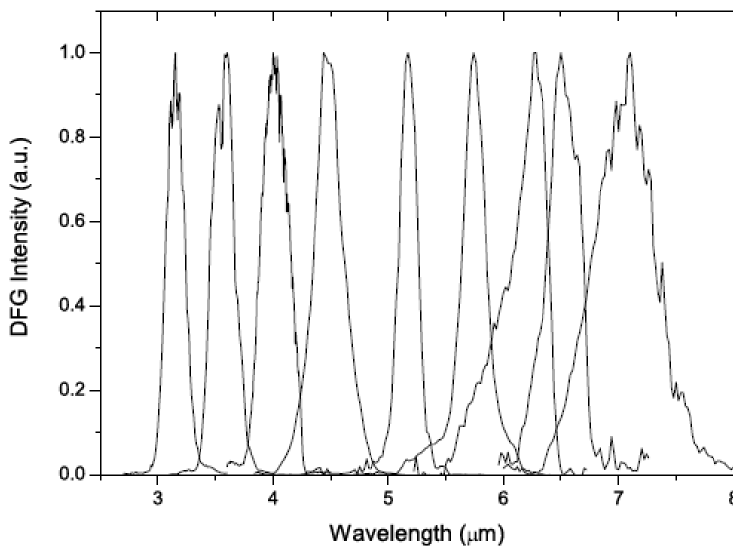

Figure 3.9: DFG Wavelength Characteristics. Figure taken from ref.[12].

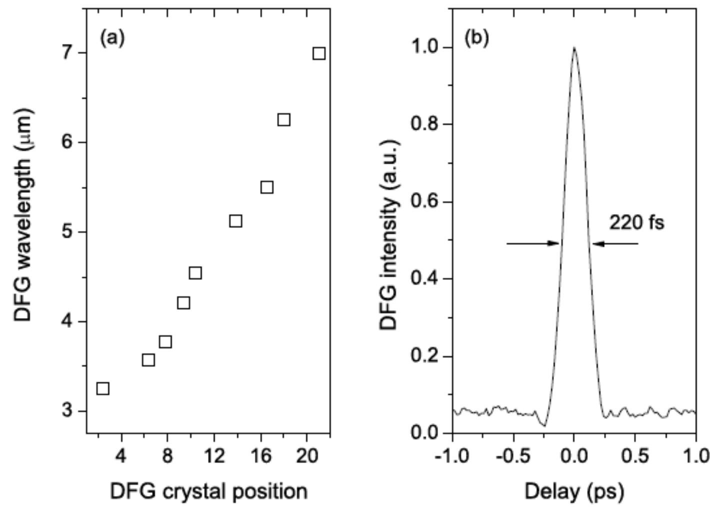

Figure 3.10: DFG Tuning Characteristics. (a) Tuning of DFG wavelength by crystal orientation (inferred by stage position). (b) A typical cross-correlation trace for DFG temporal characteristics. Figure taken from ref. [12].

3.3 Experiment Setup for Ultrafast Pump Probe Spectroscopy

3.3.1Ultrafast Non-degenerate Pump Probe Spectroscopy

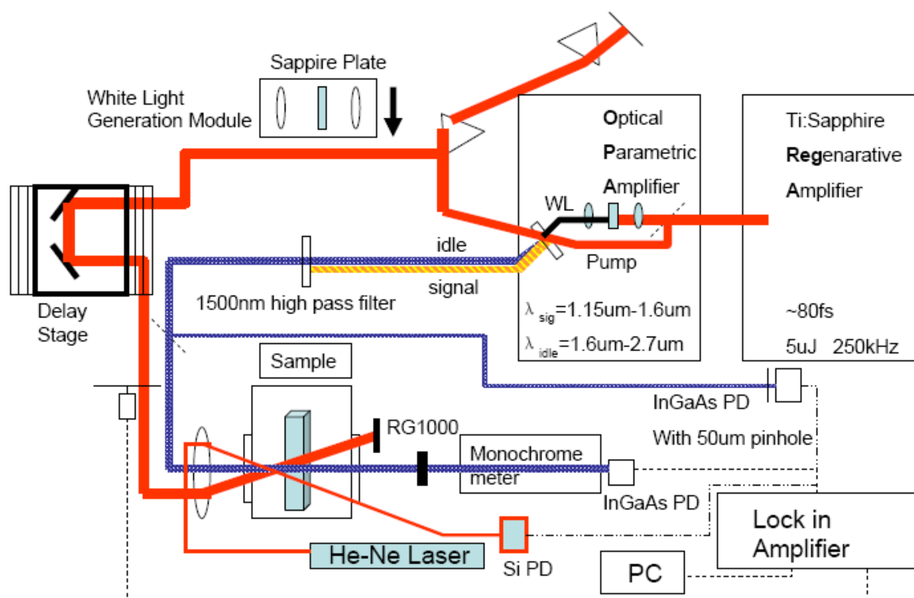

Figure 3.11: Non-degenerate Experiment Setup. Experimental setup for the time-resolved nondegenerate pump probe experiment with 800nm pump and OPA probe.

Femtosecond time-resolved nondegenerate pump-probe DT spectroscopy results in this thesis typically relied on 800 nm pump pulses. Occasionally other wavelengths from

either the white light generation module or the OPA are used as the pump to detect some dynamics. For those experiments a 10 nm bandwidth filter is used to narrow the pump bandwidth. The experiment scheme using the OPA probe is shown in figure 3.11 and is very similar to the one using the DFG. A 100-fs 250-kHz amplified Ti: Sapphire laser centered at 800 nm is used to pump the infrared OPA described above in Sec. 3.2 with signal wavelength tunable from 1.1 to 1.6 μm and idler wavelength tunable from 1.6-2.6 μm. Both the idler and the signal pulses have been used as the probe in some of these experiments with pulse width estimated to be less than 150 fs. For some other experiments, the signal and idler from the OPA are used to pump the DFG to generate 2.6 μm-7 μm probe wavelengths with pulse widths measured to be around 220 fs. The dispersion-compensated residual 800-nm beam after the OPA is used as the pump. The pump and probe beams are usually co-linearly polarized unless specifically noted and focused to about 80-μm and 40-μm diameter spots respectively on the sample. The probe beam after the sample is filtered in a monochrometer with 3-nm resolution and detected by a photo detector and lock-in amplifier referenced to the 4.2-kHz mechanically chopped pump. Depending on the probe wavelength, different photo detectors must be used. An InGaAs detector is used for the OPA probe while nitrogen cooled HgCdTe and InSb detectors are used for the DFG probes. The temperature of the sample is stabilized in a helium-flow cryostat with a feedback-heater controller over a range 10-300K. For some experiments, an additional beam path with a He-Ne laser is used. The beam from the He-Ne laser is focused through a pinhole on the sample holder and detected by a Si detector to register any sample position movement due to temperature change or some other factors during the experiment.

3.3.2Ultrafast Degenerate Pump Probe Spectroscopy

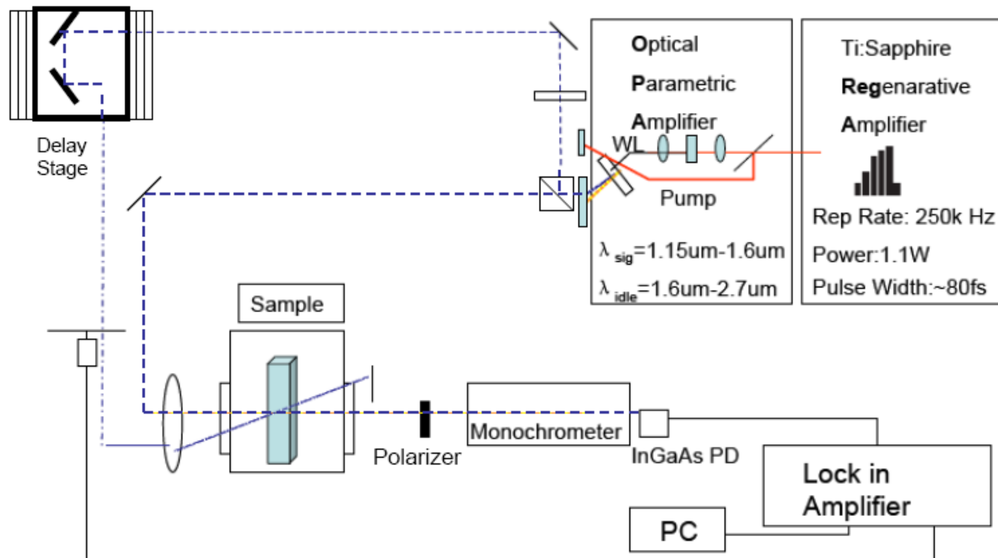

Figure 3.11: Degenerate Experiment Setup. Experimental setup for the time-resolved degenerate pump probe experiment with OPA idler or signal as pump and probe.

The experiment setup for ultrafast degenerate pump probe spectroscopy is identical to the ultrafast non-degenerate pump probe spectroscopy except that the pump and probe wavelengths are the same. The degenerate pump probe setup is shown in figure 5.12, since single chopping is used and the monochrometer can not filter the pump wavelength in this case, the pump beam causes a huge background noise floor in the experiment. Although an aperture is used to block the transmitted pump beam right after the sample, surface roughness causes some of the pump beam to be scattered in the direction of the probe and detector. To reduce this scattered pump noise we cross polarize the pump and probe in our setup. A periscope is used to rotate the probe beam polarization by 90 degrees and a linear polarizer is inserted before the monochrometer to eliminate the scattered pump while letting the probe beam through. In this way, good signal to noise ratios can be obtained. A double chopping scheme is another way to get rid of the pump noise floor. It has been tried in this experiment to significantly reduced the signal level.

References

[1] Z.-K. J. Wu, Ph.D Thesis, University of Michigan (2006).

[2] D. Strickland, and G. Mourou, Optics Communications **55**, 447 (1985).

[3] T. B. Norris, Opt. Lett. **17**, 1009 (1992).

[4] R. R. Alfano, and S. L. Shapiro, Physical Review Letters **24**, 584 (1970).

[5] A. Brodeur, and S. L. Chin, J. Opt. Soc. Am. B **16**, 637 (1999).

[6] W. L. Smith, P. Liu, and N. Bloembergen, Physical Review A **15**, 2396 (1977).

[7] P. B. Corkum, C. Rolland, and T. Srinivasan-Rao, Physical Review Letters **57**, 2268 (1986).

[8] J. K. Ranka, and A. L. Gaeta, Opt. Lett. **23**, 534 (1998).

[9] A. L. Gaeta, Physical Review Letters **84**, 3582 (2000).

[10] J. E. Rothenberg, Opt. Lett. **17**, 1340 (1992).

[11] K. Kato, Quantum Electronics, IEEE Journal of **22**, 1013 (1986).

[12] H. Choi, Ph.D Thesis, University of Michigan (2008).

[13] J. Fraser, and K. Hall, Opt. Express **5**, 21 (1999).

[14] B. Golubovic, and M. K. Reed, Opt. Lett. **23**, 1760 (1998).

[15] M. K. Reed, and M. K. S. Shepard, Quantum Electronics, IEEE Journal of **32**, 1273 (1996).

[16] Y. X. Fan *et al.*, Applied Physics Letters **45**, 313 (1984).

Chapter IV

Ultrafast Spectroscopy on Epitaxial Graphene

The transport of massless Dirac Fermions in graphene is a subject of intense interest at present due to graphene's unusual electronic properties and the potential for carbon-based electronic devices [1-5]. In steady-state transport measurements, the transport is controlled by the electrons near the Fermi level. Transport in high-speed devices, however, is determined by the dynamic conductivity of hot carriers. With the application of high electric fields, carrier gain energy at a rate much faster then that for carriers to lose energy to the lattice, creating a non-equilibrium carrier population which subsequently comes to an internal thermal equilibrium among the carriers themselves through carrier-carrier scattering. These carriers (called hot electrons) have a higher temperature T_e then the lattice temperature T_L, will then relax towards a thermal equilibrium with the lattice by losing energy to the lattice. As transport properties at high fields are determined by these hot carriers, a quantitative understanding of the hot carrier dynamics is a crucial issue affecting the performance characteristics of ultrafast, high-field devices. Also the investigation of hot carrier effects, plays a central role in the science of semiconductors and provides a key link between fundamental physics and high speed devices [6]. In this chapter I describe a series of experiments applying ultrafast pump-probe spectroscopy to investigate the dynamics of hot Dirac Fermions, electron-phonon coupling, carrier-carrier scattering, interlayer thermal

coupling, hot phonon effect, doping profile, screening length and a new electromagnetic mode seen in epitaxial graphene. Most of the experimental results in this chapter have been modeled using the idea of a temperature-dependent dynamic conductivity including both the interband and intraband contributions. At the end I will also describe my effort in probing the new TE mode in graphene using pump probe spectroscopy.

4.1 Ultrafast Relaxation of Hot Dirac Fermions

Our approach to the study of hot Dirac Fermion relaxation is to utilize ultrafast pump probe spectroscopy. The ultrafast pump-probe experiment setup is described in Chapter 3.

4.1.1 Experimental Setup

In most experiments in this section, the dispersion-compensated residual 800-nm beam after the OPA is used as the pump and the 1.1 to 2.6 μm signal and idle from the OPA is used as the probe. The probe pulse width is estimated to be less than 150 fs. The pump and probe beams are colinearly polarized and focused to 80-μm and 40-μm diameter spots on the sample respectively. The temperature of the sample is stabilized in a He flow cryostat with a feedback-heater controller over a range of 10-300K. The sample number used in this experiment is #598 grown by Prof. Walt De Heer's group in Georgia Institute of Technology, which is an ultrathin epitaxial graphene film produced on the C-terminated $(000\bar{1})$ face of single-crystal 4H-SiC by thermal desorption of Si. The details of the growth processes and characterizations of surface quality using low energy electron diffraction (LEED), and scanning tunneling microscopy (STM) have been discussed elsewhere [7]. Fig. 4.1 shows the structure of the sample: the first carbon layer (green) is covalently bonded to the 4H-SiC substrate and acts as a buffer layer; the following layer (red) exhibits the graphene electronic spectrum and is doped by charge transfer from SiC. From the measured Fermi level (see

below), the charge density is estimated to be $9x10^{12}$ electrons/cm^2. The graphene layers (blue) above the doped layer are essentially neutral before we find the exact the doping profile afterwards [8, 9]. For the growth conditions employed, the number of neutral layers has been estimated to be in the range of 15-20. Steady-state transport measurements on similar samples give phase coherence lengths of 1.2 μm at 4 K and 500 nm at 58 K [2] (the doped layer dominates steady-state transport properties in those measurements).

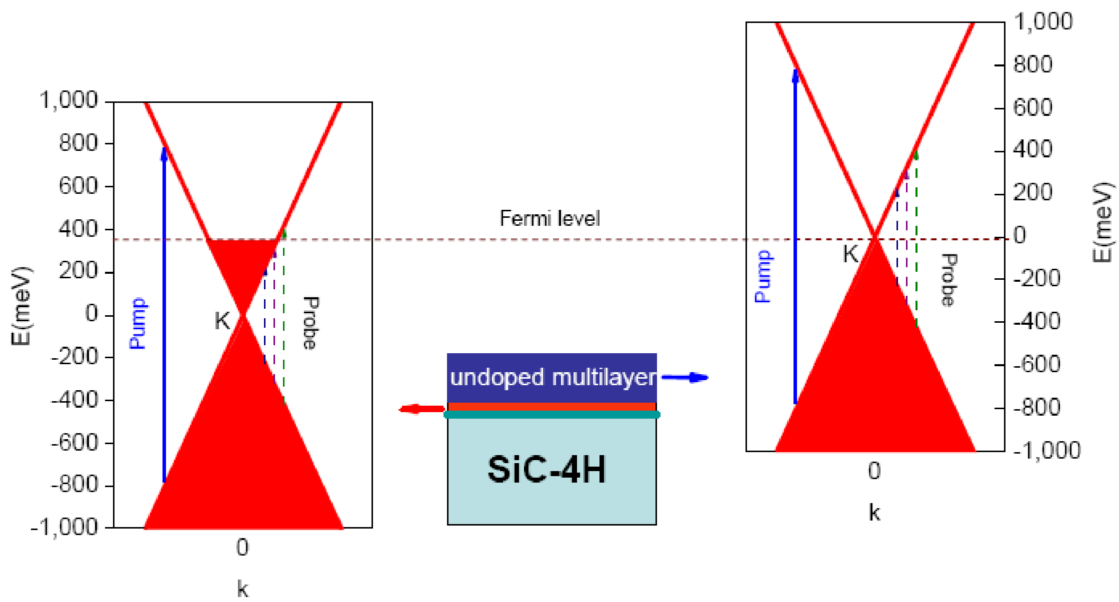

Figure 4.1: Sample Structure and Energy Dispersion Curve. Sample structure and energy dispersion curves of doped and undoped graphene layers. The sample has a buffer layer (green) on the SiC substrate and 1 heavily doped layer (red) followed by 20 undoped layers (blue) on top. The Fermi level is labeled with a dashed line (brown) lying at 348 meV (from the later data) above the Dirac point of the doped graphene layer or passing through the Dirac point of the undoped graphene layers. The blue solid line shows the transitions induced by the 800-nm optical pump pulse; the three dashed lines correspond to probe transitions at different energies with respect to the Fermi level (discussed in the text).

As illustrated in Fig. 4.1, a 100-fs near-infrared (800-nm) optical pulse excites quasiparticles from the valence to the conduction band across the Dirac point; the optical response of a multilayer graphene structure containing both doped and undoped layers is measured via the differential transmission (DT) of a tunable probe pulse as a function of pump-probe delay.

The electrons have an initial energy of 428 meV above the Fermi level in the doped layers and 777 meV in the undoped layers. Due to rapid carrier-carrier scattering, a hot thermal distribution is established within the time resolution of the experiment. The thermal distribution then cools towards the lattice temperature, initially via the emission of high-energy (194 meV and 330 meV) phonons [28] and later via the interaction with acoustic phonons. In these experiments, the elevated temperature of the quasiparticles is manifested primarily through the modification of the probe-beam absorption by Pauli blocking of interband transitions.

4.1.2 Experimental Results

Figure 4.2(a) shows DT spectra for a single position on the epitaxial graphene sample at various probe time delays, for a substrate temperature of 10 K and 500-μW pump power (corresponding to a photon fluence of 1.6 x 10^{14} photons/cm^2 per pulse). The DT amplitude peaks near zero time delay for all probe wavelengths, consistent with the establishment of a hot thermal carrier distribution within the experimental time resolution. The DT amplitude then relaxes toward zero on a time scale of 15 ps. The most notable feature of the DT spectrum is that the DT signal flips from positive on the blue (high-energy) side of a probe wavelength of 1.78 μm to negative on the red (low-energy) side of 1.78 μm, and flips back from negative to positive again at 2.35 μm. Positive DT corresponds to pump-induced transmission of the probe; negative DT corresponds to pump-induced probe absorption. The two zero crossings thus divide the DT spectrum into 3 different regions, which we will consider in more detail below.

Figures 4.2 (b) and (c) show DT time scans for selected probe wavelengths on both red and blue sides of the two zero crossings. Immediately following the pump pulse at time zero, the

DT signal is positive over the entire probe spectral range. The DT signal becomes negative within 2 ps if the probe wavelength falls between 1.78 μm and 2.35 μm, otherwise it remains positive until the signal decays away. The DT signal relaxes to zero on the time scale of 1-10 ps depending on probe wavelength (discussed further below). Experiments at different locations on the sample reveal that the sample is somewhat inhomogeneous, with the upper (1.78μm) zero crossing varying between 1.75 to 1.95 μm and the lower crossing (2.35μm) of 2.2 to 2.45 μm. The lack of the data in the two blank regions of Fig. 2(a) is due to limitations in tuning our OPA.

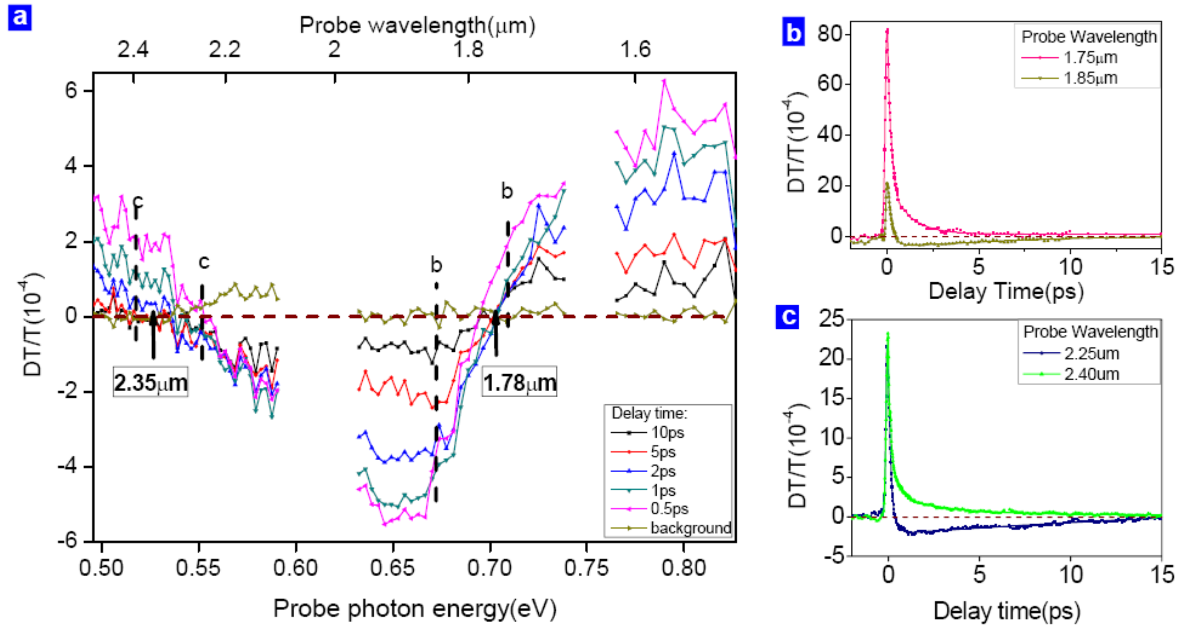

Figure 4.2: DT Spectrum and Zero Crossings. (a) DT spectra on epitaxial graphene at 10 K, with 500 μW at 800-nm pump with less than 100-fs pulse width at probe delays of 10 ps, 5 ps, 2 ps, 1 ps, 0.5 ps and background (50 ps before the pump arrives). The arrows at 1.78 μm and 2.35 μm indicate where the DT signals flip sign. (b) DT time scan of the two probe wavelengths marked in part a at the red (1.85 μm) and blue side (1.75 μm) of the 1.78 μm DT crossing point. (c) Time scan of the two probe wavelengths marked in part a at the red (2.40 μm) and blue side (2.25 μm) of the 2.35 μm DT crossing point. In all figures, the dashed line (brown) marks where the DT signal is zero. The DT tails in b and c are simply fitted by sigmoidal curve.

In order to study the effect of lattice temperature on the carrier dynamics, we show in Fig. 4.3 temperature-dependent DT time scans for selected probe wavelengths in the three different

spectral regions of Fig. 4.2. For spectral regions where the DT sign is positive (above the upper zero crossing, and below the lower zero crossing), the DT dynamics show little temperature dependence (Fig. 4.3 (b), (c)), apart from minor amplitude changes and slightly different relaxation times. When the probe wavelength falls between 1.78 μm and 2.35 μm, the DT signal is positive at early times and becomes negative within a few picoseconds. The amplitude of the negative DT component decreases with increasing temperature and almost disappears for temperatures above 180 K. The delay time at which the DT crosses zero increases monotonically with temperature (Figure 4.3 (a) inset).

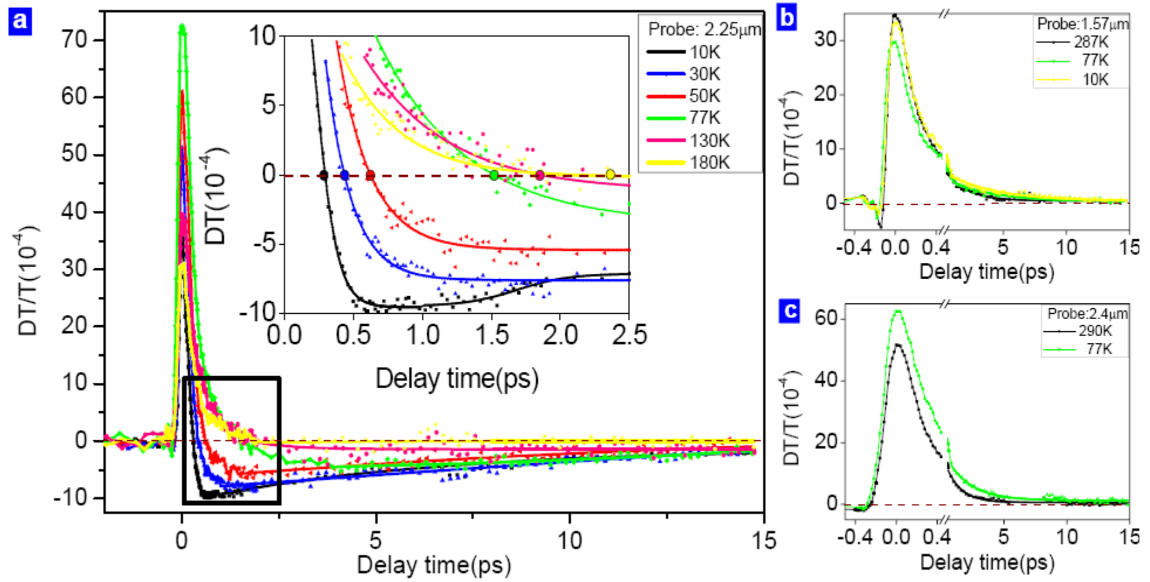

Figure 4.3: Temperature-dependent DT Spectra. (a) DT time scans at temperature 10K, 30K, 50K, 77K, 130K and 180K with 500μW pump at 800nm and 2.25μm probe. The DT time scans were fit with a sigmoidal curve to show the behavior of the zero crossings more clearly. In the inset the DT zero-crossing points at different temperatures are marked with different colors. (b) DT time scans at temperatures of 10K, 77K and 287K with 1mW pump at 800nm and 1.57μm probe. c, DT time scans at temperatures of 77K and 290K with 1mW, 800nm pump and 2.4μm probe. In all figures, the dashed line (brown) marks where DT signals are zero.

4.1.3 Interpretation of the Results

We now turn to the interpretation of the DT data and the origin of the zero-crossings. From the simplest point of view, the differential probe transmission spectrum simply arises from

the change in carrier occupation functions in the bands, since generally the probe absorption is proportional to $f_v(1-f_c)$ where f_v (f_c) is the occupation probability in the valence (conduction) band. Following the excitation of quasiparticles high into the conduction band by the pump pulse, electron-electron scattering on a time scale short compared to 150 fs establishes a hot thermal distribution characterized by an electron temperature T_e. Since the carrier occupation probability above the Fermi energy is increased (relative to the occupation without the pump pulse), the DT signal is positive due to reduced probe absorption. The probe DT is negative below the Fermi level, however, since heating of the electron plasma reduces the occupational probability for low energies. Thus the upper zero crossing at 1.78 μm probe wavelength is interpreted as arising from smearing of the Fermi level in the doped layers, Assuming no bandgap [10] (or any possible bandgap to be less than the probe energy), we find the Fermi level to be 348 meV above the Dirac point for the doped layers. This result is close to the predicted Fermi level in the carbon-deficient geometry from first-principles calculations[11] and is consistent with the results of transport studies on epitaxial graphene grown on the C-terminated ($000\bar{1}$) face [2]. Scanning tunneling spectroscopy [12] and angle-resolved photoemission spectroscopy (ARPES) of epitaxial graphene grown on the Si-terminated (0001) also find similar values for the Fermi level [13, 14]. We note additionally that there is no peak in the DT spectrum near the Fermi level; this indicates that there is no Fermi edge singularity [15] due to electron-hole interactions in the interband absorption spectrum of graphene, as may be expected from the massless nature of the quasiparticles.

At very long probe wavelengths, i.e. for final states well below the Fermi level of the doped layers, one may expect the DT spectra to be determined primarily by the carrier occupations in the undoped layers; since the pump pulse generates hot carriers in the undoped layers, the

sign of the DT signal arising from the undoped layers should be positive for all wavelengths. However, for probe wavelengths below the Fermi level of the doped layer, the contribution of the doped layer to the DT is negative. Thus one expects that for some probe energy the net DT signal should flip sign; this is the origin of the lower zero crossing at 2.35 μm.

A convenient approach to calculate the probe transmission and reflection spectra for a multi-layer structure is the transfer-matrix method described in Chapter II. A transfer matrix relates the total field (incident plus reflected) electric field on one side of a reference plane to the opposite side. For a 2D layer with complex conductivity, the transfer matrix may be written as,

$$\begin{bmatrix} E_i^+ \\ E_i^- \end{bmatrix} = \begin{bmatrix} \frac{\eta_i}{2\eta_j} + \frac{\eta_i \sigma}{2} + \frac{1}{2} & -\frac{\eta_i}{2\eta_j} + \frac{\eta_i \sigma}{2} + \frac{1}{2} \\ \frac{1}{2} - \frac{\eta_i}{2\eta_j} - \frac{\eta_i \sigma}{2} & \frac{1}{2} + \frac{\eta_i}{2\eta_j} - \frac{\eta_i \sigma}{2} \end{bmatrix} \begin{bmatrix} E_j^+ \\ E_j^- \end{bmatrix}, \tag{4.1}$$

where E_i and E_j are electric fields on incident and transmitted sides, respectively, the superscripts + and – refer to forward and backward directions, η_i and η_j are dielectric impedances of the incident and transmitted sides, respectively (defined in terms of the background dielectric permittivity ε_i and permeability μ_i by $\eta_i = \sqrt{\mu_i / \varepsilon_i}$).

In general, there are two contributions to the dynamic conductivity (or dielectric constant) of a thin layer as shown in Chapter II; that due to interband transitions, and a component due to intraband transitions. Although we shall see below that the DT spectra are dominated by the real part of the interband conductivity, for completeness we include the full conductivities (ignoring scattering) from recent theoretical work as following [16]:

$$\sigma^{intra}(\omega, \mu) = -\frac{ie^2 g_s g_v}{\hbar^2 (\omega + i0) 4\pi} \{\int_0^\infty E dE (f'(E) + f'(-E))\}, \tag{4.2}$$

$$\sigma^{inter}(\omega,\mu)=\frac{e^2 g_s g_v}{16\hbar}[f(-\hbar\omega/2)-f(\hbar\omega/2)] + \frac{ie^2 g_s g_v}{8\hbar\pi}\{P.I.\int_0^\infty dE(f(-E)-f(E))(\frac{1}{2E+\hbar(\omega+i0)}-\frac{1}{2E-\hbar(\omega+i0)})\}, \quad (4.3)$$

where $f(E)$ is the Fermi distribution function, f' is $\partial f/\partial E$, k_B is the Boltzmann constant, μ is the Fermi energy and g_s=2, g_v=2 are the spin and valley degeneracies [17]. Although we know from Mid-IR DT spectrum later that there are multiple doped layers in the sample, for the simulations here, we still calculate the transmission spectrum of the multilayer structure of Fig. 4.1, with transfer matrices for 20 undoped graphene layers (Fermi level at the Dirac point) and 1 doped layer with a Fermi level of 350 meV. This model is close enough to explain the main feature of the experiment data at this spectrum range, since the contribution from other doped layers at this energy range doesn't give significant contribution to the main feature as we will see later. The matrices are multiplied together to give the total transmission of the probe beam through the multilayer epitaxial graphene structure; the contribution from the buffer layer is ignored, and a dielectric constant of 9.66 is used for 4H-SiC substrate.

The calculated transmission spectrum is shown in Fig. 4.4 for various electron temperatures, where for simplicity we have assumed the temperature to be the same for all layers (in reality T_e may differ for the doped and undoped layers). At low temperature (10K), the transmission spectrum shows an absorption edge at $\hbar\omega = 2\mu_d$ (where μ_d is the Fermi level relative to the Dirac point in the doped layer) as one would expect from the simple picture of interband absorption discussed previously. As the temperature increases, the absorption edge due to the doped layers broadens due to smearing of the carrier distribution around the Fermi level, and the undoped layers contribute a broad peak at low energy.

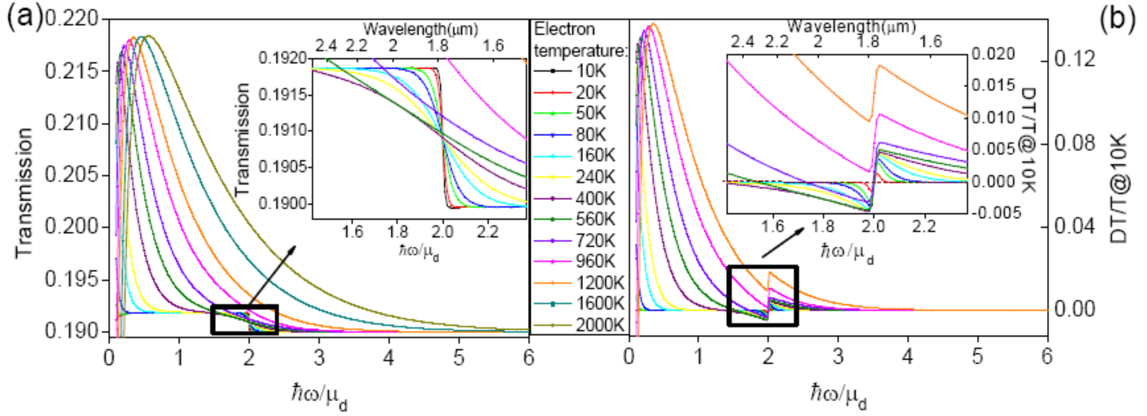

Figure 4.4: DT Signal Simulation. (a) Simulated transmission curves at different electron temperatures. In the inset, the transmission curves at low electron temperatures are shown expanded for frequencies around the two DT zero-crossings. (b) Simulated DT/T curves at different electron temperatures with lattice temperature at 10K. In the inset, the DT/T curves for low electron temperatures are expanded in the vicinity of the two DT crossing points. Both figures share the same legend.

In order to compare simulations with experiments directly, we show in Fig. 4(b) the calculated DT spectrum for an initial electron temperature of 10 K (i.e. the DT spectrum is the transmission spectrum for an elevated electron temperature minus the transmission spectrum for 10 K). The DT spectra show the upper and lower zero crossings at energies ($\hbar\omega = 2\mu_d$ and $\hbar\omega \approx 1.5\mu_d$ respectively) close to those observed in the experiment. Immediately following the pump pulse, the initial hot electron temperature is higher than 1200 K for our experimental excitation intensity; from the simulation this implies a positive DT signal over the entire spectral range, exactly as observed.

The simulation indicates that the DT spectra should show a sharp slope around the upper ($\hbar\omega = 2\mu_d$) zero crossing, whereas the experimental DT spectra show a rather shallow slope. This could occur if the substrate temperature is slightly elevated above the cold finger temperature. Alternatively, this may be a consequence of sample inhomogeneity: the 40-μm probe spot is relatively large compared to the coherence length of the graphene layers, which evidently has a significant variation of the Fermi level with positions. Similar indications of

inhomogeneity have been found in transport measurements, indicating a transport phase coherence length in excess of 1 μm[2] and in recent measurements of the spatial variation of the local carrier density [18]. DT spectra and time scans were also taken at various positions on the sample over several square millimeters of area, revealing the effects of inhomogeneity on a large domain. The effect of the varying Fermi level on the DT time scans is shown in Fig. 4.5. Shifts of the DT zero crossings with position showed that the Fermi energy varies by as much as 35 meV across this sample surface.

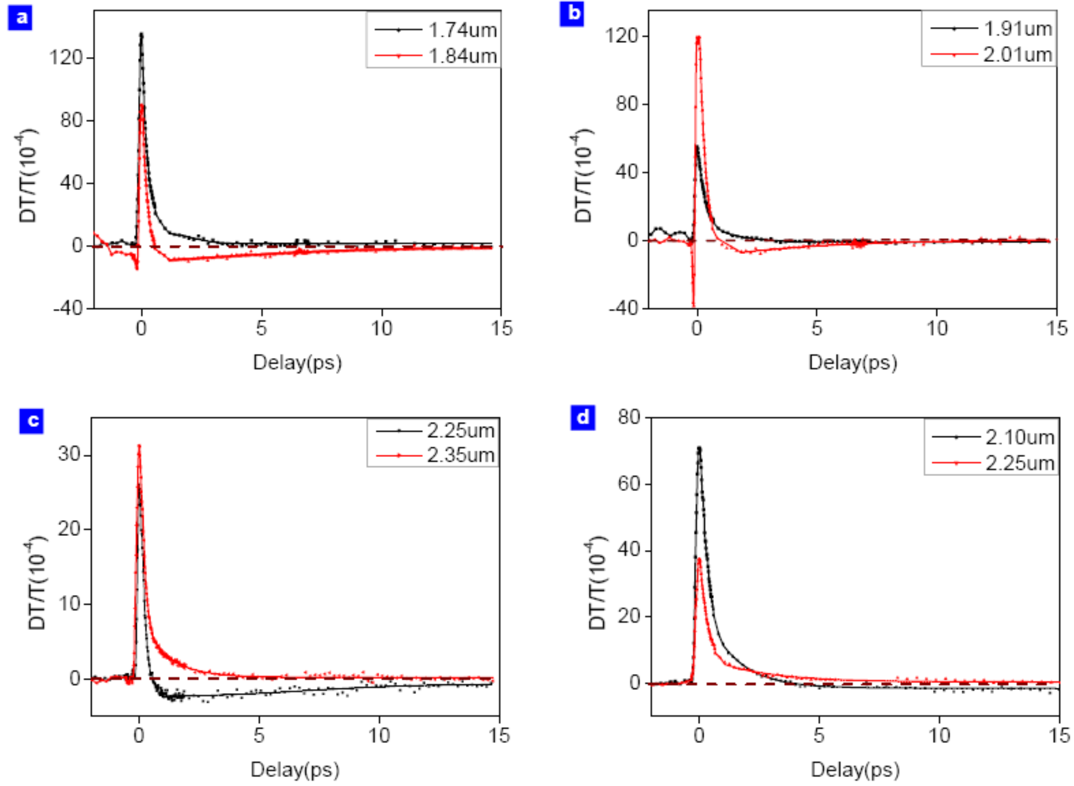

Figure 4.5: Sample Inhomogeneity. DT time scans taken on different positions of the sample. (a) and (b) The upper zero crossing shifts at two different positions of the sample. (c) and (d) Shifts of the other lower zero crossing points at two different positions of the sample. All the data are taken at 10K, with 500uW at 800nm pump. The dashed lines (wine) marks where the DT signals are zero. All the DT tails are simply fitted by sigmoidal curve.

Close examination of Fig. 4.4 shows that when the probe energy is between the two zero DT crossings (inset, Fig. 4.4(b)), the transmission curve (inset, Fig. 4.4(a)) does not relax

monotonically with decreasing electron temperature; it decreases to a minimum around 400 K and then turns back and increases with decreasing temperature. Thus we can interpret the dynamics of the DT signal when probe beam is tuned just below the Fermi level. The electron temperature following the pump pulse is in excess of 720K and the DT signal is positive; as the carriers lose energy due to electron-phonon interactions, the DT amplitude decreases and becomes zero for an electron temperature of approximately 700 K. The DT signal is then negative and reaches its maximum negative amplitude for an electron temperature of 400 K. With further cooling, the DT amplitude approaches zero. The time delay at which the DT flips sign should be expected from the model to increase with the lattice temperature, which is exactly observed in the experiment (inset of Fig. 3(a)). Additionally, the amplitude of the negative component in DT signal decreases quickly with increasing lattice temperature, and almost disappears at 180 K in the experiment.

In contrast, when the probe wavelength is either above the upper or below the lower zero crossing, the transmission decreases monotonically with the electron temperature, and the DT decay curves are only weakly dependent on lattice temperature, as is apparent in Figs. 4.3(b) and 4.3(c).

Additional simulations performed by excluding various contributions to the total conductivity reveal that the dominant contribution is the real part of the interband conductivity. Recent theoretical work has predicted that the imaginary part of the interband contribution to the conductivity is negative, leading to a novel TE mode propagating in the plane of the graphene layer in the frequency range of $1.667\mu < \hbar\omega < 2\mu$ (i.e. between the zero-crossings of the total imaginary part of the conductivity). This mode is unique in graphene and does not exist in conventional 2D electron systems such as GaAs/AlGaAs quantum-well structures

[16]. We note however that the lower zero crossing observed in our experiment has a different origin, since our probe beam is normally incident on the sample and does not couple to the plasmon mode, we find that including the imaginary intraband conductivity only results in a shift of the lower zero crossing (less than 5%), and this contribution to the conductivity cannot be isolated in our normal-incidence DT experiment. Our DT spectra are well described by interband transitions, the single-particle density of states for linear dispersion, and no electron-hole interaction.

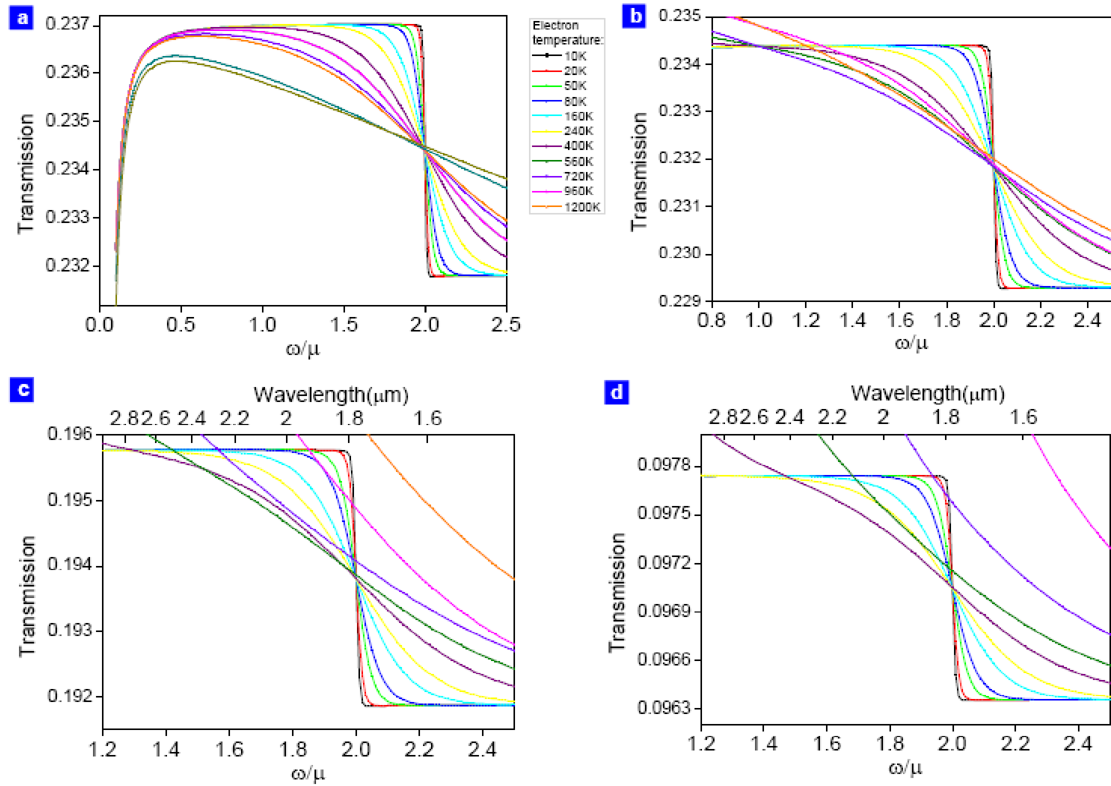

Figure 4.6: DT Crossing Points Shift with the Number of Undoped Layers. (a) Transmission spectrum with no undoped layers. (b) Transmission spectrum with 1 undoped layer. (c) Transmission spectrum with 20 undoped layer. (d) Transmission spectrum with 100 undoped layer. All the figures share the same legend.

Simulations also show that the DT spectrum depends, in detail, on the multi-layer structure of the epitaxial graphene. This is shown in Fig. 4.6: if only the doped layer is included, and the undoped layers are ignored, we find the 2.35-μm (lower) zero crossing disappears. When a

single undoped layer is added to the simulation, zero crossing appears at around μ_d; this zero crossing shifts quickly from 1.1 μ_d to 1.5 μ_d as the number of undoped layers is increased from 1 to 20, and slowly afterwards to 1.6 μ_d; for 100 layers. Thus, our DT experiment provides a strong corroborating evidence for the epitaxial graphene structure determined using other methods [8, 9, 19, 20]; our best fit to the data is obtained for one conducting layer and 20 undoped layers.

We note that our calculations of the DT spectra assume that the quasiparticle plasma can be described by a thermal distribution characterized by a single electron temperature T_e in all layers; this corresponds to an assumption of a relatively fast electron-electron scattering process. The 100-fs, 800-nm pump pulse excites electrons from the valence band to 428 meV above the Fermi level in the conducting layer and 777 meV above the Fermi level (Dirac point) in the undoped layers. Within the time resolution of the experiment, the electron distribution appears to be thermal in the experimental DT spectra. From the time delay of zero crossing DT point at 10 K, we find that the hot electron temperature relaxes to around T_e = 420 K (36 meV) on the time scale of 1.7 ps by emitting two or three 197 meV [21] optical G phonons or one to two 330 meV D phonons [21]. The relaxation afterwards is mainly due to the relatively slow acoustic phonon scattering process.

The dynamics of the DT amplitudes [Figs. 2(b, c) and 3] do not give the hot carrier cooling directly. To determine the electron temperature T_e as a function of time it is necessary to use the simulation results to calculate the DT amplitude at a given probe wavelength for each value of the temperature. This will be discussed in a separate section later.

4.2 Doping Profile and Screening Length

One of the key questions to be addressed for the development of epitaxial graphene devices is: what is the actual doping profile of the layers? A determination of the exact doping profiles and interlayer screening effect of stacked graphene layers is desired to understand the electric field effect for future multilayer epitaxial graphene based nanoelectronic device. The dielectric screening of two-dimensional electron gases has been of interest to fundamental physics since the 1970s [22-25]. Accumulating pieces of evidence indicate that epitaxial graphene behaves as multilayered graphene (as opposed to graphite) [19, 26], where the layer closest to the substrate is highly doped and the electron density drops rapidly for subsequent layers. The doping of the first few layers in epitaxial graphene is caused by a built-in electric field at the SiC-graphene interface [7, 11]. Strong covalent bonds exist between the substrate and the first layer and since charges can be transferred from SiC to the graphene layers (depending on the interfacial geometry) this results in a net doping of these layers. This charge transfer process doesn't rely on the doping of the SiC substrate. It originates from the SiC and graphene interface only [14]. Theoretical calculation in absence of interlayer hopping in a stack of 2D electron gases was considered back to 1971[22]. Interlayer hopping modifies the picture significantly, and this is considered with a simple theoretic model of finite stacks of graphene planes with interlayer electronic hybridization described by a nearest-neighbor hopping term. The interlayer hopping enhances Friedel-like oscillations in the charge distribution and lead to the changes in the sign of the charge in the neighboring layers and thus the screening length is determined to be 2-3 graphene layers superimposed to significant charge oscillations [27]. To be closer to epitaxial graphene, the rotationally stacked layers under an external field are considered in the context of graphene bilayers only [28, 29]. A more realistic model with rotationally stacked multiple graphene layers on an

interfacial carbon buffer layer covalently bonded to a SiC substrate is expected on the theoretical side to address this problem. Experimentally, electronic transport measurements are primarily sensitive to the highly conducting layer [30], while Landau level spectroscopy is mainly sensitive to the nearly-neutral layers on the top [9, 31]. Angle resolved photoemission spectroscopy (ARPES) is used to study the doping level of the very top layer of thin Si-face grown samples with 1-4 layers respectively [32]. In another work, a configuration of field-effect transistor with top and bottom gate electrodes was used to measure the change in resistance of various exfoliated graphite-film thicknesses as a function of the voltages applied to the two gates. The results theoretically fit the screening length to be 1.2±0.2 nm which is away from the theoretical prediction [33]. A direct measurement of the doping profiles of different layers in a single epitaxial graphene sample is not available so far due to experimental limitations.

4.2.1 Experimental Setup

In the previous section we show that ultrafast infrared probe spectroscopy provides an accurate determination of the Fermi level in the highest conducting layer [18]. In this work, we extended the spectral range of the probe to longer wavelengths so that we could determine the doping density in each of the first three monolayers of a multilayer sample, and therefore obtain a quantitative measurement of the interlayer screening length.

The principle of the experiment is to excite electrons high into the conduction band by an 800-nm pump; electron-electron scattering on a time scale short compared to the 150 fs pulse width establishes a hot thermal distribution, followed by acoustic-phonon-mediated carrier cooling. Since the carrier occupation probability above (below) the Fermi energy is increased (decreased) by the pump, the differential transmission (DT) signal of probe transition above

(below) the Fermi level is positive (negative). Thus, after the initial carrier cooling, the DT signal crosses zero at a photon energy corresponding to twice the Fermi level for each doped layer. By determining the positions of the zero crossings we thus determine the Fermi levels present in the sample. The Fermi levels are sufficiently different (i.e. the screening length is short) that the layers can be well separated spectrally.

The sample used in this experiment, #7J8 from Georgia Tech, is different from sample #598 referred to in the previous section since the later was irretrievably damaged in an accident. #7J8 is also an ultrathin epitaxial graphene film produced on the C-terminated face of single-crystal 4H-SiC by thermal desorption of Si. The structure of the sample is shown in Fig. 4.7(c); it consists of 63 layers with multiple doped and undoped graphene layers. The experimental setup is similar to those described in Chapter 3 and previous sections, except that a DFG is used to generate mid-IR probe wavelengths after the OPA. The pump and probe beams are collinearly polarized and focused onto the sample to ~80 μm and 40μm diameter spots in the case of the OPA probes or ~150 μm and ~80 μm spots with the DFG probes. The probe beam after the sample is filtered in a monochromator and detected by either an InGaAs photodetector or liquid nitrogen cooled HgCdTe or InSb photo detector and a lock-in amplifier referenced to the 4.2-kHz mechanically chopped pump. Since the negative DT tails are washed out at room temperature as shown in Fig. 4.3, the sample is mounted in Helium flown cooled cryostat and all the experimental results shown in this paper are performed at 10 K.

A broad range of probe wavelengths from 1.2 μm to 7 μm was scanned except in the gap between 2.5-2.7 μm and another gap between 5.8-6.7 μm (and beyond 7μm). This first was due to the laser tunability gap between the far end of the OPA idler and the near end of the

DFG. The longer wavelength gap was due to multi-photon absorption by the SiC substrate [19]. The DT signal from the SiC substrate contributes to the time-zero signals (within the pulse width only) and is typically two orders of magnitude smaller than the graphene DT signal. Different pump powers were used over a different range of probe wavelengths to get good signal to noise ratios – the determined Fermi level position is insensitive to pump power.

4.2.2 Experimental Results

Between 1.4 μm and 2.0 μm, this sample shows a very similar behavior to sample #598. As shown in Fig. 4.1(b), immediately following the pump pulse, the DT signal is positive over the entire probe spectral range. The electron temperature is above 1000 K right after the pump excitation and fast initial thermalization process for any pump power used in this experiment. Depending on the probe wavelength, the DT signal becomes negative within several ps if the probe transition falls right below the Fermi level, otherwise it remains positive until the signal decays away. The top plot of Fig. 4.7 (b) shows the DT tails flip sign between 1.7 μm and 1.75 μm which indicates a Fermi level of 355 meV-365 meV above the Dirac point for the most heavily doped layer. However, the DT tails don't flip back to positive value at 2.35 μm as happened in the previous sample; the second plot in Fig. 4.7(b) shows that the positive DT tails recover around 2.7 μm and flip back to negative values at 3.0 μm which indicates a Fermi level of 207-222 meV above the Dirac point. Since inhomogeneous broadening for the most heavily doped layer of this sample was measured to be less than 10%, this crossing point is due to another doped graphene layer. The third DT tail crossing is between 4.38 μm and 4.45 μm as shown in the third plot in Fig. 4.7(b), which corresponds to 139 meV -142 meV above the Dirac point. The exact position of the fourth zero crossing is not clear as shown in the bottom plot of Fig. 4.7(b). Due to the SiC

absorption between 5.8 μm and 6.76 μm and beyond 7 μm, differential reflection will have to be used to investigate this energy range in the future. However from the trend of the relaxation of negative DT tails as shown in Fig. 4.7(b), the fourth zero crossing is estimated to be a little bit over 6.9 μm.

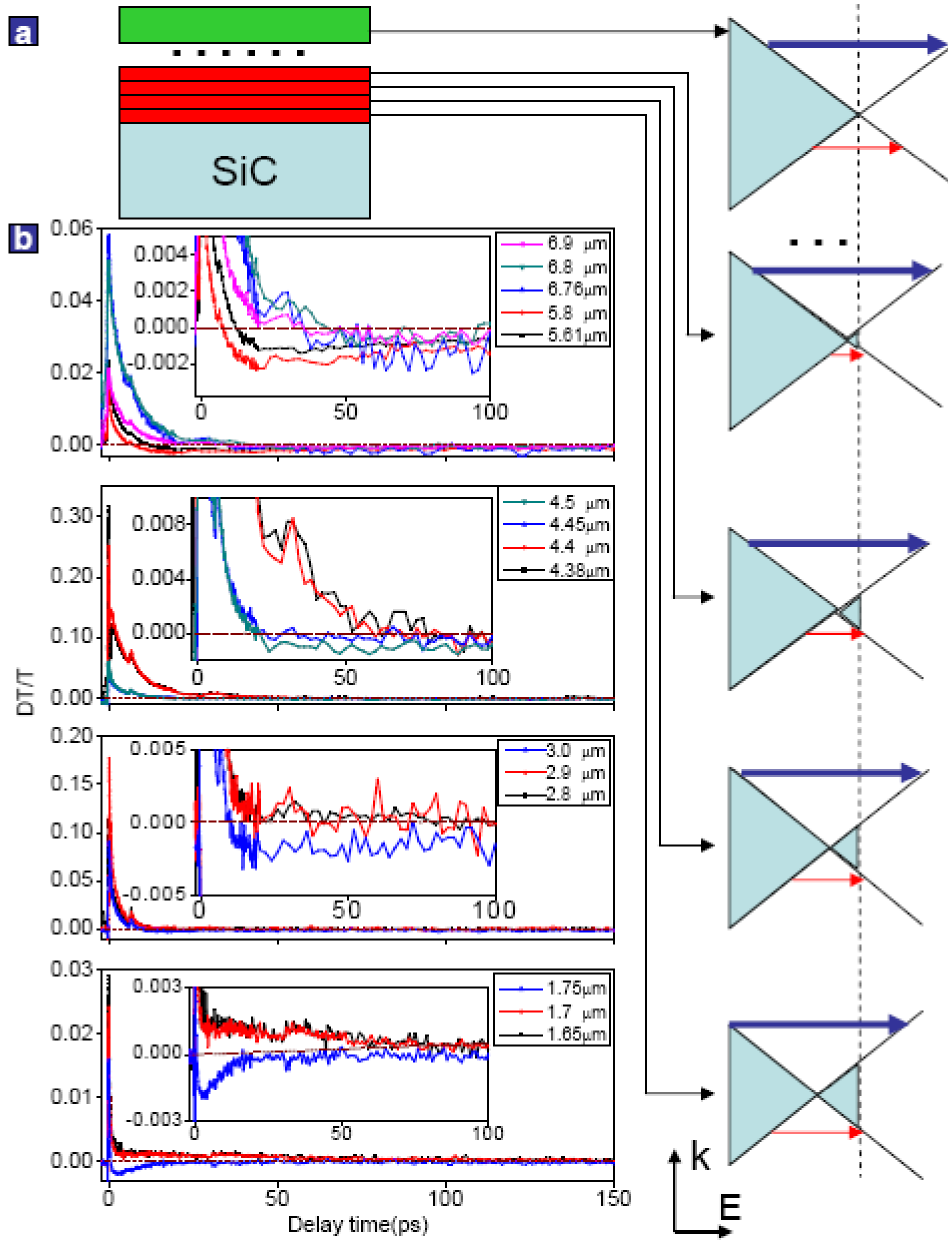

Figure 4.7: Sample Structure and DT Crossings. (a) Schematic diagram of sample structure, energy dispersion and Fermi levels of the graphene layers. The sample has several highly doped layers (red) near the SiC substrate, followed by multiple undoped layers (green) on top. The energy dispersion near the Dirac point of each layer is schematically shown. The Fermi level is labeled with a dashed line (black). Blue solid lines show the transitions induced by an 800-nm optical pump pulse; the red lines correspond to probe transitions at different energies around the DT/T zero crossings (discussed in the text). (b) Time scans of different probe wavelengths around four DT zero crossings. In the insets the DT/T relaxation tails are shown expanded around zero DT/T. The dash line (brown) marks where the DT/T is zero. The 800nm pump powers are 1mW, 9mW, 9mW and 1 mW from top to bottom respectively.

4.2.3 Interpretation of the Results

Figure 4.8(a) shows the calculated DT spectra with an initial electron temperature of 10 K using the same dynamic conductivity simulation as in the previous section. In this simulation I included four highly doped layers with doping densities identical to those measured in the experiment. However, there are two significant discrepancies between this simulation and the experimental results: first, the slope of the DT curve around the Fermi crossing is not as sharp as the one measured in the experiment; second, the DT tails stay negative over most of the scanning spectra range except the in the narrow range close to the DT crossing.

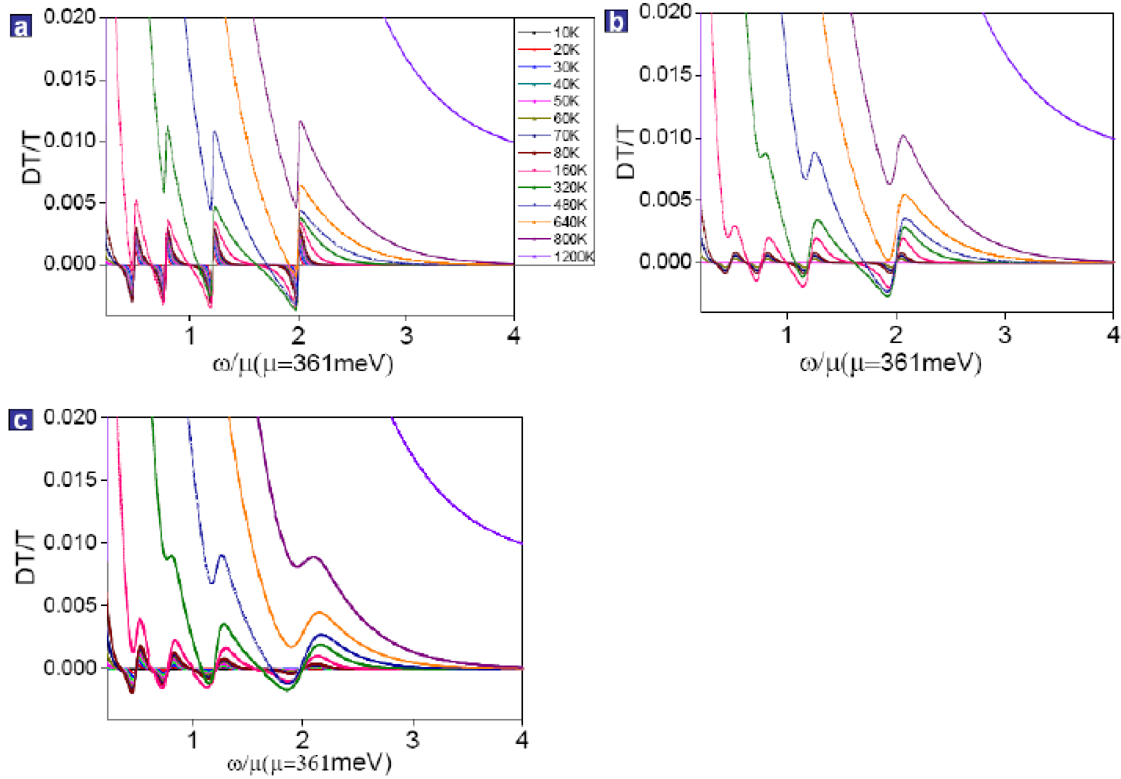

Figure 4.8: DT Signal Simulation. (a) Simulated DT/T curves at different electron temperatures with lattice temperature at 10K with no inhomogeneous broadening. (b) Simulated DT/T curves at different electron temperatures with lattice temperature at 50K with no inhomogeneous broadening. (c) Simulated DT/T curves at different electron temperature with lattice temperature at 10K with a 10% inhomogeneous broadening of the Fermi level. All the figures share the same legend.

Possible reasons for these discrepancies could include an elevated lattice temperature and inhomogeneous broadening due to sample nonuniformity. The elevated lattice temperature is an experimental artifact due to the temperature gradient between the temperature sensor and the graphene sample. Fig. 4.8(b) shows the DT spectrum simulation with an initial electron temperature of 50K. From the simulation, the positive DT signal at low electron temperature decreases significantly, and the DT curve slope at crossing points get smoother when simulated at elevated lattice temperature. The interfacial geometry and charge impurity fluctuation causes the inhomogeneity of the doping profiles in graphene layers. A typical intrinsic disorder length scale is measured to be 30 nm in exfoliated graphene [34], which is far less than the extent of my probe spots. Since DT experiments over different points on this sample show fluctuations of the DT crossing points of the most heavily doped layer to be less than 10%, in Fig. 4.8(c) DT spectrum with initial electron temperature of 10 K, but including an inhomogeneous broadening of the Fermi level of 10% of each layer. Numerically, this is done by convoluting with a Gaussian distribution function is simulated. We can see that adding both effects brings the simulation closer to the experimental observation. However, the DT signs still flip at the Fermi level transitional energy.

Figure 4.9(a) shows a fitting of the Fermi level with a simple decay curve; the best fit indicates the doping intensity decays by a factor of 0.38 in each layer. Assuming this decay rate, it takes about 8-9 layers to decay to the "undoped" carrier density of $1.5*10^{10}$ cm^{-2} as measured in a recent Landau level spectroscopy experiment [9, 31]. This decay rate corresponds to a screening length of 3.41 Å or converted to single graphene layer which matches the 2-3 layers screening length predicted from the theoretical work considering an external field on finite stacks of graphene planes [27]. and theoretical calculations for

graphite intercalation compounds give similar screening lengths of 3.8 – 5 Å [23, 24]. ARPES measurement [32] gives a shorter screening length of 1.4 -1.9 Å on a Si face 6H-SiC sample. However Si-face grown epitaxial graphene has an interface and structure very different from C-face grown samples [35]. In addition, the measurements are done on the top face for samples of different thicknesses instead of different layers on a single sample.

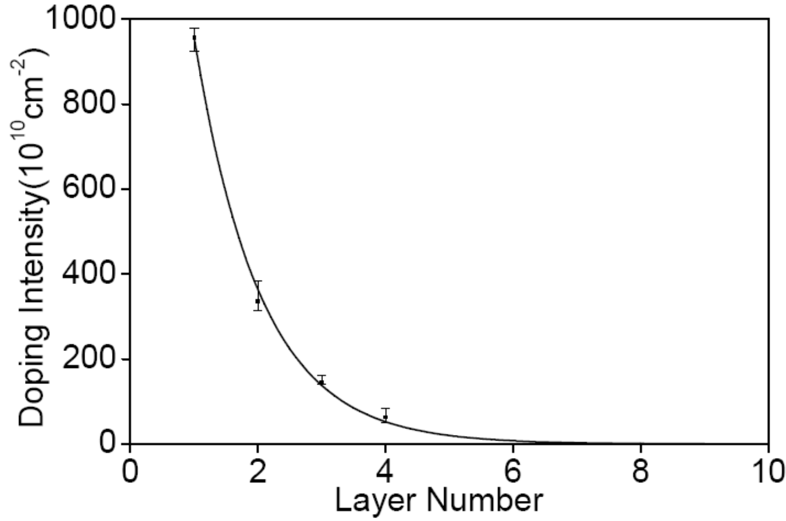

Figure 4.9: Screening Length Fitting. The limit of the error bar is determined from the probe wavelength before and after the DT tails crossing with a clear positive or negative DT sign. For the uncertainty of the fourth doped layer, we set the low energy limit of the error bar at 7.5μm which is far beyond the scanning range for confidence. The solid curve is the fit with linear decay $N^n = N^1 * r^{n-1} = N^1 * \exp(-l_n / l_s)$, where $N^1 = 9.56 * 10^{12} cm^{-2}$ is the Fermi level of the first doped layer, *r=0.379562* is the decay of the doping intensity by each layer, l_n is the distance between the nth layer and the first doped graphene layer and $l_s = 3.41$ *Å* is the screening length which is about one graphene layer.

In conclusion, I have spectrally resolved the precise doping profile of heavily doped layers and determined the screening length to be 1 layer in carbon-face grown epitaxial graphene using ultrafast pump-probe spectroscopy. The measured DT spectrum feature can be well explained by a dynamic conductivity simulation when the in-plane disorder and elevated lattice temperature effect are incorporated.

4.3 Interlayer Thermal Coupling of Hot Electrons

The distance between adjacent graphene layers is measured to be 3.368 A in carbon-face epitaxial graphene which is between the value of bulk graphite and turbostratic graphite. This large spacing suggests a relatively weak coupling between layers. X-ray diffraction reveals a significant density of stacking faults which eliminate the effect of AB stacking order that can destroy the graphene electronic characteristics. Experimentally, the charge carriers in epitaxial graphene are found to be chiral and the band structure is clearly related to the Dirac cone[1, 2, 9, 13], thus the epitaxial graphene appears to consist of stacked, non-interacting graphene sheets, and this is the model we have used for simulation in previous sections. The doped layer is believed to contribute to the electric transport in the magneto transport measurement [2]. However the role of the multiple undoped layers in electric transport is largely unexplored [20]. The understanding of existence and dynamics of coupling between the carriers in doped and undoped layers is an important issue for high-field transport in epitaxial graphene and epitaxial graphene based optoelectronic and plasmonics.

4.3.1 Experimental Setup

The sample used here is still #7J8. Its most heavily doped layer is characterized to be 355-365 meV above the Dirac points from the previous section. To study the interlayer thermal coupling, instead of using an 800-nm pump to excite hot carriers in all the layers, here we excite the hot carriers in the undoped layers using 1.9-μm (1.8-μm) pump pulse. This corresponds to the transition below the Fermi level of the most heavily doped layers (the inhomogeneity is measured to be about 15 meV in this layer on this sample). So carriers in the first doped layers aren't excited by the pump pulse directly due to Pauli blocking. Electrons in all the other layers can be excited. A weak probe pulse with degenerate wavelength of 1.32 μm (1.4μm) at various time delay respective to the pump pulses is used to

probe right below or high above (110 meV or 68meV) the Fermi level of the most heavily doped layer.

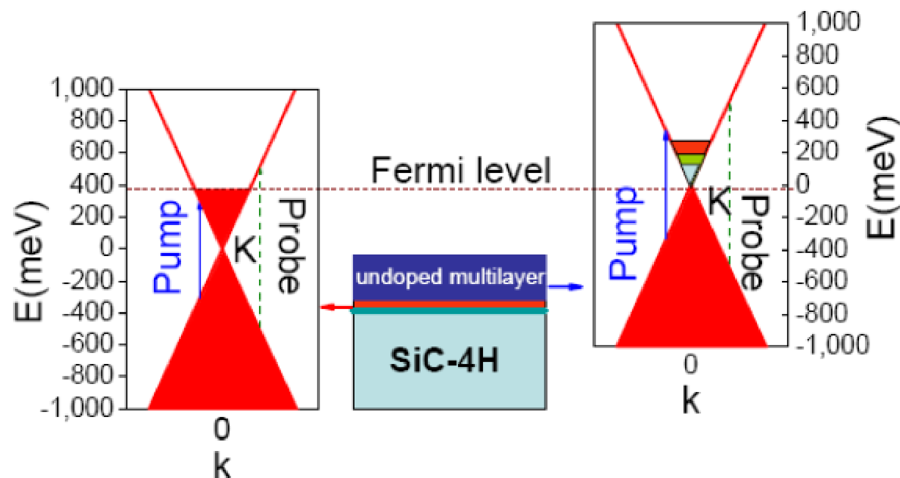

Figure 4.10 Sample Structure, Energy Dispersion Curve and Experimental Scheme. The sample has a buffer layer (green) on the SiC substrate followed by several heavily doped layer (red) and many undoped layers (blue) on top. The Fermi level is labeled with a dashed line (brown) lying at 360 meV (from the later data) above the Dirac point of the most heavily doped graphene layer and passing through the Dirac point of the undoped graphene layers. On the left,we also plot of filling of the electrons of other well characterized doped layers. The blue solid lines show transitions induced by the 1900-nm optical pump pulse where the dashed lines correspond to the transitions of the probe.

Since hot carriers in the undoped layers are below the probe photon energy, it can only contribute to the positive DT signal. The negative DT signal, if it is observed, comes from the Fermi level smearing in the most heavily doped layers. The beam is then moved onto a GaAs sample afterward with all the same experimental conditions, since the two photon energy is barely above the bandgap of GaAs, the resulting two photon DT signal on GaAs is considered as a cross correlation of the pump and probe pulses. It is also used as a reference for time-zero to determine the rising time of the DT signal on expitaxial graphene to obtain coupling strength between doped and undoped layers at the initial stage.

The degenerate pump-probe setup is described in Chapter 3: a 100-fs 250-kHz amplified Ti: Sapphire laser at 800 nm pumps an infrared optical parametric amplifier (OPA) with signal

wavelength tunable from 1.1 to 1.6 μm and idler wavelength tunable from 1.6-2.6 μm. The idler goes through a 1.9-μm (1.8-μm) filter (with 10 nm bandwidth) and is used as a pump beam. The signal goes though a 1.32-μm (1.4-μm) filter (with 10 nm bandwidth) and is used as a probe beam. The pulse widths of both pump and probe beams are estimated to be around 250 fs after broadening of the polarized beam splitter and other optics. The beams are collinearly polarized and focused to about 50-μm and 100-μm diameter spots sizes in diameter on the sample, respectively. The probe beam, after the sample is detected by an InGaAs photodetector and lock-in amplifier referenced to the 4.2-kHz mechanically chopped pump. The sample temperature is controlled over a range of 10-300 K.

4.3.2 Experimental Results

Figure 4.11 shows a DT scan on a graphene sample with 1.9-μm degenerate pump-probe at 10K: the DT signal goes to negative in 2 ps after the pump excitation. Since the signal from other doped or undoped layers only contribute to a positive signal, this negative DT signal can only come from the Fermi level smearing due to hot carriers in the most heavily doped layer. The excitation of the hot carriers in this layer doesn't come from direct pump excitation and there must be interlayer thermal coupling going on to transfer heat to the most heavily doped layer to excite the hot carriers.

To understand the interlayer coupling mechanism, the beam is moved on to a GaAs sample afterward to determine the in-situ time-zero. Since the two-photon energy at 1.8 μm for the degenerate pump-probe, is below GaAs band-gap; 1.9 μm /1.32 μm and 1.8 μm/1.4 μm pump-probes are used instead. The two photon DT signal on GaAs is considered as the cross-correlation of the pump and probe pulses, which has intermediate response time. This can be

used as a time-zero reference to determine the rise time of the DT signal on expitaxial graphene to acquire coupling time between layers at the initial stage.

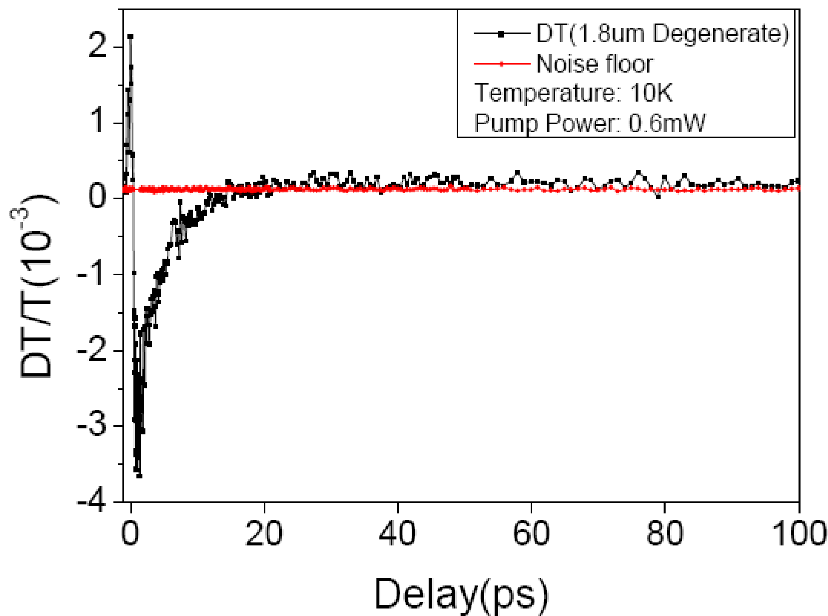

Figure 4.11, Degenerate Pump-probe DT Time Scan. DT time scan with 0.6-mW 1.8-µm pump and 1.8-µm probe at 10 K.

Figure 4.12 (a) and (c) show the rise time of the DT signal on the sample and the full DT scans at different temperatures are shown in (b) and (d). Since the signal on the GaAs is two -photon absorption which follows the cross-correlation of the pump-probe pulses. However, the DT on the epitaxial graphene follows the integration of the pump-probe cross-correlation instead. From the Fig. 4.12 (d), we see the DT signal on graphene sample generally follows the integration of the cross correlation signal on GaAs which means the coupling time is almost instantaneous.

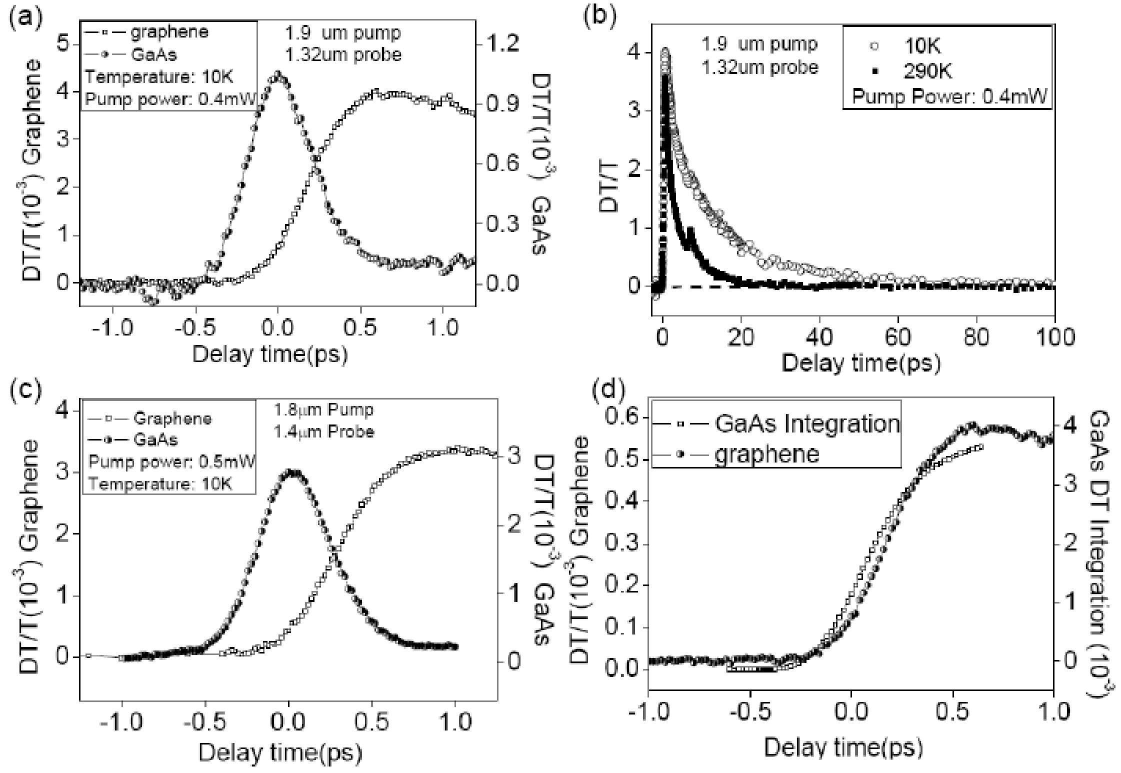

Figure 4.12: Rise Time of the Interlayer Thermal Coupling (a) DT time scans on epitaxial graphene and GaAs with 400μW pump at 1.9 μm and 1.32 μm probe. (b) The full DT time scan on epitaxial graphene at different temperatures with 1.9 μm pump and 1.32 μm probe. (c) DT time scans on epitaxial graphene and GaAs with 500μW pump at 1.8 μm and 1.4 μm probe. (d) Integration of GaAs cross-correlation signal with 1.9 μm pump and 1.32 μm probe. The dash line marks where the DT singal is zero in all figures.

4.3.3 Interlayer Thermal Coupling Mechanism

This experiment, to our knowledge, is the first direct experimental observation of heat transfer between hot carriers of different graphene layers. There are many possible coupling mechanisms account for this effect. Heat transfer between graphene layers can be due to phonon-phonon coupling between layers. The hot electrons in each layer can transfer their heat to the in-plane phonons and they can couple to each other and then transfer the heat back to heat the electrons. The hot phonon effect is still under investigation and is discussed later in this chapter. However, from the electron-phonon coupling time measured from previous section, this mechanism doesn't match the instantaneous coupling time observed in the

experiment. So, the direct coupling between the electron states of the doped and undoped layers is more likely the main mechanism that contributes to the instantaneous coupling process. Although stacked graphene layers are electronically decoupled in a perfectly rotationally stacked structure, defects in one layer can introduce scattering within the layer and coupling to electron states in the other layers. The speed of this process is comparable to the electron-electron scattering rate [20]. Remote polar phonon scattering due to the SiC substrate can be another possible medium. However this effect is considered to be ineffective due to weak polarizability of the substrate and relatively high phonon frequencies associated to hard Si-C bonds [36]. Also, all the phonon related processes need a relative longer coupling time to transfer the heat.

In conclusion, we have observed the coupling of the hot carriers between different layers in epitaxial graphene. A direct coupling between electronic states due to defects is considered to account for most interlayer heat transfer mechanisms shown in the experimental results. However, theoretical work is expected to fit the experimental data to explain the detailed mechanism accounted for this effect.

4.4 Polarization Dependence

The pump-probe beam polarizations are changed to various combinations of circularly and linear polarized light to study possible dynamics of excited spin polarized carriers in epitaxial graphene. However, within the time resolution of this experiment, we observe no polarization anisotropy.

4.4.1Experimental Setup

For polarization-dependent measurements, a probe beam (idler of OPA) and 800nm pump go through a half or quarter waveplate respectively to get right/left circularly polarized light or

switching between crossed-linear and collinear beams. The beams are respectively focused to 40-μm and 80-μm diameter spot size in diameter on the sample. All the experiments are performed in a 10K environment. The probe wavelength is fixed at 1.8 μm due to the high cost of the waveplate. Different samples are probed so that wavelengths on each sample can be both right above and below the Fermi level of the most heavily doped layer. The pump and probe polarizations are switched between linear, right or left circularly polarized to get the polarization dependent results. The two samples used in this experiment are the same ones used in the experiment described in section 4.1 and 4.2 Both samples (#598 and #7J8) are ultrathin epitaxial graphene films produced on the C-terminated $(000\bar{1})$ face of single-crystal 4H-SiC by thermal desorption of Si.

4.4.2 Experimental Results

Figure 4.13 shows DT time scans at probe energy above the Fermi level of most heavily doped layer with 9 different polarization combinations at 10K. This is measured on the sample with 20 undoped layers. Time scans around time-zero peaks are zoomed in and shown in the Fig. 4.13(b). From the experimental results, all time scans overlap with each other, and fluctuations between different polarization combinations are within the DT noise levels. This means no polarization anisotropy is observed in the DT measurement within the experimental time resolution. Similarly, Fig. 4.14 shows DT time scans at probe energy below the Fermi level with different polarization combinations on the sample with 62 undoped layers. Now the probe wavelength corresponds to the transition below the Fermi level of the most heavily doped layer. The time scans also overlap with each other and show no polarization anisotropy within the DT noise level.

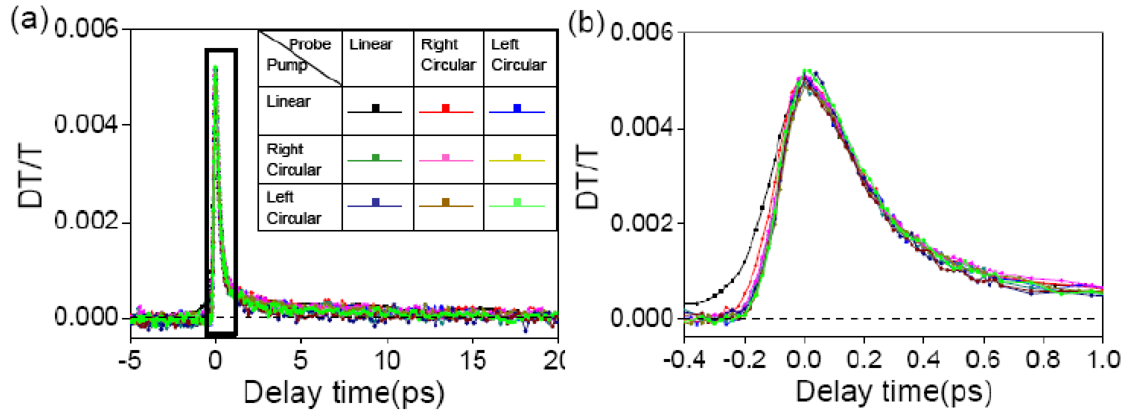

Figure 4.13: Polarization Dependence above the Fermi Level (a) Full DT/T time scans taken at 10K with linear, right and left circularly polarized 800nm pump and linear, right and left circularly polarized 1.8 μm probe respectively. The probe wavelength corresponds to the transition above the Fermi level of the doped layer on the studied sample position. The pump power is 1mW. The part in the rectangular is zoomed into Fig. 4.13 (b). Dashed line marks where the DT signal is zero. Both figures share the same legend. (b) Zoomed in time scans around time-zero peaks at different pump-probe polarization combinations.

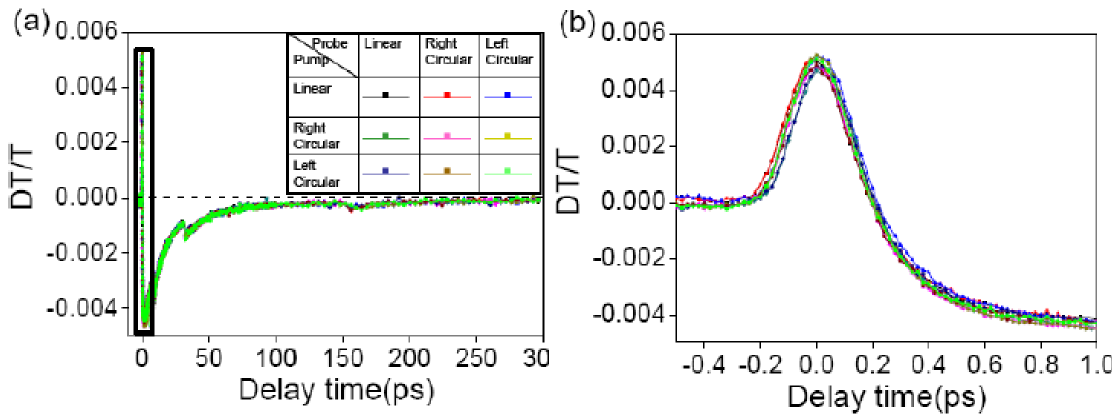

Figure 4.14: Polarization Dependence below the Fermi Level. (a) Full DT/T time scans taken at 10K with linear, right and left circularly polarized 800nm and 1.80um for pump probe beams. The probe wavelength corresponds to a transition below the Fermi level of the doped layer on the studied sample position that is different from the one used in Fig.4 2. The pump power is 1mW. The part in the rectangle is zoomed into Fig. (b). Dashed line marks where DT signal is zero. Both figures share the same figure legend. (b) Zoomed in time scans around the time-zero peaks at different pump-probe polarization combinations.

4.4.3 Experiment Discussion

Now we turn to the interpretation of the lack of polarization anisotropy observed in the experiment. There is some spin polarization anisotropy when the pump beam is right or left

circularly polarized. However this anisotropy disappears after the fast electron-electron scattering occurs because the electron-electron scattering breaks the spin polarization. So a lack in polarization anisotropy observed in the experiment is simply due to the limit of the time resolution, and 150fs pulse width in this experiment sets an upper bound of the electron-electron scattering time.

This result also coincides with the rise time of the time-zero DT/T signal. If thermalization time of electron gas due to electron-electron scattering has occurred on a time scale long compared to the pump pulse, then DT signal shows a rise time longer than the integral of the pump-probe cross-correlation. However, this is not the case observed in the experiment; the rise time of the DT signal is about the same with the cross-correlation of the pump-probe from both Fig. 4.13(b) and Fig. 4.14(b), which means the electron-electron scattering time is below the time resolution of the experiment.

In conclusion, we haven't observed any polarization anisotropy within experimental time resolution, thus we set the upper limit of the electron-electron scattering time in epitaxial graphene through polarization-dependent ultrafast pump-probe DT measurements. The observed upper limit of electron-electron scattering time is below 150fs. A more accurate experiment to further resolve the carrier-carrier scattering dynamics involving higher time resolution is expected in the near future.

4.5 Electron Cooling in Epitaxial Graphene

So far, we have a relative clear picture of excited hot carriers cooling process in epitaxial graphene from the previous experimental results. After the pump excitation of hot electrons, the electrons reach a quasi equilibrium that can be characterized by a single electron temperature within the pulse width in each layer. Due to the fast interlayer coupling, different

layers can interact with each other and reach equilibrium between layers during the pulse width. The very hot electrons then interact with optical phonon modes to reach relative low temperature, say several hundred K, in ps time scale. The slow cooling after is mainly due to the interaction with acoustic phonon modes.

Energy exchange between the electrons and their environment is a key issue in the design of electronic circuits. It is going to play a role in any future graphene-based electronics. Thus it's very important to understand the electron cooling process in epitaxial graphene. As discussed in the previous section, DT amplitudes from our experimental can be correlated to the electron temperature through the electron temperature dependent dynamics conductivity. Thus it is possible to use the same simulation tools to fit the electron temperature cooling in epitaxial graphene. For this purpose, a suitable electron cooling model is needed.

The known system that is closed to graphene is thin metal film. A two quasi-temperature model is used in reference [37] for copper film is described as follow: we assume two separate quasi equilibrium temperature $T_{e,l}$ for the electron and the lattice respectively, they follow the following coupling equations:

$$C_e(T_e)\frac{\partial T_e}{\partial t} = \kappa\Delta^2 T_e - G(T_e - T_l) + P_0(r,t), \tag{4.4}$$

$$C_l \frac{\partial T_l}{\partial t} = G(T_e - T_l), \tag{4.5}$$

where $C_{e,l}$ is the heat capacity of electron and lattice, G is the electron-phonon coupling coefficient. The first term on the right side of equation (4.4) represents thermal-conductivity losses and this term is neglected in the simulation since thermal conductivity is thought to have negligible contribution at the time scales of interest. The second term represents electron-phonon coupling and G is assumed to be constant in this model. The third term

represents the laser-heating source. The essential of this model is to assume two separate quasi-equilibrium temperature for electron and lattice. The heat transfer as also assumed to be proportional to the temperature difference. However this model doesn't fit the data very well, the electron temperature are more likely to decay with a stretched exponential $\exp\left[-(t/\tau)^{1/h}\right]$ with a heterogeneity parameter *h*=3 than the exponential decay from this model.

The dominant cooling mechanism is the energy transfer to phonon modes in nearly any solid state environment. Energy relaxation in a graphene sheet is dominated by transfer to the acoustic and optical phonon modes. The initial cooling of very hot electron plasmas has been discussed by Butscher et al.[38]. The energy relaxation thereafter at relative low temperature are dominated by acoustic phonon modes which has been discussed by R. Bistritzer et al. [39]. In this section, we only focus on the fitting of this slow acoustic phonon cooling part from our pump probe spectroscopy data.

According to the work of Bistritzer et al. [39], the two quasi-temperature model still applies, but the cooling rates are different in the neutral regime and the heavily doped regime. For neutral regime, the electron temperature follows the following equation:

$$\partial_t T_e = -\gamma T_e^2 (T_e - T_L), \tag{4.6}$$

where $\gamma = 1.18*10^3 D^2 (meV^2 * s)^{-1}$,where D is the deformation potential measured in eV, the value of D has been bounded by the transport measurement to be between 10 eV and 50 eV [40], when $T_e \gg T_L$, Eq. (4.6) is solved to be:

$$T_e(t) = \frac{T_0}{\sqrt{t/\tau_0 + 1}}, \tag{4.7}$$

with a characteristic time $\tau_0 = \frac{424}{D^2 T_0^2} \mu s$.

On the other hand, for heavily doped layers, the electron temperature follows:

$$\partial_t T_e = -\gamma_d \frac{T_e - T_L}{T_e}, \tag{4.8}$$

where $\gamma_d = 0.133 D^2 n^{3/2} meV / n\sec$, with n being measured in units of $10^{12} cm^{-2}$.

So from the theory above, the cooling rate is different for the different layers with different doping intensity in epitaxial graphene. With the probe wavelength very close to the Fermi level of the most heavily doped layer, our DT signal is mainly from this most heavily doped layer below 400K, this is shown in Fig. 4.15. The simulation assumes a single electron temperature for all the layers. This is not true when the interlayer thermal coupling is not fast enough to balance the temperature between different layers. The answer to this question is unknown so far.

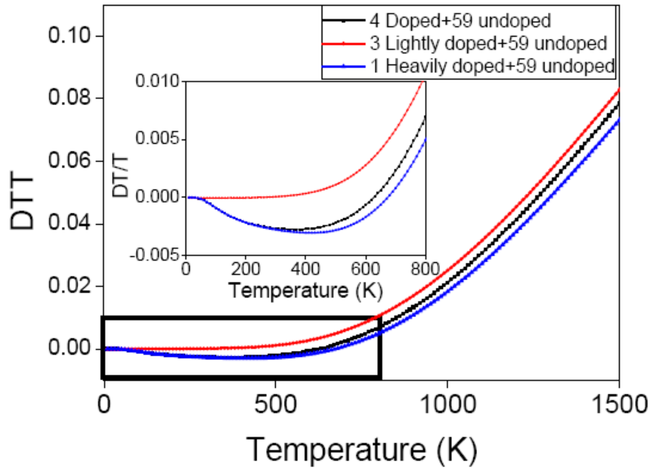

Figure 4.15: The Role of Graphene Layers in Contribution to DT signal. DT/T signal simulation at different electron temperatures with probe wavelength at 1.88 μm, and lattice temperature of 10 K. We assume the doping profile the same as measured in Section 4.2. The black line simulation includes all 59 undoped layers and 4 doped layers. The blue line has only the most heavily doped layer and 59 undoped layers included. The red line, however, includes all 3 lightly doped layers, but not the most heavily doped layer. The black box region is zoomed into the inset.

The simulation of the electron temperature cooling is still in progress as this dissertation is being written. We hope to get more insight into the electron phonon cooling process by fitting our pump probe differential transmission spectroscopy and get the deformation potential D from the fitting.

4.6 Pump Power Dependence-- Hot Photon Effect

The electron-phonon coupling rate is of fundamental interests in device physics. Pump power dependent time-resolved ultrafast spectroscopy, has been demonstrated to be a powerful tool for this purpose. Back in early 90s, this method has been used to determine the electron-phonon couplings in metals like copper [37]. By changing the optical pumping energy and using 2 two quasi-temperature models, we are able to extract the electron temperature and lattice temperatures at various time delays from the transfer matrix simulation, thus we can fit electron-phonon coupling rate from the experimental data.

4.6.1 Experimental Setup

For this experiment, the optical setup is almost the same as the one used in Sec. 4.1. But here, a tunable neutral density filter is added to change the pump power intensity. Sample #598 is again used in this experiment. The characterization of the sample with 800 nm pump beam in Sec. 4.1 shows that the DT signal flips sign at 1.78 μm. This indicates that the Fermi level is between these two probe transitions and it is 350 meV above the Dirac point. Other crossing points are not measured on this sample and we assume the same screening factor with sample #7J8 in the simulation.

4.6.2 Experimental Results

Figure 4.16 (a) shows a DT time scan with different pump pulse energies. The probe wavelength is 1.88 μm which is well below the Fermi level of a doped layer. Following the

transfer matrix method described in Chapter II, a typical simulated DT/T curve of similar situation is shown in Fig. 4.16. It has positive DT signal at the time zero after an excitation and thermalization of hot carriers; the initial electron temperature varies with different pump pulse energies and gives different DT peaks as shown in Fig. 4.17 (b). Then, the hot electrons cool down to a certain electron temperature value (755 K from the simulation) and start to give a negative DT signal as shown in Fig. 4.17 (c). From the transfer-matrix simulation with one heavily doped layer, a negative DT signal can reach its minimum at electron temperature of 375K at any excitation pulse energy so the minimum DT signal should be a constant. This is true for low pump excitation as shown in Fig. 4.17 (d): the curve is almost flat below 80 nJ.

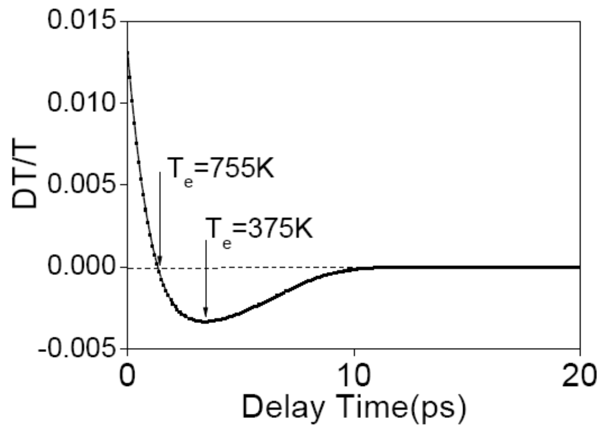

Figure 4.16: Simulated DT/T Time Scan Curve Through Transfer-matrix Method. An exponential decay of the electron temperature is assumed: $T_e(t) = 10+1155*\exp(-t/3ps)$. The electron temperature of the zero DT crossing and the minimum DT are labeled. The model used in this simulation is 17 undoped layers and 4 doped layers with the Fermi level of 350meV above the Dirac point and the screening factors the same as measured in the previous experiment.

However, this is not the case when the pump excitation gets higher. The minimum DT signal starts to drop after some limit. To see this more clearly, we decrease the pulse repetition rate to 62.5 kHz and further increase the pump excitation energy. A DT time scan and zoomed portion at minima are shown in Fig. 4.18 (a) and Fig. 4.18 (b). The pump power dependent of a minimum DT/T signal is shown in Fig 4.18 (c). The minimum DT/T decreases

monotonically with increasing pump power, this high-power effect is beyond the current transfer-matrix simulation and the mechanism is unexplored.

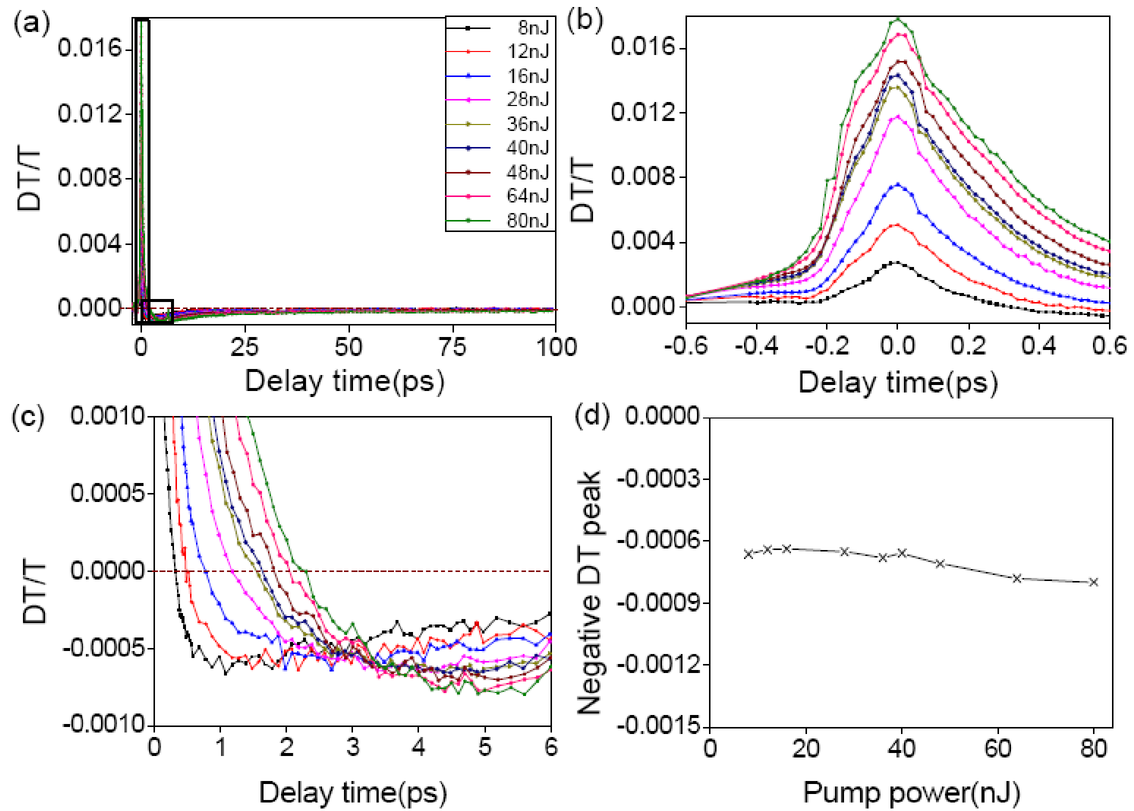

Figure 4.17: Low Pump Power Dependence (a) Full DT/T time scan taken at 10K with 800nm pump power of 8 nJ,12 nJ,16 nJ,28 nJ,36 nJ,40 nJ, 48 nJ,64 nJ and 80nJ. The probe wavelength is 1.88 µm which corresponds to the transition below the Fermi level of a doped layer. Boxed regions from plot (a) are zoomed into figures (b) and (c). (b) Zoomed in DT/T signal around the time-zero peaks (c) Zoomed in time scans around minimum DT/T signals. All three figures share the same figure legend. Dashed lines mark where the DT/T signal level is zero. (d) The pump power dependent of the minimum DT/T signal level. All the data in these figure is taken with 250 kHz repetition rate.

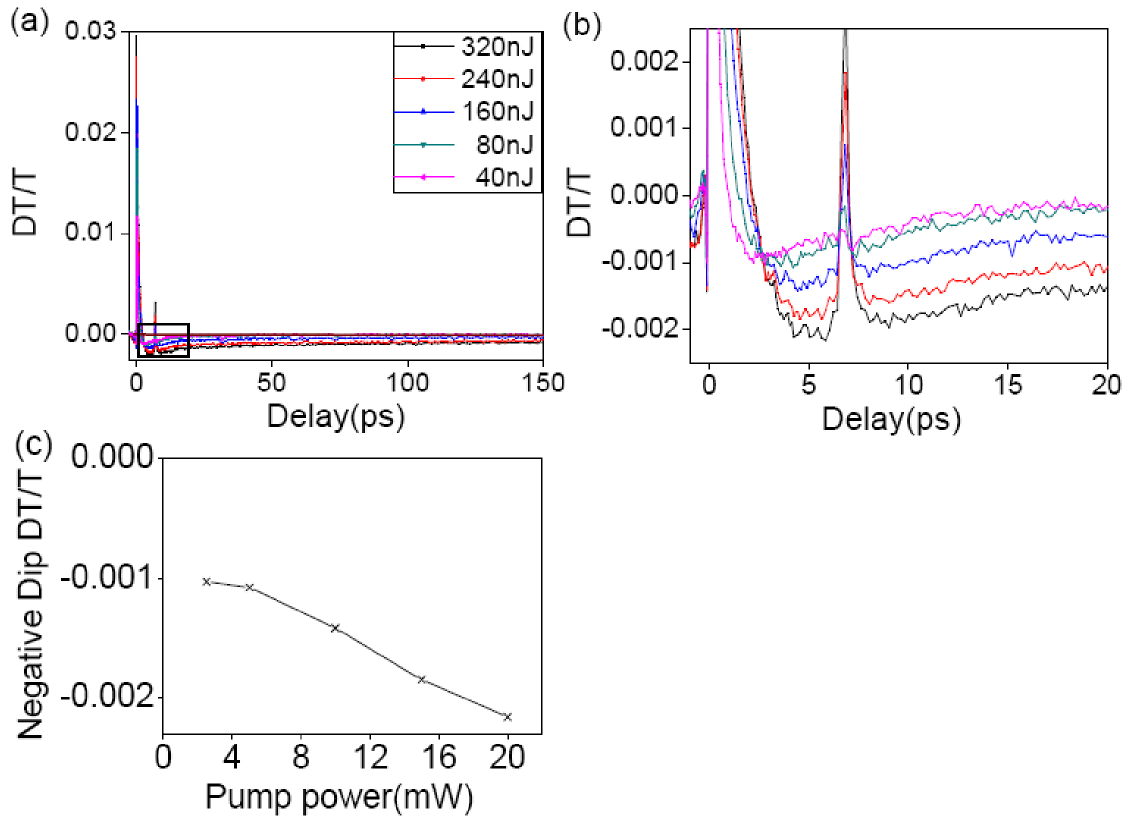

Figure 4.18: High Pump Power Dependence (a) Full DT/T time scans taken at 10K with 800nm pump power of 40 nJ, 80 nJ, 160 nJ, 240 nJ and 320 nJ. The probe wavelength is 1.88 μm which corresponds to a transition below the Fermi level of a doped layer. The part in a rectangle is zoomed and shown in Fig. (b). A dash line marks where the DT signal is zero (I can't even see the dashed line). Both figures share the same legend. (b) Zoomed in time scans around DT/T minima at different pump powers. (c) Pump power dependence at a minimum DT/T signal level. All the data in figures is taken with 62.5 kHz repetition rate.

4.6.3 Experimental Fitting at Low Pump Excitation

At low pump excitation, constant minimum DT/T can be used as a good reference to normalize simulated DT/T with the experimental results, so that we can extract the exact electron temperature at various time delays from the simulation. To fit the electron-phonon coupling dynamics, we use the same two quasi-temperature models in reference [37] that is described in Sec. 4.5. The result is shown in Fig. 4.19. The simulation has been carried out prior to knowing the precise doping profile. Thus the one heavily doped layer has been used as a model for the simulation. From Fig. 4.15, we know that this simulation doesn't actually

match the electron temperature when it is higher than 500K. So the result here related to high temperature behavior is not accurate. The updated results from this simulation are being generated as this dissertation is being written.

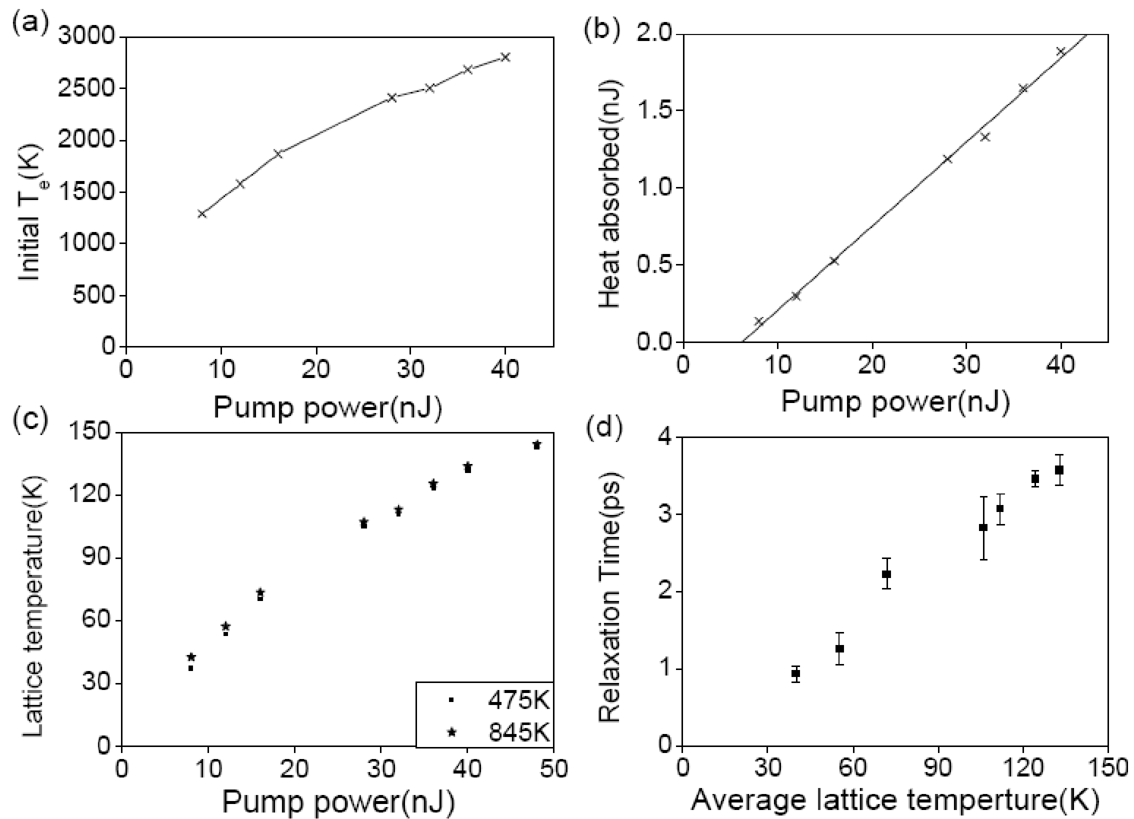

Figure 4.19: Low Pump Power Dependentce Analysis (a) Peak electron temperature at different 800nm pump power excitations at lattice temperature of 10K. (b) The energy absorbed by the sample at different pump power excitations. (c) Lattice temperature when electrons temperature relaxes to 845K (star) and 475K (rectangular) respectively. (d) The relaxation time from electron temperature of 845K to 475K at different lattice temperatures. All the results are extracted from the experimental data shown in Fig. 4.17.

The electron heat capacity of doped and undoped graphene layers are deducted in Appendix A. For the lattice heat capacity, we use the value in reference [41]. The electron temperature of DT/T peaks at different pump energies as shown in Fig. 4.19 (a). From the electrons' heat capacity, the heat absorbed by the sample at different excitation energies can be calculated. This is shown in Fig. 4.19 (b). Data points are fitted very well using a straight line whose slope is about 5% which corresponds to the pump absorption efficiency. This is much lower

than the well known 2.3% absorption coefficient of each layer, the reason for this huge discrepancy is due to the ignorance of the other doped layers.

There are two special points in a DT/T time scan: they are zero cross points and minimum DT/T points which corresponds to electron temperatures of 845K and 475K (this is different from Fig. 4.15, since 3 lightly doped layers are not included in this simulation) respectively. For different pump energies, the relaxation times from 845K to 475K are different which infers the hot phonon effect. Assuming an electron temperature relaxes through transferring heat to the lattices only, we can obtain lattice temperatures at 845 K and 475 K as shown in Fig. 4.19 (c). Due to a relatively much larger lattice heat capacity, the lattice temperature is almost constant during this relaxation process. Fig. 4.19 (d) shows that the relaxation from 845 K to 475 K gets slower with increasing phonon temperature, which is an indication of hot phonon effect.

In conclusion, electron and lattice temperatures at various time delays can be extracted from power-dependent data. The electron-phonon coupling slows down with increasing phonon temperature which indicates a hot phonon effect.

4.7 Probing the New Electromagnetic Mode in Graphene

Isotropic and uniform three-dimensional plasmas can support both longitudinal and transverse electromagnetic modes. However, in conventional 2D electron gas, only the longitudinal modes may exist under standard experimental conditions. This is due to the fact that the imaginary part of the conductivity is always positive in conventionals 2D electron gas system such as GaAs/AlGaAs quantum-well structures. This system can only support TM modes [42]. TE modes can propagate only when the imaginary part of conductivity is negative [43]. Due to an unique band structure of graphene, theoretical calculation by S. A.

Mikhailov and K. Ziegler [16] shows that in the frequency window of $1.667 < \Omega < 2$,where $\Omega = \hbar\omega / \mu$, $\mathrm{Im}\,\sigma(\omega) < 0$, which means that TE modes can be supported in this frequency range. According to reference [16], at a finite electron temperature, a TE mode acquires a finite damping due to the real part of conductivity at a finite temperature, however, this damping is very small with high doping level. With electron temperature $T_e = 0.1\mu$, this effect is still very small. Considering an electron density of the most heavily doped layer in #598, the Fermi energy corresponds to $T \simeq 4000K$, so that TE mode should be easily observable at room temperature.

To couple a mid-infrared beam into the TE mode of graphene, special dispersion relationship have to be satisfied and this is given by the equation (8) in reference [16]:

$$\sqrt{Q^2 - \Omega^2} = \frac{g_s g_v}{4} \frac{e^2}{\hbar c} \left(\frac{\Omega}{2} In \frac{2+\Omega}{2-\Omega} - 2 \right), \tag{4.6}$$

where Q is a normalized wavevector, $Q = \hbar cq / \mu$. Since the factor $\alpha = \frac{e^2}{\hbar c}$ is very small, the deviation of the wave vector from frequency Ω is very small, which means that the TE mode propagates laterally with the velocity close to the velocity of light. Thus this dispersion curve is very closed to $\omega \le cq$. So if a prism is used to couple an evanescent wave into this mode, the coupling angle is slightly below the critical total reflection angle.

The sample used in this experiment is #598; the Fermi level of the most heavily doped layer is measured to be 350 meV above the Dirac point. From the frequency windows, the TE mode support: $1.667 < \Omega < 2$, meaning the coupling wavelength needs to be between 1.77 μm and 2.1 μm.

The experimental setup is shown in Fig. 4.20. It's a pump-probe setup similar to the one used in the previous sections, except that a BK7 prism is used to couple a probe pulse to graphene.

The probe beam is s-polarized; its infrared spectrum is fixed in the frequency windows that support the TE-mode. The incident angle of the probe beam is tuned right below the critical total reflection angle in a BK7 prism as shown. An 800 nm pump pulse arrives before the probe pulse to change the electron temperature and thus the Fermi level in the sample, so that only after a certain time delay, the Fermi level and the electron temperature can satisfy the right condition to support a TE mode which is indicated as a reflection dip in a DR time scan due to the coupling of the probe pulse into the supported TE mode. The experiment is not successful due to either misalignment or the approximations made in the theory. Further improvement on the experiment setup or more detail theoretical work is needed in this direction.

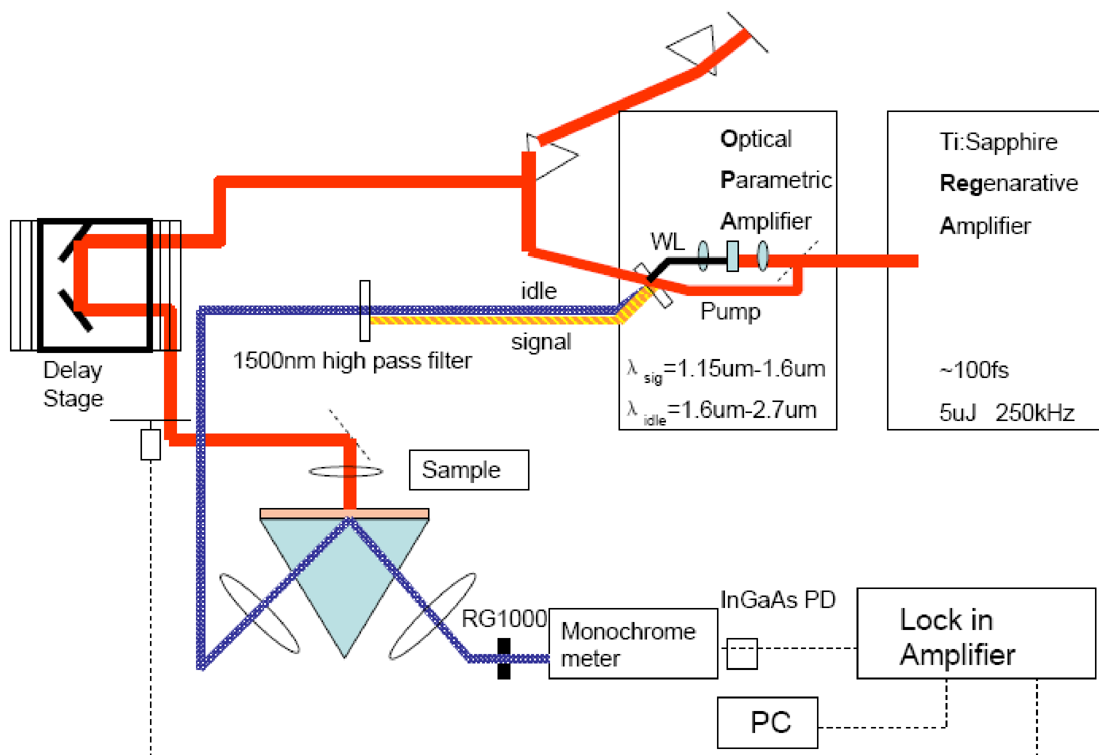

Figure 4.20 Experimental Setup for Probing TE Mode.

References

[1] C. Berger *et al.*, J. Phys. Chem. B 108, 19912 (2004).

[2] C. Berger *et al.*, Science 312, 1191 (2006).

[3] K. S. Novoselov *et al.*, Nature 438, 197 (2005).

[4] K. S. Novoselov *et al.*, Science 306, 666 (2004).

[5] Y. Zhang *et al.*, Nature 438, 201 (2005).

[6] J. Shah, Boston: Academic Press (1992).

[7] W. A. de Heer *et al.*, Solid State Communications 143, 92 (2007).

[8] M. L. Sadowski *et al.*, Solid State Communications 143, 123 (2007).

[9] M. L. Sadowski *et al.*, Physical Review Letters 97, 266405 (2006).

[10] A. Mattausch, and O. Pankratov, Physical Review Letters 99, 076802 (2007).

[11] F. Varchon *et al.*, Physical Review Letters 99, 126805 (2007).

[12] G. M. Rutter *et al.*, Science 317, 219 (2007).

[13] T. Ohta *et al.*, Science 313, 951 (2006).

[14] S. Y. Zhou *et al.*, Nat Phys 2, 595 (2006).

[15] H. Kalt *et al.*, Physical Review B 40, 12017 (1989).

[16] S. A. Mikhailov, and K. Ziegler, Physical Review Letters 99, 016803 (2007).

[17] G. W. Semenoff, Physical Review Letters 53, 2449 (1984).

[18] J. Martin *et al.*, Nat Phys 4, 144 (2008).

[19] J. Hass *et al.*, Physical Review Letters 100, 125504 (2008).

[20] P. Darancet *et al.*, Physical Review Letters 101, 116806 (2008).

[21] C. Faugeras *et al.*, Applied Physics Letters 92, 011914 (2008).

[22] P. B. Visscher, and L. M. Falicov, Physical Review B 3, 2541 LP (1971).

[23] L. Pietronero *et al.*, Physical Review Letters 41, 763 (1978).

[24] D. P. DiVincenzo, and E. J. Mele, Physical Review B 29, 1685 (1984).

[25] D. A. Dahl, Physical Review B 37, 6882 (1988).

[26] X. Wu *et al.*, Physical Review Letters 98, 136801 (2007).

[27] F. Guinea, Physical Review B 75, 235433 (2007).

[28] J. M. B. L. d. Santos, N. M. R. Peres, and A. H. C. Neto, Physical Review Letters 99, 256802 (2007).

[29] S. Shallcross, S. Sharma, and O. A. Pankratov, Journal of Physics: Condensed Matter, 454224 (2008).

[30] C. Berger *et al.*, Science, 1125925 (2006).

[31] M. L. Sadowski *et al.*, Solid State Communications 143, 123 (2007).

[32] T. Ohta *et al.*, Physical Review Letters 98, 206802 (2007).

[33] H. Miyazaki *et al.*, Applied Physics Express 1, 034007 (2008).

[34] J. Martin *et al.*, 4, 144 (2008).

[35] J. Hass *et al.*, Physical Review B 78, 205424 (2008).

[36] S. Fratini, and F. Guinea, Physical Review B 77, 195415 (2008).

[37] H. E. Elsayed-Ali *et al.*, Physical Review Letters 58, 1212 (1987).

[38] S. Butscher *et al.*, Applied Physics Letters 91, 203103 (2007).

[39] R. Bristritzer, and A. H. MacDonald, arXiv:0901.4159v2 (2009).

[40] K. I. Bolotin *et al.*, Physical Review Letters 101, 096802 (2008).

[41] C. Masarapu, L. L. Henry, and B. Wei, Nanotechnology, 1490 (2005).

[42] F. Stern, Physical Review Letters 18, 546 (1967).

[43] V. I. Fal'ko, and D. E. Khmel'nitskii, Zh. Eksp. Teor. Fiz. 95, 1988 (1989).

Chapter V

Coherently Controlled Photocurrent in Epitaxial Graphene

5.1 Introduction

Usually optical beam can't generate photocurrent, since the generated photo-carriers have equal probability in moving in all directions, thus cancelling each other and give no net current. However, by using two phase related beams, directional photocurrent can be generated and controlled by the relative phase between the two beams. This optical coherent control process can be understood in terms of interference between two or more optical fields coupled to the same initial and final states of a system as shown in Fig 5.1. Interference between transition amplitudes can occur because an electron in the lower level can reach the upper level via two pathways. By controlling the relative phase of the beams, the overall transition rate can be modified. In semiconductor, the quantum mechanical interference between pathways coupling the same initial valence state and final conduction state leads to an optically induced asymmetrical distribution of free carriers in momentum space. That's the overall rate of interband transitions induced by simultaneous one and two photon. Excitation can be different for two states with anti-parallel wavevectors. The resulting anisotropic distribution of carriers in the conduction band creates a net current flow that can be controlled by adjusting the relative phase of the beams. This phenomenon can also be understood in terms of phase interference of the electron wave-function. Electrons are excited

by single- or two- photon transitions to states of different parity. These symmetric and antisymmetric wave-functions can in turn interfere constructively in one spatial direction and destructively in the other direction depending on the optical phase.

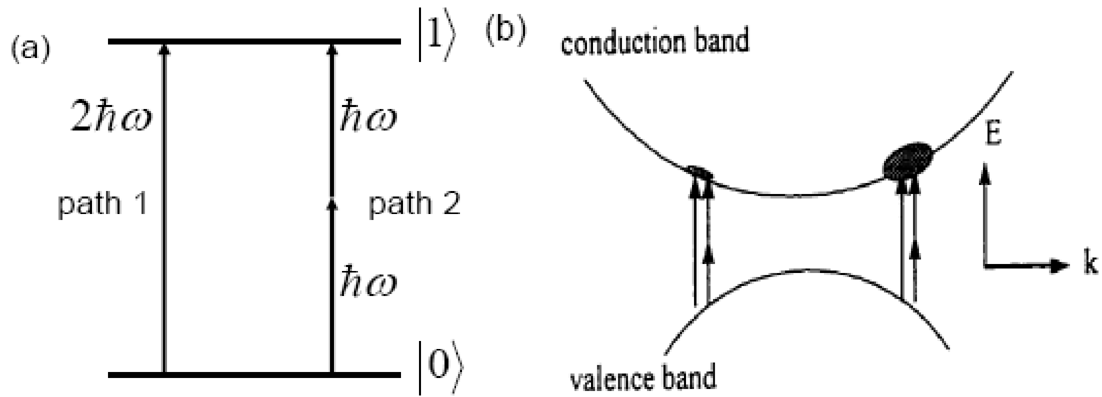

Figure 5.1: Schematic Diagram of General Coherent Control. (a) Schematic diagram of electron eigenstates coupled by electric fields at frequencies ω and 2ω between two discrete energy levels. (b) Schematic band diagram of a bulk semiconductor with electrons excited into preferential states in momentum-space. The resulting distribution of carriers creates a net current flow. Figure is taken from Ref. [1].

Optical coherent control has been demonstrated in discrete energy level systems, such as atomic media [2], Xenon gas [3, 4], mercury [5] and atomic gases such as Krypton [6], Rubidium [7] and Barium [8] as early as 1960s. Later, this effect has been exploited in molecules with the intention of manipulating chemical reactions [9-15]. Coherent control effect in solids, especially in semiconductor has once been speculated as not observable in experiment due to the continuum of the available states in conduction and valance bands and the short electronic dephasing time associated with them. Later it is shown by first principle theoretical calculations, that coherent control using interband transitions in bulk semiconductors can also yield controllable photocurrents even though both the initial and final states lie in the continuum [16]. Shortly thereafter optical coherent control has been shown to induce electrical currents in bulk GaAs [17], and later in quantum well materials [18] and carbon nanotubes [19]. These are three dimensional (3-D), two dimensional (2-D)

and one dimensional (1-D) semiconductors. Optical coherent control in indirect bandgap semiconductor like silicon has also been demonstrated experimentally recently using THz detection technique [20].

Although coherent controlled photocurrent has been demonstrated in various materials, similar experiments in epitaxial graphene are still of great interest for the following reasons: first, due to its high symmetry of the graphene sheet, the direction of injected current can be controlled by relative polarizations of the incident fields [21]; second, quantitative studies of the magnitude of the effect can be very useful as a probe of the scattering processes which control the dynamics of hot photoexcited carriers in these systems; third, this method provides means for current injection without electrical contacts.

5.2 Tight Binding Calculation

Calculation of the optical injection and coherent control in graphene through tight-binding approach has been done separately in collaboration with Julien Rioux et. al. [22] and E. J. Mele et al [21]. Here we summarize relevant theoretical results from Julien Rioux and John Sipe's work.

5.2.1 Current Injection Rate

Assuming a simple-parameter effective Hamiltonian:

$$H_{eff} -> v_F \begin{pmatrix} 0 & \hbar k_- \\ \hbar k_+ & 0 \end{pmatrix}, \tag{5.1}$$

where $k_\pm = k_x \pm ik_y$. v_F is the Fermi velocity, and a linear energy bands: $E(\mathbf{k}) = \pm v_F \hbar k$. The carrier injection rate for one-photon absorption $\overline{\xi_1}(2\omega)$ and two-photon absorption $\overline{\xi_2}(\omega)$ in rate equation $\dot{n}_1 = \xi_1^{ab}(2\omega)E_{2\omega}^{a*}E_{2\omega}^{b*}$ and $\dot{n}_2 = \xi_2^{abcd}(\omega)E_\omega^{a*}E_\omega^{b}E_\omega^{c*}E_\omega^{d}$ can be calculated following Fermi's golden rule to be:

$$\overline{\xi_1}(2\omega) = g_s g_v \frac{e^2}{8\hbar}(2\hbar\omega)^{-1} \ , \tag{5.2}$$

$$\overline{\xi_2}(\omega) = g_s g_v 8\hbar e^4 v_F^2 (2\hbar\omega)^{-5} , \tag{5.3}$$

where g_s and g_v are spin and valley degeneracy.

The one photon absorption process has no polarization dependence, however, the two photon absorption process does. Consider a general field $E_\omega = \frac{1}{\sqrt{2}} E_\omega(\hat{x}' + \hat{y}' e^{i\delta\phi})$, with the primed unit vector denoting any two perpendicular directions, the two-photon absorption rate is:

$$\dot{n}_2 = \xi_2(\omega) | E_\omega |^4 \ (1 + \sin^2(\delta\phi)) . \tag{5.4}$$

So circular polarization provides twice the two-photon absorption compared to linearly polarized light.

5.2.2 Tensor Element

The current injection due to interferences of one- and two-photon absorption is a third order nonlinear process. The corresponding tensor of graphene evaluated within the tight-binding model has a single independent component:

$$\eta_I^{xxxx} = \eta_I^{xyxy} = \eta_I^{xxyy} = -\eta_I^{xyyx} \equiv \overline{\eta}_I , \tag{5.5}$$

and

$$\overline{\eta}_I(\omega) = i g_s g_v e^4 v_F^2 (2\hbar\omega)^{-3} , \tag{5.6}$$

The current density generation rate associated with interference between single and two photon absorption processes of beams at 2ω and ω is of the form:

$$\dot{\mathbf{J}} = \overleftrightarrow{\eta} : \mathbf{E}^{\omega}\mathbf{E}^{\omega}\mathbf{E}^{2\omega} \sin(2\phi_\omega - \phi_{2\omega}) , \tag{5.7}$$

where $\mathbf{E}^{\omega,2\omega}$ and $\phi_{\omega,2\omega}$ are the optical fields and phases, and $\overleftrightarrow{\eta}$ is a fourth rank current injection tensor whose symmetry properties are governed by the illuminated material.

5.2.3Polarization Effect

Due to the symmetry of graphene and all its tensor elements are equal to each other as shown in Eq. (5.5), the coherently controlled current direction has some special polarization dependence and thus can be controlled by the polarization of the fundamental beam and its second harmonic. If both beams are linearly polarized at normal incidence to the graphene layers, the current injection rate is:

$$\dot{J}_I = 2\,\mathrm{Im}[E_\omega^2 E_{2\omega}^*]\overline{\eta}_I(\omega)[\hat{\mathbf{e}}_{2\omega}\cos 2\theta + \hat{\mathbf{e}}_{2\omega}^{\perp}\sin 2\theta]. \tag{5.8}$$

The injected current changes its orientation depending on the angle θ which the two polarization vectors make. For collinear and cross-linear geometries, the current is parallel to the polarization of the 2ω light. The component perpendicular to the 2ω polarization direction is maximal when the polarization vectors make an angle of 45° with each other. With both beams circularly polarized with normal incidence, the rate of injection is:

$$\dot{J}_I = 2\sqrt{2}\overline{\eta}_I(\omega)(\hat{\mathbf{x}}\,\mathrm{Im}[E_\omega^2 E_{2\omega}^*] + \hat{\mathbf{y}}\,\mathrm{Re}[E_\omega^2 E_{2\omega}^*]. \tag{5.9}$$

So in this configuration, the phase difference parameter controls the direction of the current.

5.2.4 Bad Electrons

Since graphene is a zero bandgap semimetal, one-photon absorption of fundamental beam is forbidden in the doped graphene layer. However, in undoped layers the one photon absorption of fundamental beam is not forbidden if the transition is below the Fermi level as in common semiconductors as shown in Fig. 5.2. So some of the fundamental beam floods the sample with carriers those are not taking part in the interference process in those undoped layers. This is in contrast to the usual semiconductors with a nonzero bandgap, where ω and 2ω can be adjusted so there is no one-photon absorption. These carriers have no net velocity,

they scatter and break the phase relationship when the directional “good” electrons are injected by quantum interference, thus the term “bad” electrons.

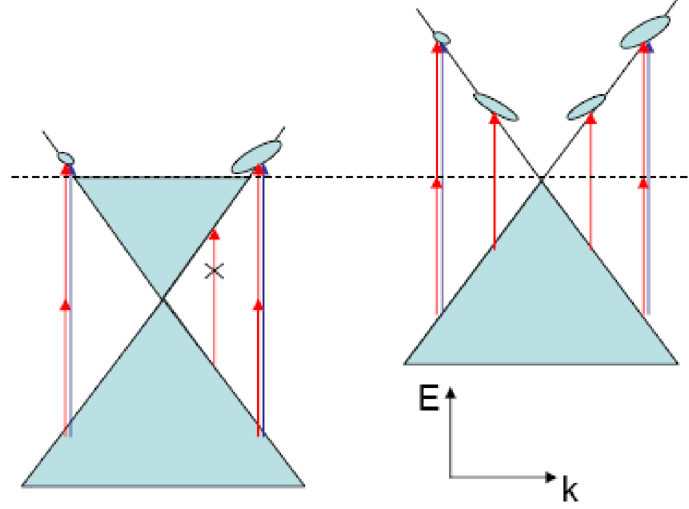

Figure 5.2: Schematic Diagram of Coherent Contol in Epitaxial Graphene. Red is associated with the ω beam, blue with the 2ω beam. Asymmetric electron populations at $\pm k$ and hence current generation, is indicated by shaded patches. The dash line goes across the Fermi level of doped and undoped graphene layers.

If we define a swarm velocity by:

$$v_{swarm}(\omega) \equiv \frac{\dot{J}_I}{e\dot{n}} = \frac{e^{-1}\vec{\eta}_I(\omega)}{x\overleftrightarrow{\xi}_1(2\omega) + x^{-1}\overleftrightarrow{\xi}_2(\omega)}, \tag{5.10}$$

where $x = \frac{|E_{2\omega}|}{|E_\omega|^2}$. The velocity per carrier is maximized by balancing one- and two-photon absorption process in the denominator of the above expression, which gives $v_{\max}(\omega) = v_F$, this maximal velocity is independent of the excitation frequency, due to linearity in the graphene bands. The work of Julien Rioux and John Sipe shows that when the injection rates of “good” and “bad” electrons are balanced, the overall swarm velocity is reduced by 2/3 compared to the optimal case.

5.3 Dynamics of Injected Coherent Control Current

Here we qualitatively discuss how the various scattering processes are going to affect the injected coherent controlled current. These effects include carrier, phonon, impurity and defect processes and space charge relaxation. We see that current decay time in graphene are longer compared to common semiconductor like GaAs due to its unique Dirac Fermion properties.

Carrier-carrier scattering rate is measured to be below 100 fs in Chapter IV. Elastic scattering between e-e and h-h doesn't affect injected current in graphene. However, elastic scattering between electrons and holes does, due to different effective masses in common semiconductors. However, this is not the case in graphene, electrons and holes are both massless in graphene and elastic e-h scattering doesn't cause current decay.

Inelastic scattering time with optical phonons is measured to be on the order of ps from Chapter IV. The phonon scattering process in graphene is different from those in common semiconductor. In semiconductor, the relaxation from high energy to lower energy in the parabolic band decreases the electron velocity; this is not the case in graphene due to graphene's linear energy dispersion curve as long as the scattering process doesn't flip the sign of the carrier velocity. However, in case the phonon scattering flips the sign of carrier velocity, current relaxes. Inelastic scattering with long length scale disorder is suppressed in graphene due to the conservation of the pseudospin freedom. The suppressing of this kind of backscattering is unique in graphene materials which increases the current decay time. However this doesn't apply to the short length scale disorder [23].

The space charge effect in quantum wells has been discussed extensively by W. Sha et al. in Ref [24]. The time scale of space charge effect is determined by the dielectric relaxation time

in graphene. The dielectric relaxation time t_d can be estimated from the Debye length L_{Db} and Einstein diffusion coefficient D through the relationship $t_d = \frac{L_{Db}^2}{D}$, using the parameters in the literature, $L_{Db} \sim 1\,nm - 5\,nm$ [25, 26], and $D \sim 2.2 * 10^{-2} m^2 / s$ [27]. The dielectric relaxation time is estimated to be on the order of 1 fs. In essence, each pair of pulses at ω and 2ω incident on the sample produces a current burst: the electrons move to one side of the sample and the holes move to the other side of the sample. An internal electric field builds up due to the transient accumulation of charges. The resulting potential difference causes back drift of carriers which produce a back drift current and degrade the coherently controlled injected current. This back drift current is related to the instant conductivity of graphene layers, as a semimetal, graphene is always conductive. This is in contrast to the case in conventional semiconductor like GaAs, which becomes resistive after the recombination of the carriers. Moreover, the injection of "bad" carriers can increase the conductivity of the sample and make the space charge effect more notable.

5.4 Experiment Setup and Detection Techniques

The space charge effect is used by A. Hach *et al.* to detect coherent control injected current in low temperature grown GaAs (LT-GaAs) using current integration [17]. Two metal electrodes are fabricated on LT-GaAs to form a metal semiconductor metal device, since the generated carriers recombined quickly, LT-GaAs becomes very resistive shortly after the excitation, and the potential difference build by the space charge can accumulate and be measured by a voltmeter. Nevertheless, due to the semimetal property of graphene and the injected "bad" electrons in graphene, this detection technique doesn't apply in our experiment. An alternative way to detect the injected coherently controlled current is

measuring the radiated THz field from the sub-picoseconds burst of coherently controlled photocurrent [19, 20]. Initial effort in this direction was reported by R. W. Newson *et al.*on thin graphite samples [19], due to a very low signal level observed in graphite, they claimed that the coherently controlled THz emission was not strong enough to be detected in graphene.

5.4.1 Free Space Electro-optics Sampling of THz Field with ZnTe

Free space electro-optic sampling (EOS) with ZnTe crystal is so far the primary method to characterize freely propagating THz field in the time-domain [28, 29]. The basic working principle is based on Pockels effect or more specifically; when a THz field goes through an EO crystal like ZnTe, it modulates birefringence of this optical medium. A differential detector measures orthogonal components of the polarization of the optical probe beam to determine the THz field strength. Since Pockels effect is a non-resonant phenomenon, the polarizability of the material has temporal response on the order of a few femtoseconds which shifts the limit of the temporal resolution to the duration of the laser pulse itself. This technique allows for contact-free means of measuring the THz wave with temporal resolution limited only by pulse duration and group velocity mismatch.

A detailed experimental setup is shown in Fig. 5.3, after the 800nm optical probe beam co-propagation along with the THz wave through the ZnTe sensor crystal, a quarter-wave plate induced a $\pi/2$ phase retardation on the beam. A Wollaston prism is used to separate the orthogonal components of the polarization, which are then sent to a balanced photodiode pair for differential detection.

Here we start with the electro-optic tensor and derive the relationship between the polarization rotation of the probe beam and the THz electric field strength. The deduction

follows the routes in Ref. [28]. For crystal such as ZnTe with cubic symmetry, the electro-optic tensor is:

$$\begin{pmatrix} 0 & 0 & 0 \\ 0 & 0 & 0 \\ 0 & 0 & 0 \\ r_{41} & 0 & 0 \\ 0 & r_{41} & 0 \\ 0 & 0 & r_{41} \end{pmatrix}, \tag{5.11}$$

which yields the following equation for the index ellipsoid in the presence of a biasing field, $\mathbf{E} = (E_x, E_y, E_z)$:

$$\begin{pmatrix} 1/n^2 & r_{41}E_z & r_{41}E_y \\ r_{41}E_z & 1/n^2 & r_{41}E_x \\ r_{41}E_y & r_{41}E_x & 1/n^2 \end{pmatrix} V = \frac{1}{n'^2} V, \tag{5.12}$$

Eigenvectors $\mathbf{V}$ are the principal axes and eigenvalues n' are the principal indices in the presence of an electric field.

For a terahertz field in the <110> direction, we have $E_x = E_y = \frac{1}{\sqrt{2}} E_{THz}$, $E_z = 0$. The solution to equation (5.12) gives both the principal indices, n',

$$n_{x'} = n + \frac{1}{2} n^3 r_{41} E_{THz},\ n_{y'} = n - \frac{1}{2} n^3 r_{41} E_{THz},\ n_{z'} = n\ , \tag{5.13}$$

As well as their corresponding principal axes, $\hat{e}$,

$$\hat{e}_{x'} = \frac{1}{2}(\hat{e}_x + \hat{e}_y - \sqrt{2}\hat{e}_z),\ \hat{e}_{y'} = \frac{1}{2}(\hat{e}_x + \hat{e}_y + \sqrt{2}\hat{e}_z),\ \hat{e}_{z'} = \frac{\sqrt{2}}{2}(\hat{e}_x - \hat{e}_y)\ , \tag{5.14}$$

Just as with the terahertz field, the optical probe beam is polarized in the <110> direction. The birefringence seen by the optical beam is $n_{x'} - n_{y'} = n^3 r_{41} E_{THz}$. Thus, the phase accumulated by the optical beam after passing through a zinc telluride crystal of length L is

$$\Gamma_{ZnTe} = \frac{2\pi}{\lambda} n^3 r_{41} E_{THz} L \ , \tag{5.15}$$

The probe beam also passes through a quarter-wave plate, so the total phase from the detection system is $\Gamma = \Gamma_{ZnTe} + \pi/2$. The normalized Jones vector of the incident probe beam is $E_{in} = \begin{pmatrix} 0 \\ 1 \end{pmatrix}$. The polarization state after the system is the product of the detection system's Jones matrix with the input Jones vector:

$$E_{out} = \begin{pmatrix} \cos(\Gamma/2) & -i\sin(\Gamma/2) \\ -i\sin(\Gamma/2) & \cos(\Gamma/2) \end{pmatrix} \begin{pmatrix} 0 \\ 1 \end{pmatrix} = \begin{pmatrix} -i\sin(\Gamma/2) \\ \cos(\Gamma/2) \end{pmatrix} , \tag{5.16}$$

Independent detection of the vertical and horizontal polarization components gives the following measured intensities:

$$I_V = \cos^2(\Gamma/2) = \frac{1}{2}[1+\cos(\Gamma)] \ , \tag{5.17}$$

$$I_V = \sin^2(\Gamma/2) = \frac{1}{2}[1-\cos(\Gamma)] \ , \tag{5.18}$$

The balance detector measures the difference between the two intensities:

$$\Delta I = I_H - I_V = -\cos(\Gamma) = \sin(\frac{2\pi}{\lambda} n^3 r_{41} E_{THz} L) \approx \frac{2\pi}{\lambda} n^3 r_{41} E_{THz} L \ , \tag{5.19}$$

which gives us the desired result that the measured intensity difference is directly proportional to the terahertz electric field.

5.4.2 Experimental Setup

For our experiment, a commercial 250 kHz Ti: sapphire oscillator/amplifier operating at 800nm is used to pump an optical parametric amplifier (OPA) to generate 1.2 μm-1.6 μm signal and 1.6 μm-2.4 μm idle light. The signal and idle beams from the OPA are used to pump a differential frequency generator (DFG) to generate 2-4 mW of 3.2 μm or 4.8μm (ω

beam) with 220 fs pulse width. ω beam passes through a $AgGeS_2$ (for 3.2μm) or $ZnGeP_2$ (for 4.8 μm) crystal (type I) to generate 1.6 μm or 2.4μm (2ω beam). The $AgGeS_2$ crystal has about 10% conversion efficiency and the conversion efficiency of the $ZnGeP_2$ is expected to be even higher according to the manufacturer. Then ω/2ω pulses pass through a CaF_2 plate with tunable tilt angle to adjust the relative phase. All the optics after the second harmonic crystal are reflection optics with λ/10 flatness generally to minimize the phase front distortion. The two emerging pump beams are cross polarized and overlapped on the samples with a 15 μm diameter spot size as measured using 10-90 percent power method with a razor blade. The two pump beams produce peak focus irradiation intensities for the 3.2 μm and 1.6 μm beams of 2.8 GW/cm^{-2} and 0.45 GW/ cm^{-2} on the sample after the loss of all intermediate optics. A high-density polyethylene (HDPE) plate which has 90% transmission to THz is used to block the transmitted Mid-IR beam which can give optical rectification generated THz signal on ZeTe crystal. The emitted terahertz radiation is measured by electro-optic sampling, whereby a weak probe pulse from the Ti: sapphire oscillator at 800nm is temporally scanned through the terahertz pulse in a 1 mm thick (110)-oriented ZnTe crystal. Because of phase mismatch between the terahertz and the probe beams, the effective bandwidth of the electro-optic detection system is estimated to be ~2 THz. An optional beam path is an 800nm prepulse focused to a 120 μm spots on the sample with 45° incident angle to excited background hot carriers with tunable power and relative delay before the arrival of the ω/2ω pulses.

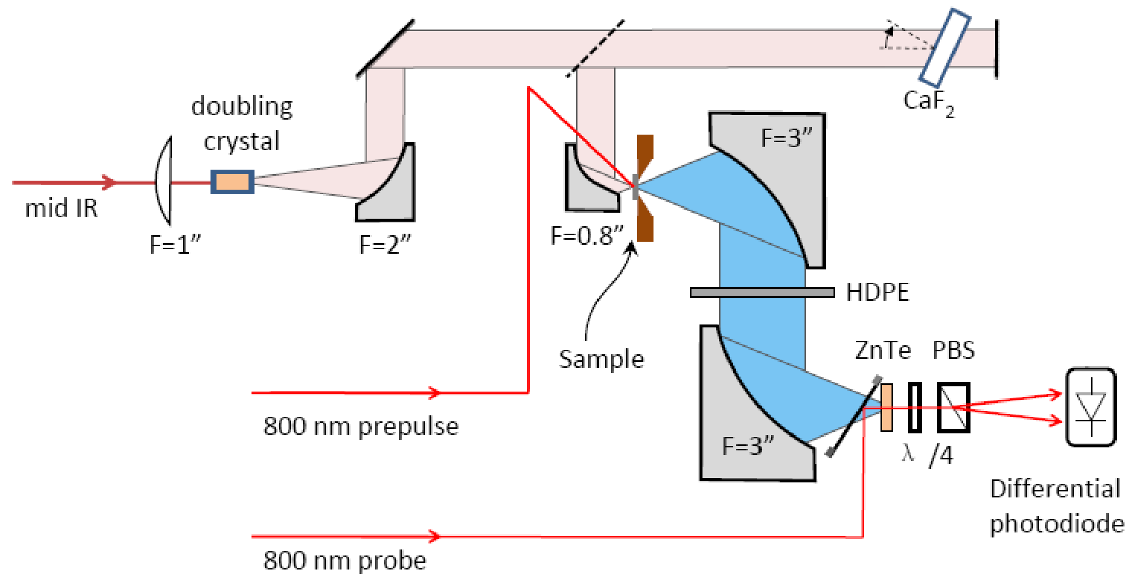

Figure 5.3: Experimental Setup for Coherent Control Experiment with Pre-pulse Excitation of Background Hot Carriers.

The samples are ultrathin epitaxial graphene films produced on the C-terminated face of single-crystal 4H-SiC by thermal desorption of Si. Four different samples with different thicknesses are used in this experiment: #8B2 (9 layers), #1104 (13 layers), #1133 (35 layers) and #7J8 (63 layers). The major experimental data shown in this thesis is on the sample (#7J8) unless otherwise specified. The doping profile of the sample (#7J8) has been determined from the pump-probe experiment in Chapter IV. The first few layers are heavily doped and the doping intensity decreases to zero gradually. The Fermi levels of the first four doped layers are measured to be about 365 meV, 220 meV, 140 meV, 93 meV above the Dirac point, respectively. From the pseudopotential simulation, both the two photon absorption and one photon absorption rate increase with longer excitation wavelength which means higher injection efficiency at lower photon energy. As shown in Fig. 5.1(a) the pump wavelength is selected right above the Fermi level of the most heavily doped layer. One-photon absorption

of ω beam is not allowed in this doped layer due to Pauli blocking, however this process would inject 'uncontrolled' carriers with no net velocity in undoped layers.

5.5 Experiment Results and Discussion

5.5.1 Coherent Controlled Photocurrent in Epitaxial Graphene

Figure 5.4 (a) shows the THz field as a function of time delay between 3.2 μm/1.6 μm pump pulses and an electro-optic sampling 800 nm probe pulse; traces are shown for values of $\Delta\Phi$ separated by π. The oscillatory structure reflects the narrow bandwidth of the electro-optic detection system. As shown in Fig. 5.4 (a), the THz field reverses sign when $\Delta\Phi$ changes by π which is consistent with a coherence-induced current source. The current amplitude and scalar direction can be controlled through the phase parameter, $\Delta\Phi$ alone. The current vector can also be controlled by redirecting the beam polarization.

Figure 5.4 (b) shows the contour plot of the terahertz radiation field from epitaxial graphene as a function of $\Delta\Phi=2\Phi_{\omega}-\Phi_{2\omega}$ and the time delay between the 3.2 μm/1.6μm pump pulses and 800 nm probe beam. A typical terahertz pulse trace as a function of the probe pulse time delay with constant $\Delta\Phi$ is shown in the top panel corresponding to the horizontal dashed line on the contour plot. The main emission peak at time zero is followed by weaker oscillatory trace (only partial shown in Fig. 5.4 (b)). This oscillatory behavior reflects the limited bandwidth of the terahertz detection scheme rather than the intrinsic temporal behavior of the current. Specifically, charge displacement is expected to rise with the 220 fs pulse and decay through the development of space-charge fields and carrier momentum relaxation. The right panel shows the dependence of the terahertz field with $\Delta\Phi$ for constant pump/probe delay. The current reverse direction as the phase varies and more generally follows a $\sin(\Delta\Phi)$ dependence, consistent with the coherently controlled photocurrent description of Eq. (5.7).

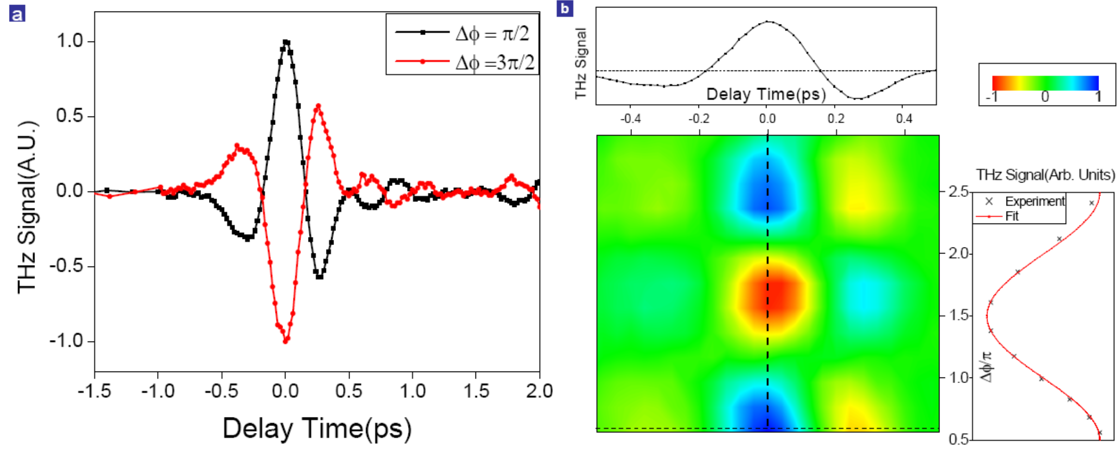

Figure 5.4: Phase Controlled THz Emission from Injected Photocurrent. a, Time-dependent electro-optic signals of THz fields from epitaxial graphene for different values of ΔΦ. b.Time-dependent terahertz radiation field from epitaxial graphene as a function of time delay between 3.2 μm/1.6 μm pump and 800nm probe pulse and the phase parameter, ΔΦ, between cross polarized pump beams. Top panel: terahertz trace time delay dependence for constant ΔΦ represent by the horizontal dashed line on the contour plot. Right panel: terahertz field ΔΦ dependence for constant time delay represented by the vertical dashed line on the contour plot.

5.5.2 THz Signal Strength

Preliminary experiment of coherent control in bulk graphite has been performed by R. W. Newson et al. using 1.4 μm /0.7μm beam [19]. Due to the very weakly emitted THz signal observed in bulk graphite, they stated that "*given graphite's absorption depth and our signal-to-noise ratio, we do not expect to observe current injection in graphene samples with the present experimental configuration (barring any enhancement effects in the atomically thin films), since the signal from graphene is expected to be about 2 orders of magnitude weaker.*"

With the same THz detection techniques, the coherent controlled THz signal from epitaxial graphene can be observed in our experiment for the following reasons: first, we are using lower energy photon, which has much larger two-photon absorption efficiency according to Eq. (5.3). Second, the epitaxial graphene sample used in this experiment has multiple layers and each layer behaves like single layer graphene which can enhance the signal magnitude.

The details of the contribution of graphene multiple layers are going to be discussed later. Third, benefitting from the high transmission coefficiency of SiC at THz, a transmission scheme is used in our experiment which easily achieves higher THz collection efficiency comparing to the reflection scheme that has been used in the previous work [19, 20].

To estimate the signal level of peak THz field from epitaxial graphene sample, we replace the epitaxial graphene sample with a 100 μm thick (110) oriented ZnTe crystal and keep all the other experimental conditions the same. The s-polarized 220 ps 3.2 μm mid-IR beam generates THz in the ZnTe crystal due to the optical rectification effect [28] and is used as a reference for the coherent control signal. The peak amplitude level of the THz from the coherent controlled signal with 3.2 μm/1.6 μm beam on sample #7J8 is about the same as the optical rectification THz signal from ZnTe crystal.

5.5.3 Polarization of the Emitted THz

To determine the relationship between the ejected current direction and ω/2ω pump polarization, we measure the polarization of the emitted THz field. For this purpose, we put a THz polarizer with known polarization axis between the two collection parabolas after the sample as shown in Fig 5.3. The polarization of the emitted THz field is measured by rotating the THz polarizer to measure the THz field after the polarizer. The fundamental beam from the DFG is horizontally polarized and polarization of the second harmonic generated 2ω is perpendicular to the fundamental polarization in type I phase matching condition. From Eq. 5.10, the injected current direction is predicted to be the same as 2ω polarization which is vertical in this configuration.

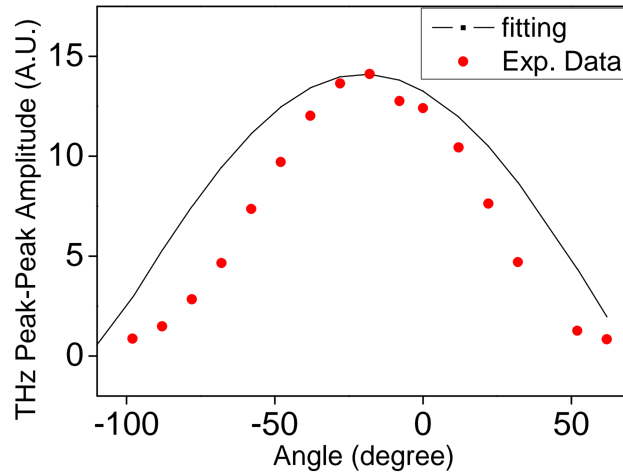

Figure 5.5: THz Field *vs* Polarizer Orientation. The x-axis is the angle between the polarization direction of THz polarizer and the vertical direction. The y-axis is the THz field peak to peak amplitude. The data is fitted by sinusoidal curve.

The experimental data is shown in Fig. 5.5; the peak amplitude is off by 20 degree from the theoretical prediction, the 20 degree discrepancy can be due to the following factors: first, the fundamental beam polarization is supposed to be horizontal, but it can be some small angle off after several reflection optics. Second, the second harmonic polarization can be a small angle off from the perpendicular direction due to non-ideal phase matching orientation of the second harmonic crystal. Third, the discrepancy partly comes from the deviation of the ZnTe crystal orientation from the optimum direction for vertical polarized THz direction. The ZnTe crystal orientation is fixed during the experiment, when the polarizer projects the THz signal to different directions, the ZnTe crystal is no longer at corresponding optimum detection orientation, so the detected THz field is smaller than those prediction from a sinusoid fitting, which explains the deviation of the shape of the experimental curve from the sinusoidal fitting curve.

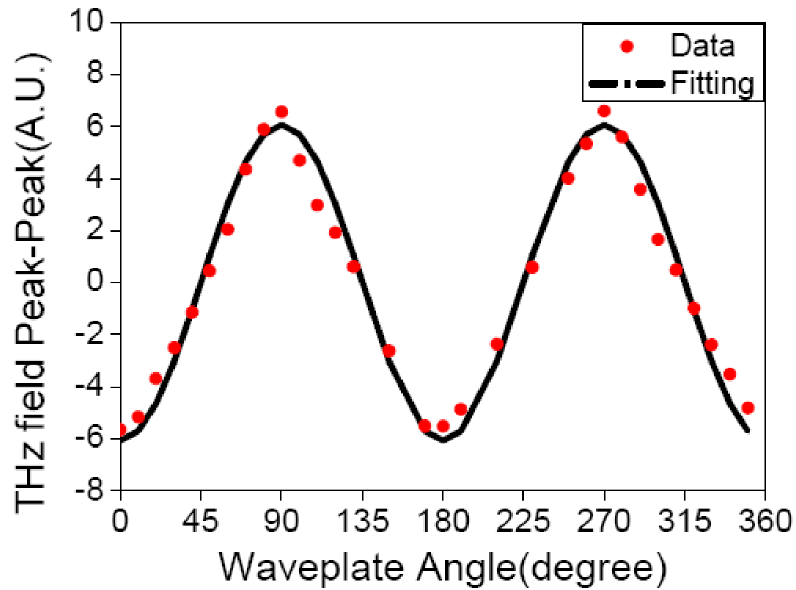

Figure 5.6: THz Field *vs* Wave Plate Main Axis Orientation. The x-axis is the angle between the main axis of the 3.2 µm half waveplate and the horizontal direction of THz polarizer and the vertical direction. The y-axis is the THz filed peak to peak amplitude. The data is fitted by sinusoidal curve.

We fix the THz polarizer orientation and use a half wave plate to rotate the fundamental beam polarization. This is done to circumvent the complex correction due to the non optimum ZnTe crystal orientation with respect to the changing THz polarization, The second harmonic crystal is rotated following the half wave plate to optimize the second harmonic generation. In this way, the polarization of the generated second harmonic beam is always orthogonal to the polarization of the fundamental beam. If the theoretical calculation is valid, the coherently controlled generated current direction and thus the THz polarization follows the polarization of the second harmonic beam, after projecting on a fix THz polarizer. The transmitted THz field follows a cosinusoidal curve.

Figure 5.6 shows peak-peak THz field amplitude as a function of wave plate rotational angle. This experiment is performed with 3.2µm/1.6µm beam. The x-axis is the angle between the main axis of the 3.2 µm half wave plate and the vertical direction (orthogonal to the

polarization of the fundamental beam), the polarization of the 3.2 μm signal is rotated twice of this angle. The THz polarizer is aligned so that the detected THz is maximized when the waveplate rotational angle is at 90 degree. Instead of using main peak amplitude as shown in Fig. 5.4 (a), we use the peak-peak THz field amplitude difference between the main positive peak and the main negative peak amplitude as shown in the y-axis. In this way, we can get rid of possible constant negative or positive background which adds error to the result. The experimental data shown in Fig. 5.6 follows the sinusoidal fitting very well which verifies that THz polarization and the current direction is fully controlled by the fundamental beam polarization and has nothing to do with the graphene crystal orientation which coincides with the theory.

5.5.4 Fundamental Beam Power Dependence

To verify the nonlinear dependence of the coherent control signal on the beam power, the peak THz field amplitude is measured as a function of the fundamental beam average power P_ω before the doubling crystal. A separate measurement of the peak THz field amplitude as a function of second harmonic beam power is not available due to the copropagating experiment configuration; there is no good way to change the power of the second harmonic beam while keeping the fundamental beam power and all other experimental conditions the same in the copropagating setup. From a simple analysis, one can expect the fundamental beam power dependence to be quadratic: from Eq. (5.7), the injected current change rate satisfies the following relationship: $\dot{\mathbf{J}} \propto \mathbf{E}_\omega \mathbf{E}_\omega \mathbf{E}_{2\omega}$. In a second harmonic process: $\mathbf{E}_{2\omega} \propto \mathbf{E}_\omega^2$, so $\dot{\mathbf{J}} \propto \mathbf{E}_\omega^4 \propto P_\omega^2$, where P_ω is the power of the fundamental beam, since the emitted THz field $E_{THz} \propto \dot{J}$, it is proportional to P_ω with a power law of 2: $E_{THz} \propto P_\omega^2$.

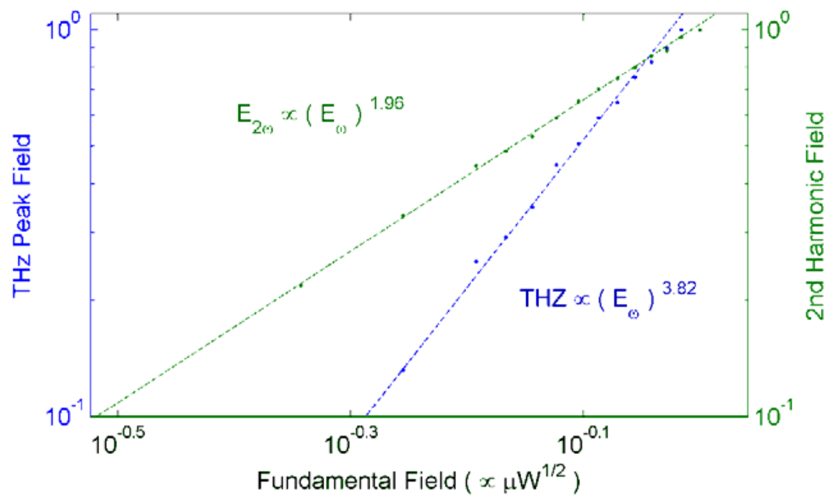

Figure 5.7: Fundamental Beam Power Dependence. The green line gives the dependence of the second harmonic power with respect to the fundamental beam power and the blue line gives the dependence of the generated THz peak field on the fundamental beam power. Log-Log plots are used to find the power dependent. The fundamental beam wavelength is 4.8 μm in this experiment.

For this purpose, a continuous tunable neutral density filter is used to attenuate the OPA signal and idle power to change the mid-IR power from the DFG. The reason we attenuate the OPA signal instead of mid-IR power directly is simply due to the lack of a tunable mid-IR attenuator. The power law dependence is shown in Fig. 5.7. The fundamental beam used in this experiment is 4.8 μm, as fitted in the figure: the generated second harmonic power follows $E_{2\omega} \propto (E_\omega)^{1.96}$ and the generated THz field follows $E_{THz} \propto (E_\omega)^{3.82} \propto (P_\omega)^{1.91}$. It's not possible at this point to determine whether the slight disagreement between theory and experiment comes from additional physical effects not included in the model. However, the power dependent data is very good and coincides with the theoretical prediction. The small deviation can be due to increasing space charge effect with increasing power, bad electrons effect, etc…

5.5.5 Second Harmonic Beam Power Dependence

To independently tune the second harmonic beam power without changing the power of the fundamental beam power is not convenient due to the limitation of the setup. However, this can be accomplished by mismatching the second harmonic generation crystal phase matching angle to change the second harmonic generation efficiency. Again a THz polarizer is inserted between the two collecting parabolas with the polarization direction well oriented to maximize detection efficiency at the SHG crystal phase matching angle. However, the effects of rotating the second harmonic crystal are multifold and not limited to the change of second harmonic power. First of all, it results in a change of polarization of the second harmonic beam. Second, the fundamental beam power changes slightly due to different conversion rate to second harmonic. Third, the second harmonic crystal is birefringent, so the linear polarization of the fundamental beam can be changed to elliptical when the polarization direction is rotated away from the crystal main axis. These effects added together make the experiment below not adequate to efficiently test the second harmonic power dependence.

Figure 5.8 shows the linearly fitted experimental results for both 3.2 μm/1.6 μm and 4.8 μm/2.4 μm pump beam, the power law fitting in Fig. 5.8 (a) and (c) show a power index of 1.8 and 11, respectively. A large discrepancy of simple power law fitting with different pump wavelengths is not a surprise considering all the factors described above. The peak THz signals does not follow a linear dependence of the 2ω beam power in this experiment as expected from independently tuning the second harmonic power. For a clean experiment, a Michelson interferometer setup is expected, so that the fundamental beam and the second harmonic beam can be separated in two different arms and changed separately.

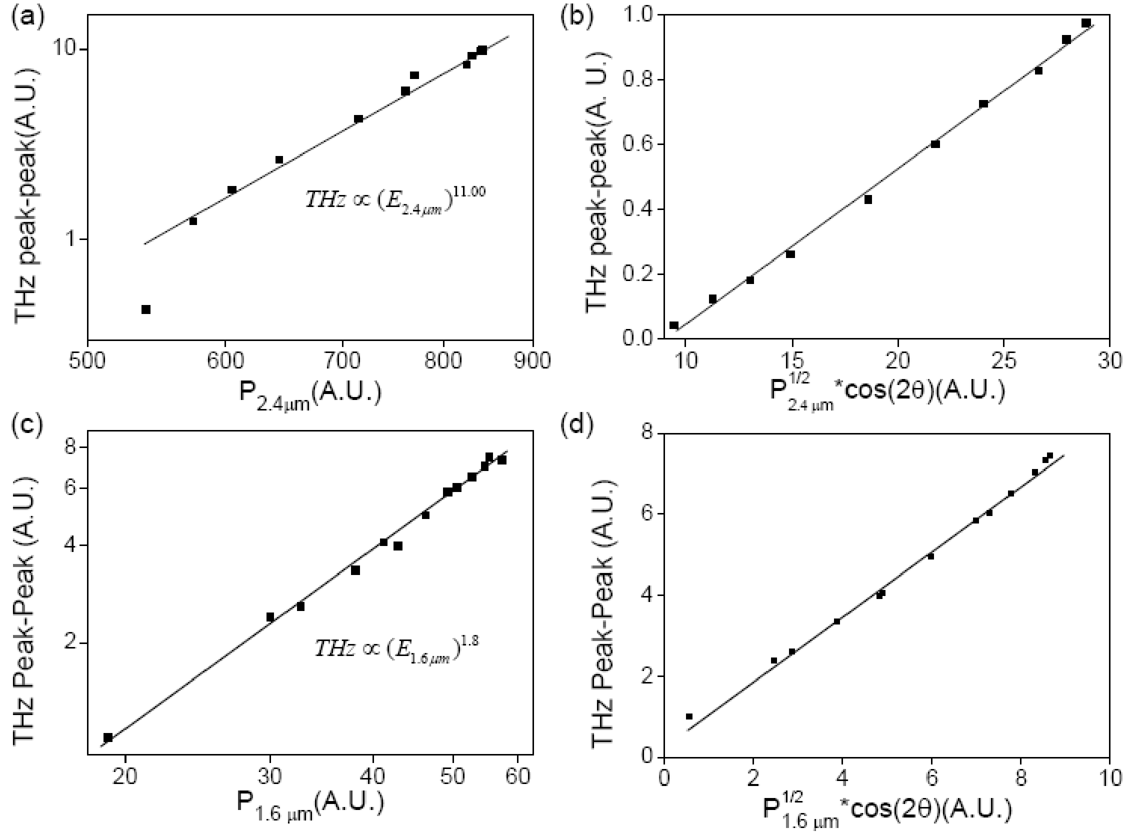

Figure 5.8: Second Harmonic Beam Power Dependence. (a) Log-log plot of THz peak-peak dependence on the second harmonic power with 2.4 μm/4.8 μm pump beam, the data can be fitted by simple power law dependence with power index of 11. (b) THz peak-peak plot as function of $P^{1/2}_{2.4\mu m}*\cos(2\theta)$ with 2.4 μm/4.8 μm pump beam, where θ is the SHG crystal phase mismatching angle, the linear fitting shows: $E_{THz} \propto P^{1/2}_{2.4\mu m}*\cos(2\theta)$. (c) Log-log plot of THz peak-peak dependence on the second harmonic power with 1.6 μm/3.2 μm pump beam, the data can be fitted by power law dependence with power index of 1.8. (d) THz peak-peak plot as function of $P^{1/2}_{2.4\mu m}*\cos(2\theta)$ with 1.6 μm/3.2 μm pump beam, where θ is the SHG crystal phase mismatching angle ,the linear fitting shows: $E_{THz} \propto P^{1/2}_{1.6\mu m}*\cos(2\theta)$.

Despite the complexity of the multiple effects of phase mismatch of SHG crystal, we find the experimental data follows a fitting of $E_{THz} \propto P_{2\omega}^{1/2} * \cos(2\theta)$ as shown in Fig. 5.8 (b) and (d) for both pump wavelengths. If we neglect the effect of the birefringent of the SHG crystal and assuming the generated second harmonic beam polarization rotates the same angle with the SHG crystal. This can be easily understood from the fact that only the projection of the fundamental beam on the phase matching angle direction can generate the perpendicular

polarized (relative to the projection of the fundamental polarization to the phase match angle) second harmonic beam. Then the angle between the second harmonic beam polarization and the fundamental beam polarization is θ, and from Eq. 5.8, the generated current direction and thus the polarization of the generated THz field is rotated by 2θ degree, after the THz polarizer, and the emitted THz signal has linear dependent on the second harmonic beam power $E_{THz} \propto P_{2\omega}^{1/2}$, we can get $E_{THz} \propto P_{2\omega}^{1/2} * \cos(2\theta)$. Unfortunately, both SHG crystals used in this experiment give significant birefringence when the fundamental beam doesn't propagate along the main axis of the crystal, which can change the polarization into elliptically polarized light depending on the rotation angle and crystal thickness which complexes the interpretation and fitting of the data.

5.5.6 Sample Dependence

Although the data shown so far are all taken on sample #7J8 (63 layers), experiments with both 1.6 μm/3.2 μm and 2.4 μm/4.8 μm are performed on other three samples (#8B2 (9 layers), #1104 (13 layers), #1133 (35 layers)) with different numbers of layers. Beside layer number dependence, another motivation of this experiment is to determine whether major contribution of coherent control signal comes from all graphene layers or it's only dominated by the doped layers. Since the 1.6 μm/3.2 μm pump beam wavelength is well selected to be the transition right above the Fermi level of the most heavily doped layer, so that the injected directional electron is very close to the Fermi energy of this layer, where the scattering processes are suppressed compared to the undoped layers and thus allowing us to have a very long mean free path when we initially designed the experiment.

Figure 5.9 shows peak THz amplitude of different positions on different samples with either 3.2 μm/ 1.6μm or 4.8 μm/ 2.4 μm pump wavelengths. Sample #7J8 (63 layers) shows the best

homogeneity which coincides with the homogeneity of the infrared DT signal. Sample #1133 (35 layers) shows 50% THz amplitude changes on different positions on the sample. The other two samples are also quite inhomogeneous but the variation of the THz signal over different positions of the sample is less observable due to the relative low THz signal level.

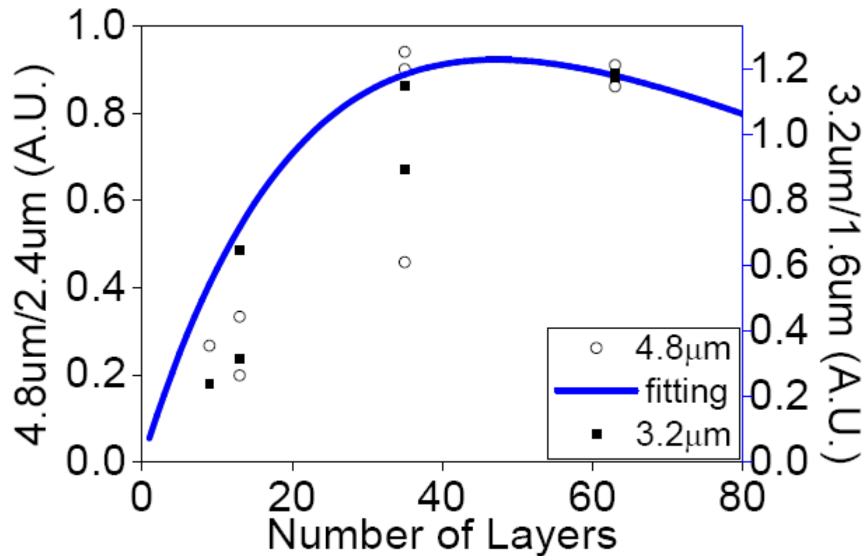

Figure 5.9: Sample Dependence. Coherent control generated THz peak-peak amplitude with 4.8 μm and 3.2 μm fundamental beam wavelengths on different positions on different graphene samples are plotted as a function of the number of graphene layers. The data with different fundamental beam wavelength are normalized with each other according to the same average THz peak signal on sample #7J8 in the plot and fit together with a single fitting curve.

From Fig. 5.9, we can rule out the possibility that the doped layers dominate the contribution to the THz signal for at least two experimental facts: first, although the 35 layers sample and 63 layers sample have similar amplitudes, the other two thin samples show significantly lower signal levels. Second, both 3.2 μm/ 1.6 μm and 4.8 μm/ 2.4 μm pump show similar sample layer number dependent trends, where 3.2 μm/ 1.6 μm pump excites carriers right above the Fermi level of the most heavily doped layer while 4.8 μm/ 2.4 μm doesn't.

Now we assume all the layers have the same THz response to the pump beam regardless whether it's undoped or doped layers, this is a good assumption only when the doped layer

doesn't have significantly large signal contribution compared to the undoped layers. Since the number of undoped layers always dominates in any of the samples, the assumption that doped and undoped layers contributes the same to the signal doesn't significantly affect our fitting. Under this assumption, the signal amplitude doesn't increase monotonically with increasing number of graphene layers for the simple reason that each graphene layer absorbs both THz radiation and mid-IR pump beam, and the THz generated in the top layers is greatly attenuated by the bottom layers if there are too many layers. To modeling this, we assume a flat spectrum absorption coefficient of 2.3% at any wavelength [30], although the absorption changes slightly when shifting to lower photon energy end [31]. The emitted THz is proportional to the $E_{THz} \propto \mathbf{E}_{\omega}^{2}\mathbf{E}_{2\omega}$, so the enhancement factor of N layers respect to a single layer is: $En = \sum_{k=1}^{N} (x^{k-1})^{3} x^{N-k}$, where $x = (1-2.3\%)^{1/2}$ is the transmission coefficient of electric field by one graphene layer. Figure 5.9 shows that this model fits the experiment very well, and the fitting predicts the optimum layer number to be 47 layers.

5.5.7. The Effect of Pre-injected Hot Carriers

Another interesting experiment which can give fundamental insight into dephasing of quantum coherence is pre-injecting hot carriers with an 800nm pulse before the arrival of the 3.2 μm/ 1.6 μm pump beam to see how the pre-injected hot carriers affect the coherent controlled current and its THz emission. For this purpose, a beam path of an 800nm pre-pulse is added and focused to a 120 μm spots on the sample with 45° incident angle to excite background hot carriers with tunable relative delay before the arrival of the ω/2ω pulses. The intensity of the pre-pulse is also continuously tunable with a neutral density filter. At the same time a flip mirror is added right after the ZnTe crystal to switch the transmitted mid-IR beam to a monochromator, followed by an InSb photo detector to get the in-situ mIR-IR

differential transmission signal as shown in Fig. 5.10. When switching to the differential transmission experiment, the HDPE plate has to be removed to unblock the transmitted mid-IR and the chopper is switched to chop the 800 nm pre-pulse. For coherent control experiment, the chopper is also moved to chop the pre-pulse to measure the differential coherently controlled THz signal due to the pre-pulse injected hot carriers.

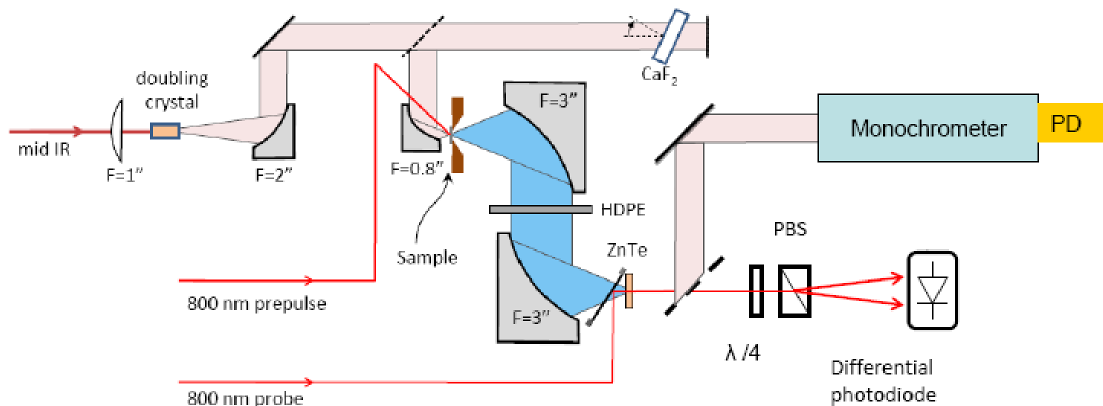

Figure 5.10: Experiment Setup for Coherent Control Experiment with In-situ Differential Transmission Measurement.

Figure 5.11 shows the emitted coherent controlled THz at different pre-pulse injection power and different time delays. In this experiment, the rotational angle of CaF_2 retardation plate is fixed at the position that gives the maximum THz signal, both pre-pulse power and the time delay between the pre-pulse and pump beam are tuned to see how it affects the emitted THz signal. From the Fig. 5.11, the THz signal amplitude decreases monotonically with increasing pre-pulse energy and increase monotonically with the relative delay after the pre-pulse injection. However, in any cases, the THz waveform doesn't change with the pre-pulse injection which indicates that the space charge effect is not significant at these hot carrier injection intensities, this can be due to the very fast dielectric relaxation time and generated space charges are quickly screened and don't give any effect in the signal. In case the space charge effect plays a role, the generated spatial separated charges can build up an internal

electrical field which makes the electrons move in opposite direction away from the injected coherent controlled current. The pre-injected hot carries also increase the conductivity of the graphene sheet, which can enhance the current intensity from the space charge effect. Since the THz emission from this current has a relative delay with respect to the coherently controlled THz emission, this back drift current can affect the emitted THz waveform shape besides the amplitude.

Besides the space charge effect, the injected hot carriers can occupy high energy levels in the conduction band and cause Pauli blocking to the absorption of the ω/2ω pump beam which can also decrease current generation and THz signal. To measure this effect quantitatively, we conduct an in-situ pump-probe experiment with the coherent control experiment, since an infrared differential transmission signal from the pump-probe experiment is supposed to be mainly due to the Pauli blocking effect of hot carrier occupations of high energy levels from the previous results in Chapter 3. The pump probe DT/T signal is plotted along with the differential THz signal normalized by the THz signal without pre-pulse in Fig. 5.12, the prepulse power are 4.1 mW and 20.6 mW respectively in Fig. 5.13. The experiment shows two important features: first, the time-zero DT signal from pump-probe experiment is about an order of magnitude smaller than the normalized differential THz signal, which means Pauli blocking is not the main contribution to the differential THz signal; second, the decay of the differential THz signal follows the decay of the DT signal closely which is supposed to be related to the decay of the hot electron temperature and we'll discuss this effect in details later.

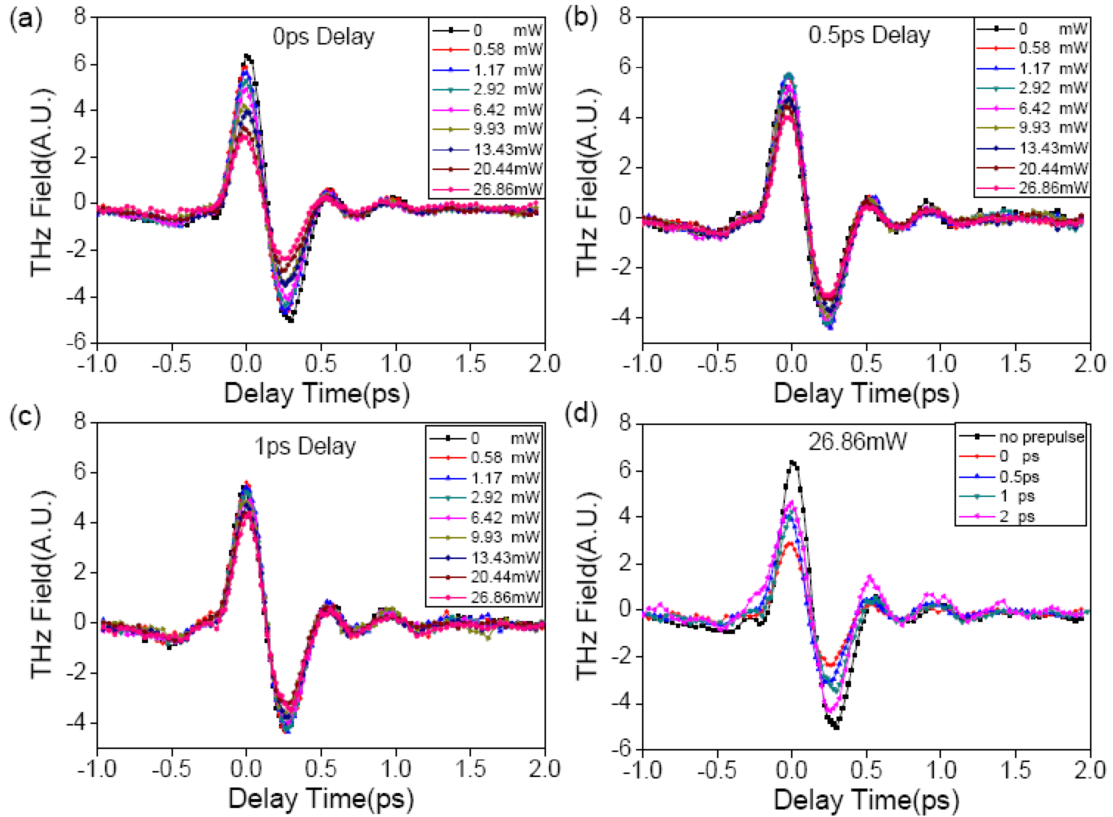

Figure 5.11: Coherent Controlled THz Waveform. THz waveform with different pre-pulse injection intensity at different pre-pulse delays. All the data are taken with 3.2 µm/1.6 µm pump and 800 nm pre-pulse with 45 degree incidence angle and 120µm diameter focal spot on the sample. (a), (b) and (c) THz waveform at 0 ps, 0.5 ps and 1 ps time delay with pre-pulse power of 0 mW, 0.56 mW, 1.17 mW, 2.92 mW, 6.42 mW, 9.93 mW, 13.43 mW, 20.44 mW and 26.66 mW, respectively. (d) THz waveform with pre-pulse power of 26.86 mW at 0 ps, 0.5 ps, 1 ps and 2 ps time delay, respectively. In each of above, a set of data without any pre-pulse injection is used for reference.

Another significant effect of the hot carriers is that it can significantly increase absorption in THz frequency region, this is observed in 800 nm pump THz probe experiment conducted by Chuck Divin in our group. Since the probe focal spots in THz pump-probe experiment is limited by the diffraction limit of THz wavelength, the highest 800nm pump power intensity is many orders smaller than the pre-pulse intensity used in the coherent control experiment. A pump-probe experiment with the same pump intensity with that used in the pre-pulse experiment is not available. However, a pump power dependent study of 800 nm pump THz

probe experiment shows a saturation effect at high pump power as shown in Fig. 5.14 (courtesy of Chuck Divin): the interpolation of 280K data shows that even with 1 mW/cm^2 pump fluency, the dt/t is about 25%. Since in pump probe experiment, all the graphene layers contribute to the change of THz absorption, while in pre-pulse experiment, only half of the layers on average contribute to the change of THz absorption, which further deducts the contribution from this effect to be 12%.

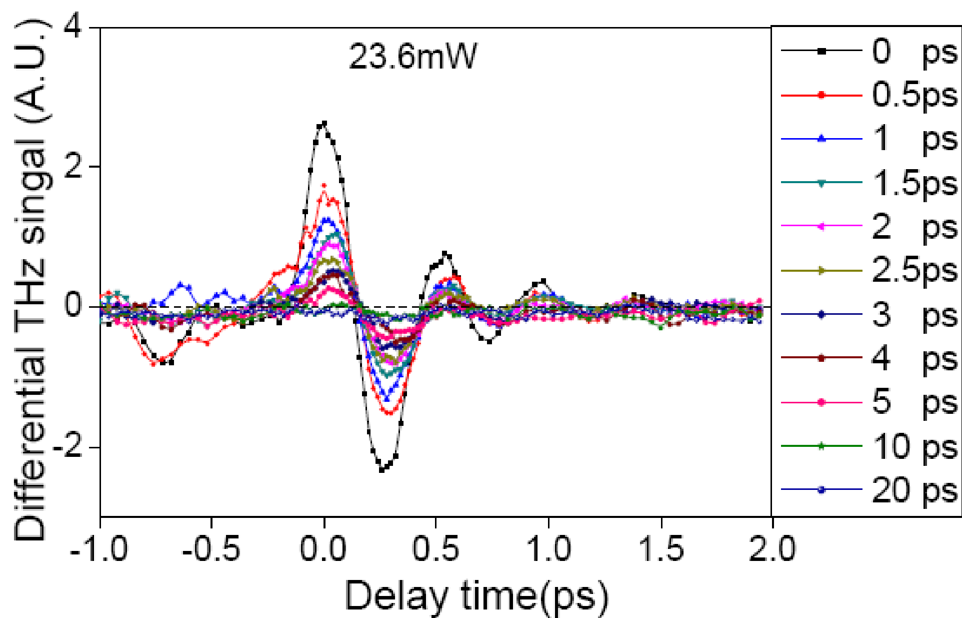

Figure 5.12: Differential THz Signal Waveform. Here is pre-pulse power is 23.6 mW, data are taken at various delay times relative to the pre-pulse. The coherent control experiment is pumped with 1.6μm/3.2 μm in all the plots.

Figure 5.15 plots together the normalized differential THz signal with 1 mW/cm^2 pre-pulse influence and dt/t signal of pump-probe experiment with 17 μJ/cm^2 pump intensity to compare the relaxation process. The data shows that the dt/t signal relaxes significantly slower than the differential THz signal, which provides evidence that the hot carries induced THz transmission change is not the dominating effect to give the differential THz signal.

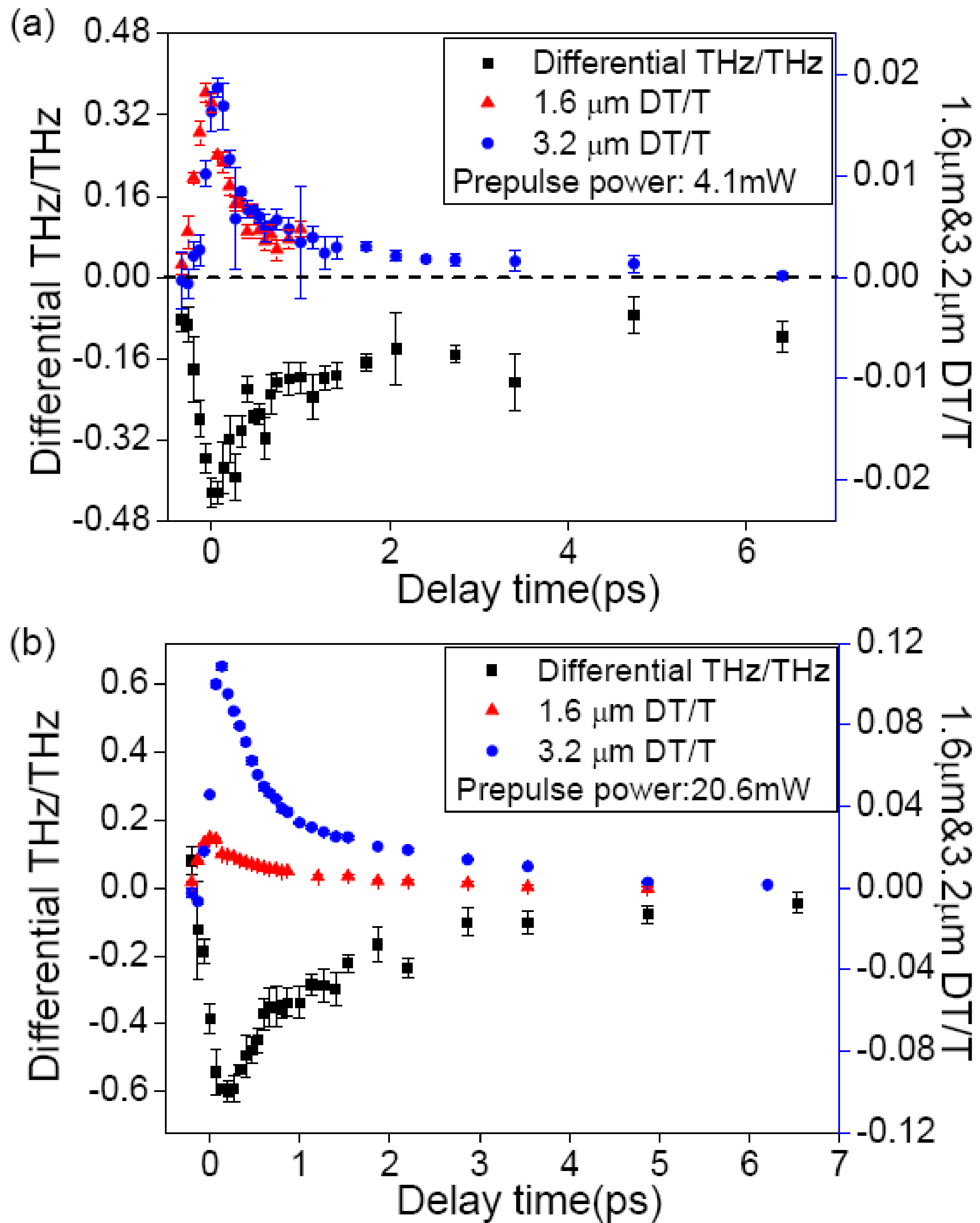

Figure 5.13: Differential THz Signal and In-situ Mid-IR Pump-probe Signal. (a) Time scan of normalized differential THz signal and in-situ differential transmission signal with 1.6μm, 3.2 μm probe wavelength, all pumped with 4.1 mW 800nm. (b) Time scan of normalized differential THz signal and in-situ differential transmission signal with 1.6μm, 3.2 μm probe wavelength, all pumped with 20.6 mW 800nm pre-pulse. The coherent control experiment is pumped with 1.6μm/3.2 μm in all the plots.

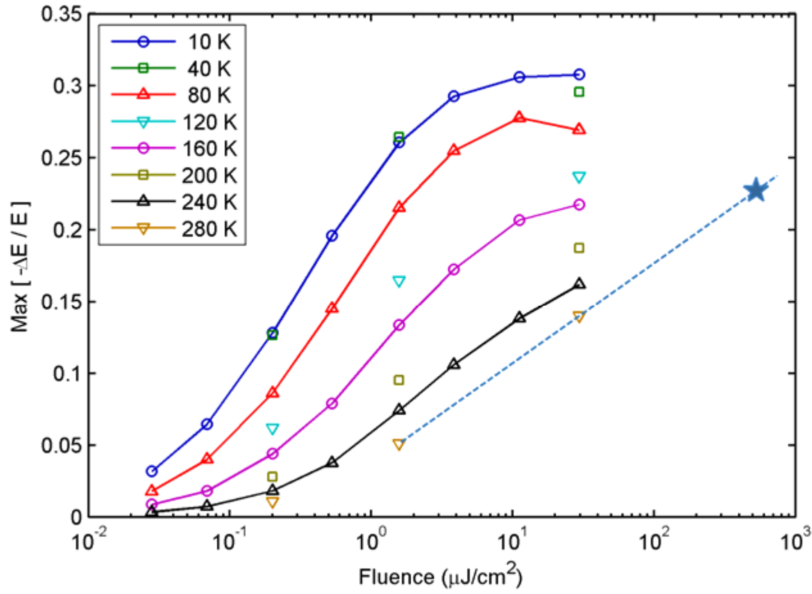

Figure 5.14: Power Dependent THz Probe dt/t Data at Different Temperature. Here dt is the change of transmission of the THz field, the interpolation of the 280 K data shows the that even with pump fluency of 1 mW/cm^2, the peak dt/t signal is about 25%. Courtesy of Chuck Divin.

If we take off the contribution from Pauli blocking of the pump beam absorption and hot carrier induced THz absorption, there is still more than 40% differential THz signal due to other mechanisms. The injected hot carriers increases the electron-electron scattering rate; however the elastic scattering doesn't affect the current, since this process simply transfers the momentum of one electron to another and there is no net momentum loss during this scattering. So the electric current is conserved after this scattering. Electron-phonon scattering changes the electron velocity and thus degrades the generated ballistic current. However it takes almost 1 ps time scale for the hot electrons to emit optical phonon, so there is not enough time for the phonon scattering to give a big differential THz signal at zero time delay. So hot carriers won't affect THz signal significantly once coherent controlled directional current is generated.

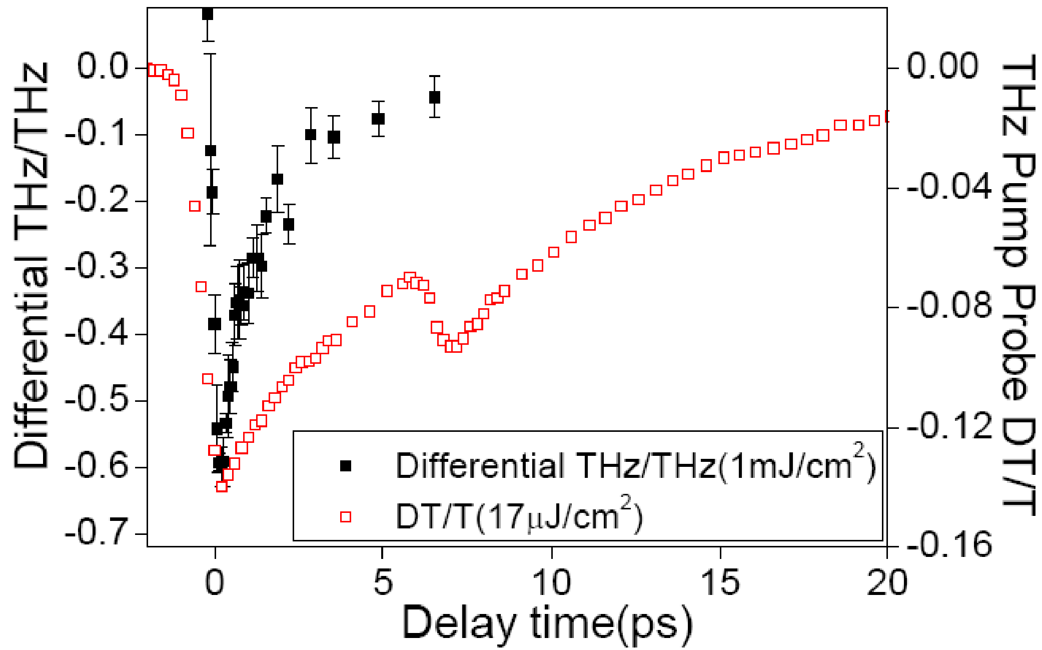

Figure 5.15: Normalized Differential THz Signal and dt/t Signal. Normalized differential THz signal with 1 mJ/cm^2 and pre-pulse fluence at varies time delays and time scan of 800nm pump and THz probe dt/t signal with 17 μJ/cm^2 pump power. The pump probe experiment is performed at 280 K instead of room temperature. The coherent control experiment is pumped with 1.6μm/3.2 μm.

To summarize the above analysis, the injected hot carriers contribute to the differential THz during the current generation process. This is not a big surprise since the directional current generated from coherent control process relies on the interference effect between one photon and two photon transition paths. If the phase relationship between these two paths is broken during the optical transition process, the injected carriers have an equal possibility to move in any directions and contribute no net current. The broking of this phase relationship is simply due to fast electron-electron scattering and happens almost instantaneously. From Fig. 5.11, we can see that the phase breaking process is more notable at high electron temperature and decreases monotonically with electron temperature. The almost synchronized relaxation curves between the differential THz signal and pump probe DT signal shown in Fig. 5.13 indicate that the phase breaking scattering simply follows hot electron temperature relaxation.

This results is a high electron temperature extension of reference [32], where they show that the phase breaking collisions in steady state transport region yields a phase breaking time inversely proportional to the carrier temperature from 1.4 K to room temperature, which is the same behavior we observed in the high electron temperature region.

5.6 Optical Effect

In this section, we discuss the factors that can potentially affect photo current injection in the coherent control experiment from the optical aspects. This includes pulse broadening, temporal walk-off, chirp and delayed pulses.

5.6.1 Spectrum Bandwidth in Second Harmonic Generation

Second harmonic generation is used to create phase related ω and 2ω beams in the coherent control experiment. A detailled theoretical treatment of second harmonics generation can be found in any nonlinear optics textbook [33]. Here we discuss the spectrum bandwidth in second harmonic generation only. For monochromatic beams, collinear phase matching requires that n(ω)=n(2ω), when a finite bandwidth is involved this condition extends to:

$$\frac{dn(\omega)}{d\omega}-\frac{dn(2\omega)}{d\omega}=0\,. \tag{5.20}$$

Here the derivatives are associated with the group velocity of each pulse. Consequently, in the presence of unequal group velocities, phase matching is not satisfied for the whole pulse spectrum and the 2ω pulse time envelope and spectrum is affected.

Let's assume that the pump pulse remains undepleted throughout the interaction, which is an acceptable approximation for the low conversion efficiency in our experiments (less than 10%). Then we can identify two regimes for the parametric process: the first when the interaction length l (or crystal length, whichever is shorter) is smaller then l', and the second when $l>l'$, where l' is the walk-off length defined as

$$l' = (|\Delta v_g^{-1}| \Delta\omega)^{-1}, \tag{5.21}$$

$\Delta\omega$ is the frequency bandwidth and Δv_g^{-1} is the inverse group velocity mismatch given by

$$\Delta v_g^{-1} = \frac{1}{c}(n(2\omega) - n(\omega) + \omega\frac{dn(2\omega)}{d\omega} - \omega\frac{dn(\omega)}{d\omega}), \tag{5.22}$$

The length l' corresponds to the distance over which the relative phase of the pulses changes by 1 radian due to dispersion. When $l > l'$ the frequency doubling process takes place almost the same way as under conditions of perfect group velocity matching: the full spectrum is phase matched, the pulses are overlapped in time (no group delay) and $\tau_{2\omega} = \tau_\omega / \sqrt{2}$. Since phase matching is satisfied, the phase relationship between ω and 2ω is preserved across the pulse even in the presence of a frequency chirp.

In the situation where $l > l'$, the pulse time delay at the exist of the crystal can be shown to be:

$$t_d \approx \frac{l}{2\Delta v_g}. \tag{5.23}$$

As a result of this time delay, the 2ω pulse spreads from minimum time duration of $\tau_\omega / \sqrt{2}$ to

$$\tau_{2\omega} \approx (\frac{\tau_\omega^2}{2} + (\frac{l}{\Delta v_g})^2)^{1/2}. \tag{5.24}$$

5.6.2 Pulse Broadening and temporal walk-off

Femtosecond ultrafast pulse has a minimum frequency bandwidth determined by their duration. When it propagates through media such as lenses, windows, polarizers and waveplates introduces pulse broadening, chirping and temporal walk-off between the ω and

2ω pulses. In phase sensitive experiments, these effects can be crucial.

As the two pulsed exit the doubling crystal and propagate through other optical elements, pulse broadening and temporal walk-off take place. The broadening pulse duration is:

$$\Delta\tau(z) \approx (D\Delta\lambda)z\,, \tag{5.25}$$

where z is the propagation distance. $\Delta\lambda$ is the spectral width and D is the broadening coefficient given by:

$$D = \frac{\lambda}{c}\left(\frac{\partial^2 n}{\partial\lambda^2}\right). \tag{5.26}$$

The effect of D, either compressing or broadening the pulse-depends on the sign of the frequency chirp. For D>0 (normal dispersive medium), a positively chirped pulse experiences increasing chirp and duration, but starts compressing if D<0. The converse situation applies to a pulse with negative chirp.

5.6.3 Current Injection with Chirped and Delayed Pulses

To a first approximation, a frequency chirp in a pulse can be expressed by a linear term such that:

$$\omega(t) = \omega_0 + 2bt\,, \tag{5.27}$$

with ω_0 the center frequency and b the chirp parameter. Assuming a Gaussian pulse envelope, the relationship of *b* to the pulse duration $\Delta\tau$ and frequency bandwidth $\Delta\omega$ is given by

$$b = \frac{2\ln 2}{\tau^2}\left[\left(\frac{\Delta\tau\Delta\omega}{4\ln 2}\right)^2 - 1\right]^{1/2}. \tag{5.28}$$

Hence, if b_ω and $b_{2\omega}$ are the chirp parameters for ω and 2ω and the pulses are delayed relative to each other by a time t_d, the phase difference as a function of time is:

$$\Delta\phi(t) = 2\phi_\omega(t+t_d) - \phi_{2\omega}(t) = 2b_\omega(t+t_d)^2 - b_{2\omega}t^2\,. \tag{5.29}$$

When pulse broadening is relatively small, one can assume that $b_{2\omega} = 2b_{\omega}$, since ω and 2ω are phase-related. In this case,

$$\Delta\phi(t) = 2b_{\omega}(2tt_d + t_d^2) . \qquad (5.30)$$

Therefore, a general criterion for chirping to be an important factor in the current injection rate is that:

$$4b_{\omega}t_d\tau_{\omega} > 1 . \qquad (5.31)$$

This corresponds to a phase variation greater then 1 radian within the pulse duration. Note that $\Delta\phi$ remains constant if $t_d = 0$.

The rate equation for the current injection can be written as:

$$\dot{J}^{I} = \eta \,|\, \vec{E}_{\omega} \,|^2 |\, \vec{E}_{2\omega} \,|^2 \sin(\Delta\phi) - \frac{J}{\tau_c} , \qquad (5.32)$$

which becomes:

$$\dot{J}^{I}(b_{\omega}, t_d) = 2^{5/2}\eta(\mu_0 / \varepsilon_0)^{3/4} n_{\omega} n_{2\omega}^{1/2} I_{\omega}(t) I_{2\omega}^2(t - t_d)\cos(4b_{\omega}t_d t) - \frac{J}{\tau_c} , \qquad (5.33)$$

where η is the proper tensor element of $\hat{\eta}$. Any delay between the pulses then reduces the amount of current injection because of non-ideal pulse overlap and also reduces the integrated current because of the variation in $\Delta\phi$.

5.7 Conclusions

In conclusion, we have generated coherently controlled electrical currents in epitaxial graphene using both 3.2 μm/1.6 μm and 4.8μm/2.4 μm, 280fs pulse. These ballistic currents depend on the relative phase between pulses, and the direction of generated current follows closely with the theoretical prediction. Our results are encouraging for all-optical generation of electrical currents in epitaxial graphene and may bring new understanding to

optoelectronic functionalities. By pre-injection background hot carriers in the system, we have studied the enhancement of the hot carriers in phase breaking scattering process and our results show that this scattering rate increase monotonically with the hot electron temperature.

References

[1] A. Hache, J. E. Sipe, and H. M. van Driel, Quantum Electronics, IEEE Journal of **34**, 1144 (1998).

[2] G. L. Gurevich, and Y. G. Khronopulo, Sov. Phys. JEPT **24**, 1012 (1967).

[3] D. J. Jackson, J. J. Wynne, and P. H. Kes, Physical Review A **28**, 781 (1983).

[4] J. C. Miller *et al.*, Physical Review Letters **45**, 114 (1980).

[5] C. Chen, Y.-Y. Yin, and D. S. Elliott, Physical Review Letters **64**, 507 (1990).

[6] H. G. Muller *et al.*, Journal of Physics B **23**, 2761 (1990).

[7] Y.-Y. Yin *et al.*, Physical Review Letters **69**, 2353 (1992).

[8] F. Wang, C. Chen, and D. S. Elliott, Physical Review Letters **77**, 2416 (1996).

[9] P. Brumer, and M. Shapiro, Accounts of Chem. Res. **22**, 407 (1989).

[10] E. Charron, A. Giusti-Suzor, and F. H. Miles, Phys. Rev. Lett. **71**, 692 (1993).

[11] J. L. Krause, M. Shapiro, and P. Brumer, J. Chem. Phys. **92**, 1126 (1989).

[12] B. Sheehy, B. Walker, and L. F. DiMauro, Physi. Rev. Lett. **74**, 4799 (1995).

[13] A. Shnitman *et al.*, Phys. Rev. Lett. **76**, 2886 (1996).

[14] D. J. Tannor, and S. A. Rice, Adv. Chem. Phys. **70**, 441 (1988).

[15] L. Zhu *et al.*, Science **270**, 77 (1995).

[16] R. Atanasov *et al.*, Physical Review Letters **76**, 1703 (1996).

[17] A. Hach *et al.*, Physical Review Letters **78**, 306 (1997).

[18] E. Dupont *et al.*, Physical Review Letters **74**, 3596 (1995).

[19] R. W. Newson *et al.*, Nano Letters **8**, 1586 (2008).

[20] L. Costa *et al.*, Nat Phys **3**, 632 (2007).

[21] E. J. Mele, P. Kral, and D. Tomanek, Physical Review B **61**, 7669 (2000).

[22] J. Rioux, and J. Sipe, Private Communication (2008).

[23] P. L. McEuen *et al.*, Physical Review Letters **83**, 5098 (1999).

[24] W. Sha *et al.*, Quantum Electronics, IEEE Journal of **28**, 2445 (1992).

[25] C. Lu *et al.*, Nano Letters **4**, 623 (2004).

[26] DasA *et al.*, Nat Nano **3**, 210 (2008).

[27] N. Tombros *et al.*, Nature **448**, 571 (2007).

[28] T. F. Meade, Ph.D Thesis, University of Michigan (2003).

[29] P. C. M. Planken *et al.*, J. Opt. Soc. Am. B **18**, 313 (2001).

[30] R. R. Nair *et al.*, Science **320**, 1308 (2008).

[31] K. F. Mak *et al.*, Physical Review Letters **101**, 196405 (2008).

[32] X. Wu *et al.*, Physical Review Letters **98**, 136801 (2007).

[33] R. W. Boyd, Elsevier Inc. (2008).

Chapter VI

Contributions, Conclusions, and Future Work

In this Chapter, I will summarize the work in this dissertation and look into the experiments and research directions for the future.

6.1 Contributions and Conclusions

The work in this dissertation consists of two major parts: using ultrafast pump-probe spectroscopy to study the hot Dirac Fermion dynamics and using coherent control to generate ballistic currents in carbon-face epitaxial graphene.

In the spectroscopy part, I described the first non-degenerate ultrafast pump-probe experiment on epitaxial graphene in which we observed ultrafast relaxation dynamics of hot Dirac fermionic quasi-particles. The DT spectra are well described by interband transitions with no electron-hole interaction. The temporal resolution of our experiments allowed us to differentiate between the optical phonon and acoustic phonon scattering processes. Following the initial thermalization and emission of high-energy phonons, cooling is determined by electron-acoustic phonon scattering. We observed thermal coupling of hot carriers between graphene layers in epitaxial graphene and determined the interlayer thermal coupling time to be instantaneous within the resolution of the experiment.

We have spectrally resolved the precise doping profile of heavily doped layers and

determined the screening length to be 2-3 layers in carbon-face grown epitaxial graphene using ultrafast 800 nm pump, mid-infrared probe spectroscopy. The measured DT spectrum feature can be well explained by a dynamic conductivity simulation when plane disorders and elevated lattice temperature effects are incorporated into the simulation.

Polarization dependent and pump intensity dependent experiments were also performed to study the carrier-carrier scattering time and electron-phonon coupling strength. The intensity dependent study reveals an interesting hot phonon effect on the electron-phonon coupling.

In the coherent control part, we have generated coherently controlled electrical currents in epitaxial graphene using both 3.2 μm/1.6 μm and 4.8 μm/2.4 μm, 280fs pulses. These ballistic currents depend on the relative phases between pulses, and the direction of generated current is close to the theoretical prediction. The injected current direction doesn't rely on the graphene crystal orientation and can be fully controlled by either changing the relative angle between two linearly polarized pumps or the relative phase of two circularly polarized pumps. Current degradation is found to be different from traditional semiconductors due to graphene's unique electronic structure. The results are encouraging for all-optical generation of electric currents in epitaxial graphene and may bring new understanding to optoelectronic functionalities. By pre-injecting background hot carriers into the system, we studied the enhancement of hot carriers in phase-breaking scattering process and the results show that this scattering rate increases monotonically with hot electron temperature.

6.2 Future Work

6.2.1 Magneto Ultrafast Nonlinear Spectroscopy

Landau level splitting in graphene is unusual compared to equal Landau level splitting in common semiconductors due to its linear energy dispersion. Previous quantum Hall effect

experiments [1] and magneto infrared linear spectroscopy experiments [2] on graphene all show the interesting, new and unique physics of Dirac Fermions. However, the magneto infrared nonlinear spectroscopy of epitaxial graphene has been left unexplored so far. This research will provide an in-depth understanding of the physics of hot Dirac Fermions and build the foundations for using graphene in future spintronic and valleytronic devices.

An effort in this direction was made last August with an 800 nm pump, scanning probe wavelength around 2.4μm and 3T magnetic field to look for the expected Landau level splitting. When the probe wavelength corresponds to the transition between the Landau levels, the pump probe DT signal should be non zero, otherwise no DT signal would be observed due to the lack of the change of electron occupation function due to pump excitation when there is no density of state. However, the Landau level splitting was not observed since the photon energy of the 2.4 μm probe corresponds to a Landau level with broadening larger than the Landau level spacing itself. This was basically due to two limitations in the experimental conditions: an insufficient magnitude of the magnetic field and a probe photon energy that was not low enough. With improvement in either limitation, this experiment should have been successful. Figure 6.1 shows the landau level energy with 3 T and 5 T respectively. For a 5 T magnetic field and 5.4 μm probe from the DFG, the Landau level splitting could be as large as 26 meV. This energy is larger than the Landau level broadening measured by Orlita et al. [1] and should be easily resolved.

Time resolved spectroscopy would provide detailed scattering processes on discrete Landau levels. Rabi oscillations between discrete Landau levels has been proposed theoretically [2] and it would be interesting to look at experimentally. Observation of Rabi oscillations could

lead to the next step in quantum control of these states. Population inversion and lasing with discrete Landau levels in graphene is also an interesting direction.

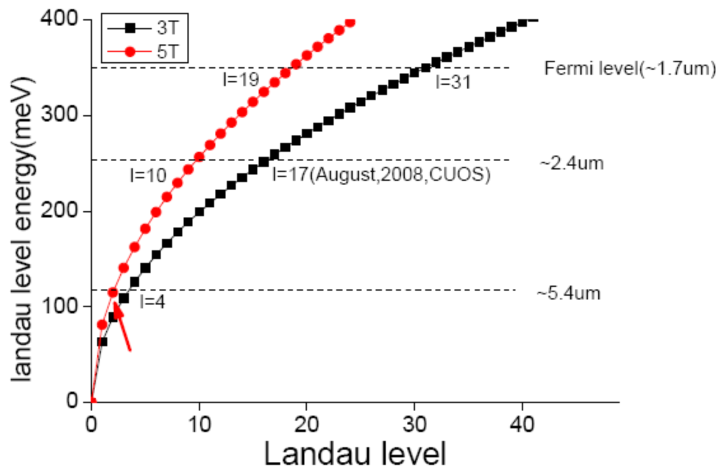

Figure 6.1: Landau Level Energy *vs* Landau Level Number under Different Magnetic Fields. The three horizontal dashed lines label, from highest to lowest respectively, the energy of the Fermi level of the most heavily doped layer, the lowest probe photon energy of the IR-OPA and the preferred probe photon energy of the DFG. The Landau level number is labeled at which landau level energy the probe photon corresponds to at different magnetic field strength.

6.2.2 Exfoliated and CVD Grown Graphene, Graphene Bilayer

As a spontaneous yet nontrivial extension of my research described above parallel work (with or without magnetic fields) is expected on exfoliated and CVD grown graphene samples as well as graphene bilayers to study how different growth mechanisms and substrates affect ultrafast carrier dynamics.

Exfoliated graphene as a clean graphene sample provides a hygienic platform to study intrinsic graphene properties and the role of naturally formed ripples [3, 4] on transport properties. Back electrical gate can be relatively easily fabricated by doping a Si substrate which provides flexibility for gate controlled studies [5, 6].

CVD grown graphene is still a very new material and its properties are largely unexplored. This growth method, however, holds great promise for future industrial fabrication of low-

cost graphene devices with CMOS compatibility and flexibility of transferring onto various substrates [7-9].

Graphene bilayers have parallel parabolic band structures with no bandgap. What makes this interesting is that a bandgap can be easily opened by applying an electric field [10, 11]. Comparison between bilayer and single layer graphene can provide a physical insight for an effect of linear dispersion curve in graphene transport properties. Also the bilayer shows interesting integer quantum hall effect anomalies [12], so it would be interesting to look into its behavior under a magnetic field.

6.2.3 Nonlinear Frequency Multiplication

The nonlinear frequency multiplication effect of graphene has been investigated theoretically by S. A. Mikhailov and K. Ziegler [13]. This effect is a direct result of graphene's unique linear dispersion curve as shown in the following.

For a 2D particle, the energy spectrum is $E_{p2} = V\sqrt{p_x^2 + p_y^2}$. According to Newton's equation of motion, $dp_x / dt = -eE_x(t)$, under an external time-dependent harmonic electric field $E_x(t) = E_0 \cos \Omega t$, the momentum $p_x(t)$ is then given by the sine function $p_x(t) = -(eE_0 / \Omega) \sin \Omega t$. In conventional 2D electronic systems with parabolic energy dispersion, the response is linear with the same frequency. This is simply due to the fact that under parabolic energy dispersion the velocity v_x and hence the current $j_x = -en_s v_x$ are proportional to the momentum p_x. However, in graphene, the velocity

$$v_x = \frac{\partial E_{p2}}{\partial p_x} = V \frac{p_x}{\sqrt{p_x^2 + p_y^2}}, \tag{6.1}$$

which is a strongly nonlinear function of p_x. Therefore the local field polarization has a substantially anharmonic response. Also, the nonlinear response only has odd harmonics whose coefficients fall off very slowly with the harmonic number. S. A. Mikhailov and K. Ziegler also give the threshold intensity of the external field to see the nonlinear response [13].

This odd high harmonics response has been observed experimentally in carbon nanotubes which have a similar linear dispersion curve [14, 15]. Our attempt to generate a third harmonic response on sample #7J9 with 4.8 µm pulse was not successful, although the Mid-IR intensity was far above the nonlinear threshold. A possible reason may be that the condition [13] $\hbar\Omega << \max(\mu,T)$ was not well satisfied since the 4.8µm fundamental beam was quite close to the Fermi level of the most heavily doped layer. For this reason, further work could include testing with higher intensity THz fields.

6.2.4 Generation and Probe the Pseudospin /Valley Polarization

Pseudospin is a unique quantum number due to graphene's Dirac Fermion properties[16]. It originates from the two triangular sub-lattices in graphene's honeycomb structure. Pseudospin is interesting to both fundamental physics and for device applications that have been termed pseudospintronics or Valleytronics [17, 18]. Optical generation of the Valley and pseudospin polarization have been proposed theoretically in the literature recently [19, 20] by using a polarized THz field. Experimental generation and probe of the this polarization will have a profound impact on graphene based valley optoelectonics.

6.2.5 Reflection of Coherent Controlled Ballistic Current

Although all optical generation of photocurrent using a quantum interference effect has been demonstrated in this dissertation, the ballistic nature and the mean free path of this generated

photocurrent remain unproven. A straightforward way to address this problem is by measuring roundtrips of ballistic electrons bounded back and forward by the edges of a graphene nanoribbon or well defined potential well on epitaxial graphene. This back reflected ballistic electron can generate a THz field with the direction of polarization reversed. The THz field would have a time delay corresponding to the roundtrip time which would give a good measurement of the mean free path and the swarm velocity of the generated current.

6.2.6 Ballistic Dirac Fermions in Magnetic Field

Another extension of the current control work would be putting optically injected ballistic Dirac Fermions in a magnetic field to look into their cyclotron motion. The radially polarized THz field emitted in this configuration should convey the rich time-resolved magnetic transport mechanisms in the sample.

6.2.7 Toward Graphene Based Optoelectronic Devices

Although the major effort so far has been a focus on graphene based electronic devices, graphene's potential in THz and mid-infrared optoelectronic devices should not be underestimated. The tuneable narrow-bandgap and gating feature [6] of graphene hold promise for infrared and THz lasers, detectors, tuneable optical switches and modulators. There will be long-term efforts devoted to this direction from both the fabrication and device physics aspect.

References

[1] M. Orlita *et al.*, Physical Review Letters 101, 267601 (2008).

[2] B. Dora *et al.*, Physical Review Letters 102, 036803 (2009).

[3] A. Fasolino, J. H. Los, and M. I. Katsnelson, Nat Mater 6, 858 (2007).

[4] J. C. Meyer *et al.*, Nature 446, 60 (2007).

[5] K. S. Novoselov *et al.*, Science 306, 666 (2004).

[6] F. Wang *et al.*, Science 320, 206 (2008).

[7] L. Gomez De Arco *et al.*, Nanotechnology, IEEE Transactions on 8, 135 (2009).

[8] K. S. Kim *et al.*, Nature 457, 706 (2009).

[9] A. Reina *et al.*, Nano Letters 9, 30 (2009).

[10] E. McCann, and V. I. Fal'ko, Physical Review Letters 96, 086805 (2006).

[11] E. V. Castro *et al.*, Physical Review Letters 99, 216802 (2007).

[12] K. S. Novoselov *et al.*, Nat Phys 2, 177 (2006).

[13] S. A. Mikhailov, and K. Ziegler, arXiv:0802.441v1 (2008).

[14] C. Stanciu *et al.*, Applied Physics Letters 81, 4064 (2002).

[15] A. M. Nemilentsau *et al.*, Carbon 44, 2246 (2006).

[16] A. K. Geim, and K. S. Novoselov, Nat Mater 6, 183 (2007).

[17] H. Min *et al.*, Physical Review B 77, 041407 (2008).

[18] A. Rycerz, J. Tworzydlo, and C. W. J. Beenakker, Nat Phys 3, 172 (2007).

[19] W. Yao, D. Xiao, and Q. Niu, Physical Review B 77, 235406 (2008).

[20] J. Zhou, arXiv:0807.0667v1 (2008).

Appendices

Appendix A

Electron Heat Capacity of Single Graphene Layer

In this appendix, we calculate the electron heat capacity for single graphene layer in both neutral and heavily doped region. For this purpose, first, we calculate the density of state for 2 dimensional Dirac Fermion, we assume a linear E-k dispersion curve:

$$E_{\pm}(\vec{k}) = \pm\hbar v\left|\vec{k}\right|, \tag{A.1}$$

Here v is the Fermi velocity. The number of state in energy interval ΔE is

$$\Delta Z(\Delta E) = \frac{A}{(2\pi)^2}\int dl dk = \frac{A}{(2\pi)^2}\int \frac{dl}{\nabla_k E}\Delta E \tag{A.2}$$

Add 2 fold spin degeneracy and 2 fold valley degeneracy, so the density of state is:

$$N(E) = \frac{A}{(2\pi)^2}\int \frac{dl}{\nabla_k E} = \frac{2A}{\pi}\frac{E}{\hbar^2 v^2} \tag{A.3}$$

Then we can calculate the electron heat capacity using standard statistic mechanic method. We have to distinguish two different cases, the layer with neutral doping intensity and the layer in heavily doped region.

A.1 Electron heat capacity of the undoped graphene layer

For undoped graphene layer, the Fermi level sits at the Dirac point at any temperature, and this is enforced by the particle-hole symmetry of graphene, so the mean excitation energy of this system at finite temperature satisfies:

$$E(T)-E(0)=\sum_{k,s_z}[<n_+(k)E_+(\vec{k})>+<1-n_-(k)>)E_-(\vec{k})]=2\sum_{k}2<n_+(k)>E_+(\vec{k}), \qquad (A.4)$$

which can be converted to:

$$E(T)-E(0)=4A\int_0^\infty dx\frac{E_+(\vec{k})}{\exp(\frac{E_+(\vec{k})}{k_BT_e})^x+1}, \qquad (A.5)$$

where $x=\beta\hbar ck$:

$$E(T)-E(0)=\frac{4A}{\pi}k_BT(\frac{k_BT}{\hbar v})^2\int_0^\infty dx\frac{x^2}{e^x+1}, \qquad (A.6)$$

So:

$$C_e(T_e)=\frac{\partial E}{\partial T_e}=\frac{18\zeta_3}{\pi}Ak_B(\frac{k_BT_e}{\hbar v})^2, \qquad (A.7)$$

where $\zeta_3=\int_0^\infty dx\frac{x^2}{e^x+1}$ is the Riemann zeta function.

A.2 Electron heat capacity of the doped graphene layer

Since the temperature dependent of the Fermi level need to be taken into account in calculating the electron heat capacity in this case, we tried to get the temperature dependence of the Fermi level first. This calculation follows the standard method used to determine the Fermi level of metal in any solid state text books.

Suppose N is the number of free electrons then:

$$N=\int_0^\infty f(E)N(E)dE, \qquad (A.8)$$

And we introduce a function defined as $Q(E)=\int_0^E N(E)dE$ which means the total number of quantum state below energy E and do partial integration we get:

$$N=\int_0^\infty Q(E)(-\frac{\partial f}{\partial E})dE\,, \tag{A.9}$$

We do Taylor expansion of Q(E) around E_F to the second order:

$$Q(E)=Q(E_F)+Q'(E_F)(E-E_F)+\frac{1}{2}Q''(E_F)(E-E_F)^2+\cdots, \tag{A.10}$$

$$-\frac{\partial f}{\partial E}=\frac{1}{k_BT}\frac{1}{(e^{(E-E_F)/k_BT}+1)(e^{-(E-E_F)/k_BT}+1)}, \tag{A.11}$$

Then

$$N=Q(E_F)\int_{-\infty}^{\infty}(-\frac{\partial f}{\partial E})dE+Q'(E_F)\int_{-\infty}^{\infty}(-\frac{\partial f}{\partial E})dE(E-E_F)+\frac{1}{2}Q''(E_F)\int_{-\infty}^{\infty}(-\frac{\partial f}{\partial E})dE(E-E_F)^2+\cdots$$

which can be simplied as following:

$$N=Q(E_F)+\frac{1}{2}Q''(E_F)\int_{-\infty}^{\infty}(-\frac{\partial f}{\partial E})dE(E-E_F)^2+\cdots.$$

So

$$\begin{aligned}N&=Q(E_F)+\frac{(k_BT)^2}{2}Q''(E_F)\int_{-\infty}^{\infty}\frac{\xi^2}{(e^{\xi}+1)(e^{-\xi}+1)}d\xi+\cdots\\&=Q(E_F)+\frac{\pi^2}{6}Q''(E_F)(k_BT)^2+\cdots\end{aligned}\,, \tag{A.12}$$

When T=0K, $N=Q(E_F^0)$ where E_F^0 is the Fermi level when the electron temperature is 0 K. For temperature above 0K, we do a taylor expansion of $Q(E_F)$ around E_F^0 and only keep the terms to T^2

$$N=Q(E_F^0)+Q'(E_F^0)(E-E_F^0)+\frac{\pi^2}{6}Q''(E_F^0)(k_BT)^2\,, \tag{A.13}$$

So we can get

$$E_F = E_F^0\{1-\frac{\pi^2}{6E_F^0}[\frac{d}{dE}\ln N(E)]_{E_F^0}(k_BT)^2\}, \tag{A.14}$$

From the definition of Q(E), Q'(E) is the density of state N(E),so

$$E_F = E_F^0\{1-\frac{\pi^2}{6E_F^0}[\frac{d}{dE}\ln N(E)]_{E_F^0}(k_BT)^2\}, \tag{A.15}$$

For two dimensional Dirac-Fermion in graphene, N (E) is proportional to E, so

$$E_F = E_F^0\{1-\frac{\pi^2}{6}(\frac{k_BT}{E_F^0})^2\}, \tag{A.16}$$

Then we try to calculate the heat capacity of electron. The total energy of electron can be written as:

$$U = \int_0^\infty Ef(E)N(E)dE, \tag{A.17}$$

To calculate the integration, we introduce function $R(E) = \int_0^E EN(E)dE$, which means the total energy of the electron when the quantum states were fully filled with electrons, integration by part we can get:

$$\begin{aligned} U &= \int R(E)(-\frac{\partial f}{\partial E})dE \\ &= R(E_F^0) + R'(E_F^0)(E_F - E_F^0) + \frac{\pi^2}{6}R''(E_F^0)(k_BT)^2 \end{aligned}, \tag{A.18}$$

Since

$$E_F = E_F^0\{1-\frac{\pi^2}{6E_F^0}[\frac{d}{dE}\ln N(E)]_{E_F^0}(k_BT)^2\},$$

$$U = R(E_F^0) + \frac{\pi^2}{6}R'(E_F^0)(k_BT)^2\{-[\frac{d}{dE}\ln N(E)]_{E_F^0} + \frac{d}{dE}\ln R'(E)]_{E_F^0}\}, \tag{A.19}$$

We have $R'(E) = EN(E)$, so

$$
\begin{aligned}
U &= R(E_F^0) + \frac{\pi^2}{6} E_F^0 N(E_F^0)(k_B T)^2 \{-[\frac{d}{dE}\ln N(E)]_{E_F^0} + \frac{d}{dE}\ln(EN(E))]_{E_F^0}\} \\
&= R(E_F^0) + \frac{\pi^2}{6} E_F^0 N(E_F^0)(k_B T)^2 \{-\frac{1}{E_F^0} + \frac{N(E_F^0) + E_F^0 \frac{dN(E)}{dE}|_{E_F^0}}{E_F^0 N(E_F^0)}\} \\
&= R(E_F^0) + \frac{\pi^2}{6} E_F^0 N(E_F^0)(k_B T)^2 \{\frac{\frac{dN(E)}{dE}|_{E_F^0}}{N(E_F^0)}\} \\
&= R(E_F^0) + \frac{\pi^2}{6} N(E_F^0)(k_B T)^2
\end{aligned}
, \qquad \text{(A.20)}
$$

Thus we can get the unit area electron heat capacity:

$$
C_e(T_e) = \frac{1}{A}\frac{\partial U}{\partial T} = \frac{2\pi}{3}\frac{E_F^0}{\hbar^2 v^2} k_B^2 T , \qquad \text{(A.21)}
$$

Here we get the heat capacity proportional to T instead of T^2 in contradict to the case where the Fermi level is at K point.

Assuming a Fermi level of 348meV,

$$
C_e(T_e) = \frac{1}{A}\frac{\partial U}{\partial T} = \frac{2\pi}{3}\frac{E_F^0}{\hbar^2 v^2} k_B^2 T = 20.132 * 10^{-10} T(J/m^2 * K), \qquad \text{(A.22)}
$$